Karlsruhe Institute of Technology

Institute of Fluid Mechanics

Development of an empirical body force model for plasma-based flow control in CFD applications

Entwicklung eines empirischen Volumenkraftmodells für Plasma-basierte Strömungskontrolle in CFD Anwendungen

Master Thesis of

Maiken Günther

At the Department of Mechanical Engineering,
Institute of Fluid Mechanics

Advisors: Prof. Dr.-Ing. Bettina Frohnapfel

Dr.-Ing. Jochen Kriegseis

Duration: July 2020 – November 2020

I declare that I have developed and written the enclosed thesis completely by myself, and have not used sources or means without declaration in the text.

Karlsruhe, 30. 11. 2020

.....

(**Maiken Günther**)

Abstract

In the present work a new empirical model for the phase-resolved body forces of an DBD (Dielectric-Barrier-Discharge)-plasma actuator is developed. Therefore planar body forces have been derived from existing PIV (Particle-Image Velocimetry) measurements. A new approach is introduced that makes use of the similarity of fluid dynamic and electrostatic potential theory. The body forces are derived with the gradient of a scalar potential field that consists of superimposed single body force potentials. A system of linear equations describes the relation between the gradient field, the magnitude of the single potentials and the resulting body forces. A least-square fit of this equation system to the experimental body forces approximates the local magnitude of the potentials.
The modeling results are compared to the experimental data regarding their phase-averaged and phase-resolved integral body force, the spatial body force distribution and the physical plausibility of the potential magnitudes. Centering around a baseline state, different numeric configurations of the model and their results are presented and discussed.
This baseline state strongly indicates the validity of the developed approach, particularly regarding the resulting values of phase-resolved integral body forces. A future improvement of the numeric setup of the model is expected to prove the similarity of the distribution of body force potentials and free charges in the discharge area. This could lead towards a model that is independent from experimental validations. Finally, the new model is drawn into comparison with former modeling approaches by Shyy *et al.* [28], Suzen *et al.* [31] and Maden *et al.* [23]. Here it asserts itself with its unique capability to represent both components of phase-resolved body forces with good accuracy.

Kurzfassung

In der vorliegenden Arbeit wird ein neues empirisches Modell der phasenaufgelösten Volumenkräfte entwickelt, die mit einem DBD (Dielectric-Barrier-Discharge/Dielektrische Barriereentladung) Plasma Aktuator erzeugt werden. Dazu wurden zuvor die zweidimensionalen Volumenkräfte aus vorhandenen PIV (Particle-Image Velocimetry) Messungen abgeleitet.
Das neue Modell nutzt die Gemeinsamkeiten der Anwendung der Potentialtheorie, sowohl in der Strömungsmechanik als auch der Elektrostatik. Die Volumenkräfte werden dabei als der Gradient eines skalaren Potentialfelds definiert, das aus der Überlagerung einzelner so genannter Volumenkraftpotentiale besteht. Das Gradientenfeld, die Ergiebigkeit der einzelnen Potentiale und das resultierende Volumenkraftfeld werden durch ein lineares Gleichungssystem verbunden. Daraus werden anschließend mit Hilfe der Methode der kleinsten Fehlerquadrate die Ergiebigkeiten der Potentiale an die experimentellen Volumenkraftdaten angenähert.
Die Ergebnisse der Modellierung werden anhand ihrer Übereinstimmung mit den experimentellen Daten validiert. Dabei werden die räumliche Verteilung der Volumenkräfte, als auch ihre phasengemittelten sowie phasenaufgelösten integralen Werte verglichen. Ein weiteres Kriterium für die Güte des Modells ist die physikalische Plausibilität der Ergiebigkeiten der Potentiale. Ausgehend von einem Grundzustand werden verschiedene numerische Konfigurationen des Modells sowie die dazugehörigen Ergebnisse vorgestellt.
Bereits der Grundzustand deutet stark auf die Gültigkeit des entwickelten Ansatzes hin, insbesondere im Hinblick auf die phasenaufgelösten integralen Volumenkraftwerte. Ein Beweis des Zusammenhangs zwischen der Verteilung der Volumenkraftpotentiale und der Verteilung der geladenen Teilchen im Plasma ist im Laufe zukünftiger Weiterentwicklungen des Modells zu erwarten. Dies könnte zu einem erweiterten Modell führen, das unabhängig von experimentellen Daten ist. Abschließend wird das neue Modell mit den bestehenden Modellierungsansätzen von Shyy *et al.* [28], Suzen *et al.* [31] und Maden *et al.* [23] verglichen, dabei besticht es durch die Fähigkeit, beide Komponenten der Volumenkräfte phasenaufgelöst und mit zufriedenstellender Genauigkeit darzustellen.

Contents

1. Introduction

Within the past decades the influence of air-based logistics on global climate change have begun to gain importance. Inter alia, the necessity of reducing the negative impact of aviation on the global climate is driven by the foresight of future generations characterized by growth of population and increasing globalization.
Regardless of the specific form of drive technology, a key towards more energy-efficient flight is the reduction of drag that is induced in the boundary layer of the aircraft surface. In addition and especially when regarding future performance improvements, including higher ascent rates and larger end-speeds, it is essential to avoid so called stall effects on the airfoil. Stall occurs when the flow is not able to follow the surface and detaches instead, resulting in the interruption of momentum transfer, the increase of drag and the decrease of lift.
Throughout the history of aerodynamics different methods of avoiding stall effects on airfoils have been studied. Three main effects can be manipulated: laminar-to-turbulent transition, flow separation and induction of turbulence [24]. In order to regulate these effects, methods of active flow control as mechanical flaps or synthetic wall jets are applied on a large scale. They show clear advantages over passive flow control methods like delta shaped airfoils or vortex generators, as those cause a further increase of drag and can not be specifically activated when needed, as for take-off and landing for instance [10].
In the beginning of the 21st century researchers found promising results in the application of non-thermal plasma discharge actuators for active boundary layer flow control. The AC-driven dielectric barrier discharge (DBD) actuators consist of two electrodes, which can both be integrated into the airfoil. One is exposed to the surface, the other is located slightly downstream and is embedded into a dielectric sheet to inhibit a direct discharge. Ions are generated and accelerated by the strong electric field between the electrodes and induce momentum in the surrounding gas, resulting in a flow field with velocities up to around 10 m/s [2, 15, 24].
The essential advantage this active flow control method has over prior ones is the minimal mechanical impact on the shape of the airfoils, as the electrodes of the actuator have a nearly negligible height or can be integrated into the surface of the airfoil. They are rather easy to manufacture, operate with relatively low power consumption, exhibit high frequency responses and have no moving parts. On the other hand, precise flow induction is challenging and becomes even more difficult for higher Reynolds numbers as compiled by Kotsonis [15]. In addition, the high voltages applied for the ionization of the gas and acceleration of ions require a high operation stability due to safety considerations.

1.1. Motivation

To improve the operation stability and thus leading to a reliable control of the DBD actuator, its modes of action must be understood. For analyses independent from experimental examinations, the effects of the plasma actuator are integrated into computational fluid dynamics (CFD) simulations. This is achieved with boundary conditions in form of body forces. There have been several approaches to modeling these body forces generated by the DBD:
Shyy *et al.* [28] found a simplistic approach that is capable of convincing computations of the integral and phase averaged body force, but is not able to resolve its spatial distribution. A more physical model by Suzen *et al.* [31] computes the body forces with an estimation of the external electric field and location of charged particles. Yet the corresponding CFD simulations of both models generate unsatisfactory results. A more recent and solely empirical model was presented by Maden *et al.* [23]. They found a mathematical description of the phase-averaged body forces in horizontal direction that is able to resolve the induced velocity profile in CFD simulations. Nevertheless, its applicability on other actuator configurations is limited.
Above all, DBD actuators are driven by AC and Kuhnhenn *et al.* [19] confirmed a highly phase-dependent behavior of the body forces with PIV measurements. All previously mentioned models are focused on phase-averaged body forces and are therefore not able to compute the phase-resolved body forces at all, or only to some extent. Summarizing, a phase-resolved model of the body force is needed for an accurate phase-resolved computation of the flow field generated by a DBD plasma actuator.

1.2. Objective

The objective of this thesis is the development of a new empirical phase-resolved model of the body forces generated by the plasma actuator that can be used as boundary conditions in CFD simulations. To achieve this, a new approach based on the analogies of fluid dynamics and electrostatic fields is introduced and discussed. The new model will be able to represent the phase-resolved body forces based on PIV (Particle-Image Velocimetry) measurements by Hehner *et al.* [12, 13].
It will then be compared to former models by Shyy *et al.* [28], Suzen *et al.* [31], as well as Maden *et al.* [23] in order to estimate its performance in further CFD simulations.

1.3. Thesis Outline

First, the principles of plasma discharge are described. For the following presentation of the new model, potential theory is introduced in an electrostatic context, as well as in a fluid dynamic one. A brief outline describes the electrohydrodynamic link between both scientific fields. With this background the working principles of DBD plasma actuators are characterized up to first estimations of its phase-resolved behavior. Subsequently, the modeling approaches mentioned before are elucidated and evaluated. As the PIV measurements by Hehner *et al.* [12, 13] provide the data for the new empirical model, their experimental setup is presented briefly and the determination of body forces from velocity fields is discussed.
Next, the new empirical model is introduced. Its rationale, implementation as well as the fitting to the experimental data is described and different configurations of the model are shown and discussed.
Finally, the strengths of the new model are highlighted and brought into context to the phase-resolved distribution of free charges. For further classification, the new model is compared to the former approaches mentioned before. As the new model opens up vast opportunities for further examinations, a detailed outlook for future research topics is given.

2. Theoretical Background

Following, the theoretical background of the thesis is highlighted. A brief introduction in the vast field of plasmas leads towards the discharge effects that cause the induction of ionic winds. Subsequently potential theory is introduced the context of fluid dynamics as well as electrostatics. The field of electrohydrodynamics does not provide a lot of literature, hence only a brief introduction into the topic is given. This leads towards the description of the DBD plasma actuator. It is focused on the electric and phase-resolved characteristics of the discharge. Finally, three modeling approaches are introduced and discussed thoroughly as their methods and results will be compared to the new model.

Note that in this thesis two terms are used that are worth clarifying beforehand. The first one is *topography* with a meaning similar to its use in geography. Here, it describes the spatial distribution of body forces. The terminology results from the 3D view of the body force field, where regions of high body forces are displayed as elevations and low body forces similar to a vale. It was introduced to avoid confusion with the term "distribution of body force potentials", that refers to the exact position of the potentials. The second term is *potential field*. Potentials are defined as scalar field, as will be introduced. Sometimes its gradient field is named "potential field", but here the term refers to scalar values in the numerical grid that are the result of superimposed potentials.

A second annotation concerns the notation of the direction of vectorial values. In this thesis capital letters (X and Y, mostly superscripted) refer to the respective direction vector. This will improve the distinction against location vectors in the coordinate system (lower letters x and y).

2.1. Physics of Plasmas

The word plasma describes matter of partly or fully ionized gases. Besides gaseous, liquid and solid, plasma is commonly referred to the fourth state of matter. It is described by its kinetic temperature T and the density of charged particles n. The kinetic temperature T is linked to the charge of an electron temperature T' by Boltzman's constant k and the electron charge e:

$$kT = eT' \tag{2.1}$$

Hence, an elementary charge in a potential difference of $n \cdot 1\,\mathrm{V}$ (means with a kinetic energy of $n \cdot 1\,\mathrm{eV}$) refers to a kinetic temperature of $n \cdot 11\,604\,\mathrm{K}$ according to the fraction k/e [16].

This leads to an important classification of plasmas into equilibrium and non-equilibrium plasmas. In an equilibrium plasma all electrons, ions and neutrals have the same kinetic temperature $T_e = T_i = T_n$. In a non-equilibrium plasma the electrons have a kinetic energy in the range of 1 to 10 eV(equals 1 to 10 times 11 604 K) whereas the temperature of ions and neutrals stays approximately the same as the ambient temperature: $T_i \approx T_n \approx 300\,\mathrm{K}$ [16].

Another important characterization of plasmas is the degree of ionization α. It is defined by the charge density of ions n_i and neutrals n_n:

$$\alpha = \frac{n_i}{n_n + n_i} \tag{2.2}$$

Due to random motions of particles in the plasma, collisions happen with the exchange of momentum (respectively kinetic temperature). In the presence of an uniform electric field $\vec{E}$, these random collisions are superimposed by a systematic motion due to the direction of the field. This superimposed motion is known as drift, and is described by the drift velocity $\vec{v_d}$. The sign of the velocity depends on the charge of the particle, m describes the mass of the particle and ν_m the frequency of collisions.

$$\vec{v_d} = \pm\frac{e}{m\nu_m}\vec{E} \tag{2.3}$$

For a better understanding of the discharge principles in plasmas, we take a look at a nearly evacuated tube that contains two electrodes facing each other. By applying the voltage V_{supply}, a uniform electric field $\vec{E}$ builds up between the electrodes.

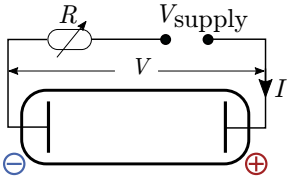

Figure 2.1.: An evacuated tube as a simplified model for the understanding of plasma discharge (based on Francis [9]).

The DBD actuator described later is operated under atmospheric pressure and driven by AC in contrary to the DC in the discharge tube. Furthermore, the electrodes do not face each other as in fig. 2.1 but mounted in one plain on a bench to create a surface discharge. The main difference on a molecular basis between discharges in low and ambient pressure is the mean free path length of particles, which is larger at low pressure. This influences the frequency of collisions between particles ν_m and therefore the particles are decelerated less in low pressure. Nevertheless the behavior of the electric current and the voltage in the described setup are widely studied and are qualitatively comparable to the discharge that is examined in this work.

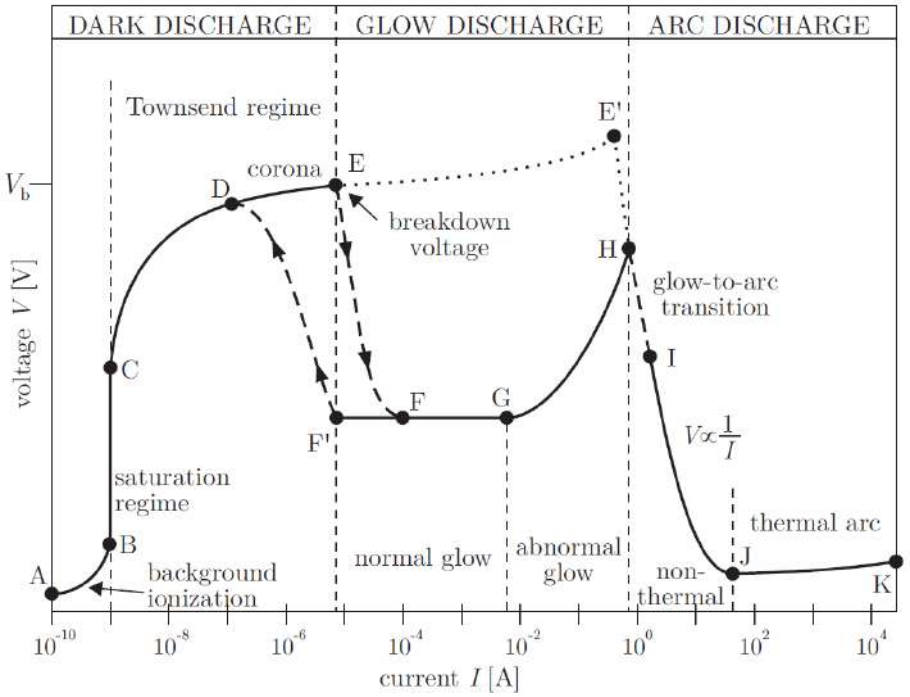

Figure 2.2.: Voltage versus current for DC discharges at low pressure based on Roth [25] and compiled by Kriegseis [16]

.

At low, negligible voltages the ions in the gas originate solely from background radiation. Up to point B, these ions drift towards the electrodes. The electric current stays the same between B and C, as only the stated ions in the gas are moved, relating to the ionization rate by background radiation.

Beyond point C, the electric field provides enough energy for these electrons to ionize other atoms as they collide. These collisions release new electrons that are accelerated and cause new collisions themselves. This ”snowball effect” leads to a non-linear relation between voltage and current and is the main mechanism in the so called Townsend regime (C-E). Up until point E, all ions in the gas (with exception of those generated in the snowball effect) originate from background radiation, making the discharge non-self-sustaining. For the sake of completeness is it said that a special form of discharge can occur at sharp edges of the electrodes. The local electric field becomes particularly high and causes corona-discharges. For specific geometries of the electrodes at ambient pressure, this effects can lead to a behavior as indicated by the dashed line in fig. 2.2.

At point E the electrical breakdown voltage of the gas is reached, causing the resistance of the gas to decrease dramatically. The current increases and the voltage drops to point F. Following, the plasma covers the cathode and the current increases independently from the voltage. Thus the voltage has to increase significantly up to reach point H. Beginning from F the electric field is strong enough to ionize the gas. This glow discharge is not longer depending on the background radiation and is therefore called self-sustaining. Once established, the glow discharge maintains even for a slightly reduced current and therefore shows the hysteresis indicated by point F’

For increasing currents, the electrodes are heated up by Joule heating and additionally to the effects described before, electrons are emitted from the electrodes by thermionic emission. The current increases due to the additional electrons and visible discharge arcs are formed, leading to dramatic voltage drops [11].

Due to collisions in the gas, the atoms are excited and then go back to ground state under the emission of light. As the name "glow regime" indicates, around point E the emitted light gets visible by naked eye can be seen in fig. 2.6.

Ionic Wind

Up until now, the detailed mechanisms that cause ionic winds are not yet understood. In accordance to the drift velocity mentioned before, the ions and electrons are accelerated in the discharge. By transferring momentum to neutral particles, they create a so called "ionic wind". Because of further collisions between neutral particles the flow field propagates even to regions that are not affected by the discharge. Although the electrons reach much higher velocities than the ions, they are not able to transfer a significant amount of momentum to the neutral particles due to their small mass. Yet the velocity of ions can reach up to a few thousand m/s according to Moreau [24].

The principle directions of the ionic wind around a surface discharge is shown in fig. 2.3. At the upstream side, the surrounding air is sucked towards the discharge and accelerated nearly parallel to the surface. This accelerated flow is referred to as the wall jet.

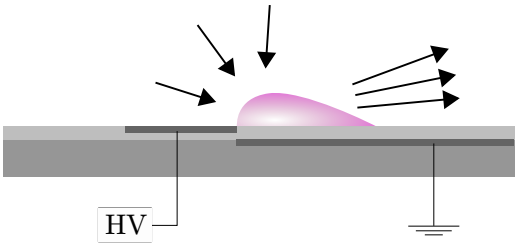

Figure 2.3.: Flow directions around the discharge without external flow

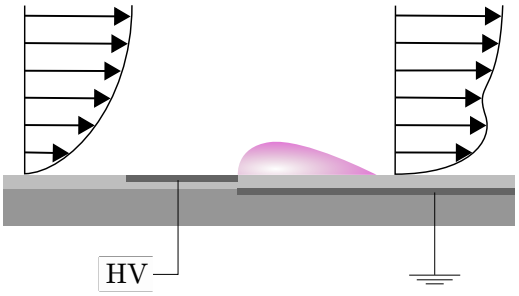

Figure 2.4.: Boundary layer manipulation of an external flow field through discharge

Figure 2.4 sketches how the boundary layer of an external flow field can be manipulated. The upstream flow shows the well-known boundary layer that is formed to viscous effects close to the wall. Due to the wall jet, this layer is manipulated, even outside the bounds of the discharge.

2.2. Potential Theory in Fluid Dynamics

The introduction of a potential-based theory was found to be a valid method of describing certain phenomena in fluid dynamics, for example the flow around solid objects [29]. For incompressible flows potential theory is an exact solution to the Navier-Stokes equations. Yet this solution is mostly of theoretical nature as potential theory is not able to describe friction effects. To compensate this lack, the combination of potential and boundary layer theory was found to show good approximations for real-life applications.
The essence of potential theory states that a flow can be described by overlaying single velocity potentials ϕ. Their gradient describes the velocity field as shown in equation 2.4.

$$\vec{u} = -\nabla\phi \tag{2.4}$$

Inter alia, these potentials can describe so called sources and sinks. A potential sink absorbs flow in one point. In contrast, source describes a point of emerging flow. A quite

intuitive analogy is shown in 2.5 by comparison with a straw, through which a fluid is sucked or expelled. Comparable to a potential sink, the fluid is sucked symmetrically to the orifice of the straw and absorbed. Unfortunately the opposite flow direction, with the straw acting as source, is not feasible in reality.

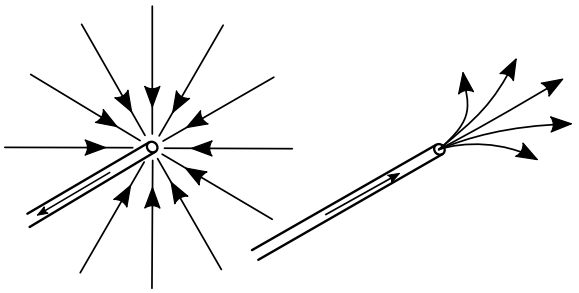

Figure 2.5.: Analogy of a source and sink in fluid dynamics to the orifice of a straw. While the suction of fluid is comparable to a sink, the expelling of fluid does not resemble a source, adapted from Spurk and Aksel [29]

Similar analogies exist in electrostatics and electrodynamics as will be described in section 2.3, but for simplification reasons this chapter will refer to fluid dynamics. When referring to electrostatics, the potentials will be named electric potentials.

There are two main mathematical formulations for a sink that are applied and compared in this thesis: $\phi = 1/r$ for a single point sink and $\phi = \ln r$ for a line sink. These two formulations will be discussed graphically in the context of the corresponding modeling results in chapter 5.1.3. For easier numerical handling a third mathematical formulation one was evaluated: $\phi = \exp(-r^2)$. As later the logarithm-based formulation will stand out, the characteristics of potentials will be explained with this example:

The decay of a potential is described by a magnitude M and the distance r from the center of potential.

$$\phi = \frac{M}{2\pi} \ln r \tag{2.5}$$

Due to the nature of the logarithm, the formulation in equation 2.5 describes a sink. A simple multiplication with -1 results in the equivalent source. The potential at the origin of the sink ($r = 0$) is not defined and therefore a singular point. Supported by the analogy of the straw, it is obvious how the sink violates the continuity equation. For mathematical applicability, the singular point is therefore usually located outside of the interrogation area.
To get a description of the flow that is absorbed by the sink, the magnitude M is defined as the flow that passes through a sphere around the sink, defined with the radius r and the surface A_s.

$$M = \iint_{A_\mathrm{s}} \vec{u} \cdot \vec{n} \, \mathrm{d}A_\mathrm{s} = \iint_{A_\mathrm{s}} \frac{\partial \phi}{\partial r} \cdot \vec{n} \, \mathrm{d}A_\mathrm{s} \tag{2.6}$$

The magnitude M is independent from the radius, as the continuity equation is only violated by the singular point ($r = 0$).

2.3. Electrical and Electrohydrodynamical Background

The described boundary-layer flow originates from electrical forces that interact electrohydrodynamically with the fluid. Following, these properties will be outlined.

2.3.1. Electrostatics

The electric potential of a single point charge Q (located at the origin of the coordinate system) at a distance r from the charge is described with the permittivity of vacuum ϵ_0 by

$$\phi(r) = \frac{1}{4\pi\epsilon_0}\frac{Q}{|r|}. \tag{2.7}$$

By definition and resulting from equation 2.7 a negative charge leads to a negative potential and vice versa. For multiple charges q_k, the local electric potential ϕ with the distance r can be expressed by the sum of the single charges:

$$\phi = \frac{1}{4\pi\epsilon_0}\sum\frac{q_k}{|r - r_i|}. \tag{2.8}$$

The potential difference between two points is called voltage.
The presence of at least one charge forms a vector field called the electric field. The electric field $\vec{E}$ is defined by the electrostatic force $\vec{F}_\mathrm{e}$ acting on a hypothetical small test charge q. Also the electric field can be described by the negative gradient of the electric potential.

$$\vec{E} = \frac{\vec{F}_\mathrm{e}}{q} = -\nabla\phi \tag{2.9}$$

2.3.2. Electrohydrodynamics

The barely investigated field of electrohydrodynamics (EHD) deals with the dynamics of electrically charged and neutral fluids and their interactions with electric fields. Most assumptions can only be made for very dilute fluids, where a single charged molecule is not affected by the field generated by other molecules, only by the applied external electric field. In real life applications, the generation and decay of charges and their interaction has to be taken into account. Nevertheless, Landau and Lifshitz [20] found an analogy that was developed further by Castellanos [3]. They derive the body force generated by an electric field into a fluid with the analogy of a parallel plate capacitor. The fluid is confined within the plates. The distance between the plates is increased marginally at constant potential of the electrodes, resulting in a change of the electric field. This electric change is brought into the fluid as mechanical stress due to the expansion. With the electric field $\vec{E}$ and the displacement vector $\vec{D}$, this change of a thermodynamic potential $\tilde{F}$ in relation to the thermodynamic potential in the absence of the electric field F_0 can be expressed as:

$$\delta\tilde{F} = \delta F_0 - \vec{D}\cdot\delta\vec{E} \tag{2.10}$$

Applying Maxwell's equations, Gauss theorem and mass conservation, an isotherm process leads to the relation of the body force $\vec{f}_\mathrm{b}$ to the electric field $\vec{E}$:

$$\vec{f}_\mathrm{b} = q_\mathrm{c}\vec{E} - \frac{1}{2}E^2\nabla\epsilon + \nabla p_\mathrm{st} \tag{2.11}$$

The first term containing the charge density q_c is called the Coulomb force and usually dominates the body force as its the strongest EHD force term. The dielectric force $\frac{1}{2}E^2\nabla\epsilon$ describes the force exerted on a non-homogeneous dielectric fluid by an electric field and can be neglected if the AC period is longer than the charge relaxation time. The last term refers to the electrostrictive force with the electrostrictive pressure $p_{st} = (1/2)\epsilon a E^2$ with the permittivity ϵ. It is treated as a modification to the fluid pressure and can be neglected for the assumption of an isobaric discharge. This leads to the electrohydrodynamic link between fluid mechanical body forces and the electric field:

$$\vec{f_b} = q_c\vec{E} \tag{2.12}$$

This relation is equivalent to the definition of the electric field in equation 2.9 and therefore indicates the accordance of the electric field and body force. Castellanos does not comment on this relation, but it can be estimated that the direct equation of electric and mechanic force is the result of gross simplifications.
Even disregarding this contradiction, equation 2.12 clarifies the difficulties of the determination of body forces: It calculates the influence of the electric field on a single charge while this charge is also part of the electric field itself.

2.4. DBD Actuators

Using ionic winds to manipulate the boundary layer of a flow field was first mentioned in the 1990s by researchers from the University of Poitiers in France and the University of Buenos Aires (Argentina). Subsequently, the first group to establish a stable surface DBD was directed by Roth in the beginning of the 2000s at the University of Tennessee (USA), as summed up by Moreau [24].

The actuator consists of two electrodes with an applied electrical potential difference in orders of kV. The electrodes are separated by a dielectric sheet to inhibit direct discharge and therefore the actuator is driven by AC with a frequency up to a hundreds of kHz. Figure 2.6 shows a photograph of a DBD actuator where the discharge area glows in a paint lilac.

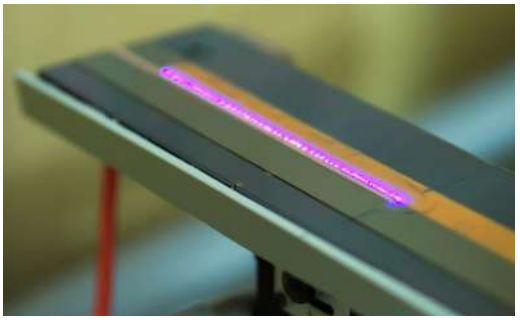

Figure 2.6.: Photograph of DBD discharge recorded by Maden *et al.* [21]

Although the boundary layer manipulation resulting from DBD actuators has already proven its functionality in several studies (e.g. [18, 24]), the phase-resolved mechanisms of charge distribution and momentum transfer still has to be investigated. Nevertheless, several electrical characteristics of the actuator have been observed that lead to an estimation of the phase-resoved charge distribution.

Electrical Characteristics of a DBD Plasma Actuator

Kriegseis [16] investigated the DBD actuator regarding its discharge characteristics and describes the relation between the charge of the electrodes (Q) and the applied voltage (V) as shown in fig. 2.7. This Q-V cyclogram is called a Lissajous figure and will be a base for further explanations of the DBD actuator as well as the determination of later examination phases in the cycle. The gray enclosed area is the electrical power of the actuator.

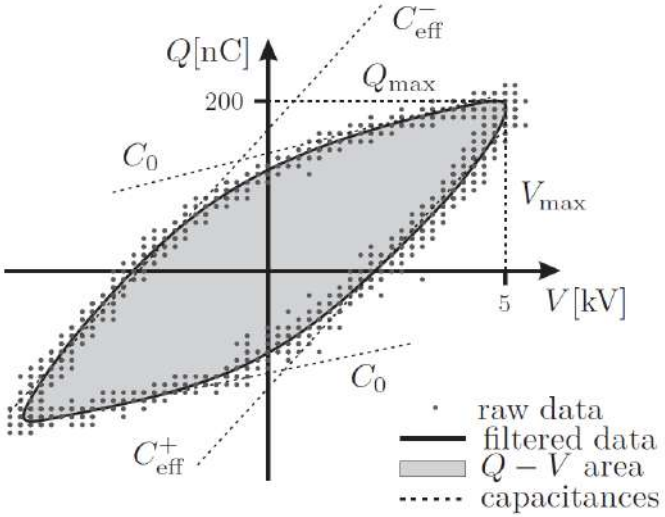

Figure 2.7.: Lissajous figure of a DBD plasma discharge found by [16].

The actuator capacitance C_i for discrete points i is displayed in the Lissajous figure as Q-V-slope and can be approximated as following:

$$C(t_i) = \left.\frac{\Delta Q}{\Delta V}\right|_i \tag{2.13}$$

As already marked in 2.7, two characteristic capacitances of the DBD actuator can be distinguished: the cold capacitance C_0 and the effective capacitance C_{eff}. In phases of cold capacitance, the actuator behaves like a pure passive component (the value of C_0 remained the same for a simple multimeter measurement of an actuator that was disconnected from the electric supply). For phases before the maximum voltage is reached, the capacitance reaches maximum values of C_{eff}. Therefore Kriegseis [16] adapts the theory of Enloe *et al.* [6], stating that the free charges generated by the actuator act similar to an enlargement of the exposed electrode. This leads to an increased capacitance of the actuator as sketched in fig. 2.8.

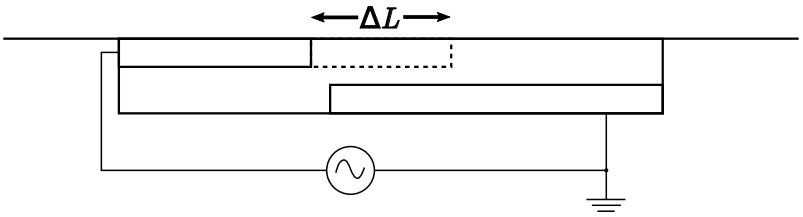

Figure 2.8.: Scheme of the virtual, adapted from Steffes [30]. The free charges on the actuator surface behave similar to a downstream enlargement of the exposed electrode by the length ΔL

The effect is displayed in fig. 2.9 for multiple AC-phases. Here the regions of cold and effective capacitance are marked in gray. Starting from the passive actuator, the capacitance rises up to the effective value. Briefly after the maximum voltage, the virtual electrode collapses and the capacitance drops again to the value of C_0. The peaks towards infinitive values are due to the discrete calculation as shown in eq. 2.13. Note how the values of C_{eff} are slightly higher for an applied negative voltage than for positive voltages, indicating different effects for each maximum voltage.

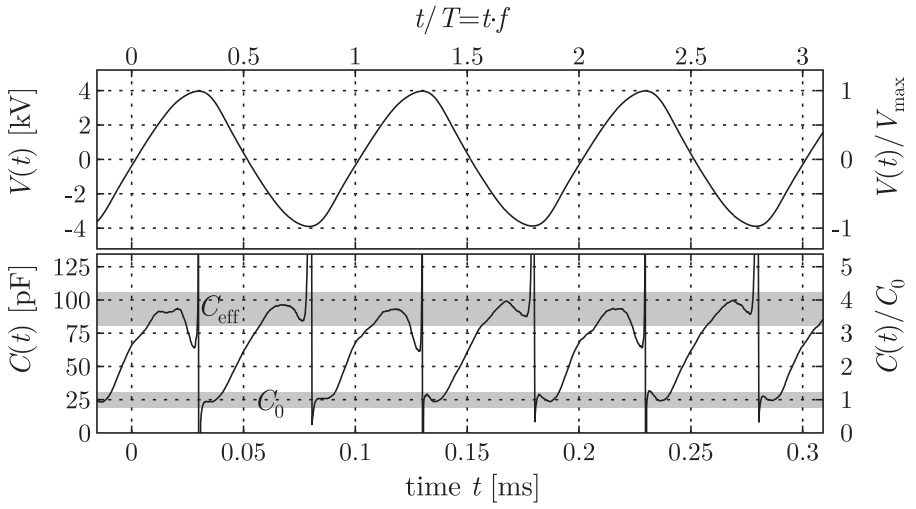

Figure 2.9.: Voltage and capacitance measurements of a DBD by Kriegseis [16].

Though observations as presented before result from effects of free charges, their exact spatial distribution in relation to the phase of the voltage supply is not yet understood. Intricate and highly dynamic interactions between the alternating electric field and the charged particles take place. In addition, the typical spatial and temporal scales of the discharge are 4-8 orders of magnitude smaller than those of the resulting airflow [16]. The main impacts which affect the distribution of charges are:

- The applied voltage and therefore the electric field
- The virtual length of electrodes
- Repulsion between electrical charges
- The inertia of ions compared to the inertia of electrons
- Emission and recombination of electrons on exposed electrode
- Emission and recombination of electrons with gas molecules

These interactions hamper a phase-resolved physical modeling of the charge distribution. Nevertheless, a possible sequence of charge distributions will be described as suggested by Steffes [30]. It is reduced to its main effects for simplification.

Negative Exposed Electrode

For an easier understanding of the discharge principles the actuator surface is presumed without free charges. In reality there will still be few charges on the dielectric originating from former half-cycle.
The major ionization of air molecules is located at the downstream edge of the exposed electrode, as the electric field reaches its maximum at this point of minimal distance between the electrodes. Some of the liberated electrons will react with air molecules, resulting

in negatively charged ions with a mass comparable to the mass of the positive ions. The charged ions are accelerated by the electric field as sketched in fig. 2.10. Collisions with neutral molecules result in a downstream facing force while the momentum transferred by ions is higher than by electrons due to their mass differences.

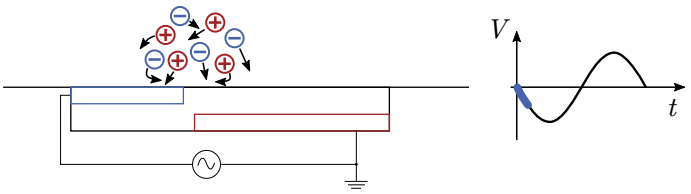

Figure 2.10.: Generated ions and their direction of movement in relation to the applied voltage. For simplification reasons the electrons and negative ions are summarized. Adapted from Steffes [30].

Positively charged ions recombine on the surface of the exposed, negatively charged electrode and are neutralized. Negative ions and electrons accumulate on top of the dielectric thus they can not be neutralized (fig. 2.11). These resulting negative charges act like an extension to the exposed electrode. According to the previous chapter, this effect is called a "virtual electrode" [16]. The electric field strength increases at the downstream end of the virtual electrode until new free charges are generated. The following movements of the charged particles are comparable to those at the beginning of the half-cycle. These effects take place until they reach the end of the bottom electrode, or in the present case of an AC-voltage until the electric field strength does no longer support the generation of charges.

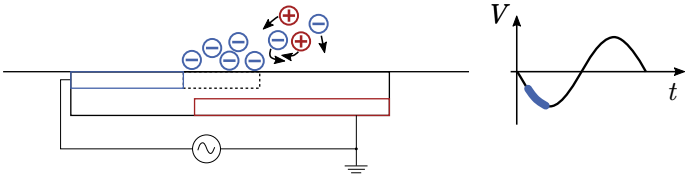

Figure 2.11.: Ions of the same charge as the exposed electrode accumulate on the dielectric and therefore act similar to a prolonged electrode. The electric field between these accumulated charges and the embedded electrode generates new charges that are accelerated. Adapted from Steffes [30].

At this point the charges at the surface start to degrade. This process is not yet understood. It is suggested that recombination with positive ions could neutralize the electrons. Another possibility is that with decreasing voltage, the electric potential of the upper electrode drops under the potential of the charges on the surface. Thus, the charges would start moving back towards the exposed electrode. Depending on the velocity and magnitude of these effects in relation to the frequency of the voltage there could still be negative charges on the surface at the beginning of the positive half-cycle.

Positive Exposed Electrode

In the case of remaining negative charges on the dielectric, these charges influence the discharge behavior particularly at the beginning of the positive half-cycle. They can initiate the generation of free charges that move towards the upper electrode. These avalanches due to the remaining electrons of the negative half-cycle occur additionally to the avalanches

due to background ionization. Therefore the charge density and resulting force can be larger than in the negative half-cycle.

Apart from the avalanches due to remaining charges the discharge behavior of the actuator in the positive half-cycle is similar to the one in the negative half-cycle: Positive ions and electrons are generated, some of the electrons might ionize air molecules to negative ions. First, the negative charges move towards the upper electrode and have the chance to recombine and neutralize. Following the positive charges move in the direction of the bottom electrode where they accumulate, prolonging the upper electrode into a positively charged virtual electrode.

Enloe *et al.* [7] found quantitative proof of a different amount of induced momentum by the negative and positive voltage. This results from the different average mass of positive and negative charges, as the negative ones are partly electrons. A description of their investigations will be given in the context of the phase-resolved body forces in chapter 3.3.

2.5. Modeling Approaches

The flow field induced by the actuator is described with the continuity equation, the two-dimensional Navier–Stokes equations and the energy transport equation for a steady incompressible flow. The continuity equation has to be solved for every species in the flow (the variable i corresponds to the species: electrons, ions or neutral particles). The variable R_i describes the rate of production and therefore contains the chemical transformation between species. For low-energy non-thermal plasmas the energy transport equation is often neglected to reduce calculation complexity and is therefore not listed here.

$$\frac{\partial \rho_i}{\partial t} + \nabla \cdot \rho_i \vec{u_i} = R_i \tag{2.14}$$

$$\rho(\frac{\partial \vec{u}}{\partial t} + \vec{u}\nabla\vec{u}) = -\nabla p + \nabla\tau + \vec{f} \tag{2.15}$$

The effects of the discharge are brought into the Navier-Stokes equations by the body force term. There have been several physical approaches to estimate this electroyhydrodynamic force for further applications in CFD simulations. This is one of the main causes for the difficulties of modeling the discharge on a physical basis.

In the modeling approaches presented here the electrohydrodynamic force is estimated to be equal to the Coulomb force with the charge density ρ_c as shown in equation 2.12. Yet, the local charge densities are not known for the phase-averaged nor for the phase-resolved field. A phase-resolved and qualitative estimation of charge densities was given by Steffes [30] as described in section 2.4. Nevertheless, the Coulomb force approximation proved to show first reasonable results, as will be shown in the description of the single approaches, and is in accordance to its dominance in equation 2.11.

2.5.1. Model by Shyy *et al.*

The first model described here was presented by Shyy *et al.* [28] and Jayaraman *et al.* [14]. The phase-averaged body force field is derived from a linear decrease of the electric field strength from a maximum value at the lower downstream corner of the exposed electrode in both spatial directions.

While the authors derive the wall shear stress and velocities out of the computed body forces with a numerical model, the present thesis focuses on the model of the body forces. The reconstruction of the resulting flow field was not possible in the time frame of this thesis.

The body force f^i is calculated by the combination of the local electric field strength E^i, charge density of electrons ρ_c and the elemental charge e_c. The charge density is simplified by setting the value of $1.0 \times 10^{11}\,1/\mathrm{cm}^3$.

$$\begin{aligned} f^X &= E^X \rho_c e_c \\ f^Y &= E^Y \rho_c e_c \end{aligned} \tag{2.16}$$

Although the electrons scarcely contribute to the momentum transfer of the plasma to the surrounding air due to their small mass, the electric field for the present calculations is formed by electrons. The maximum electric field strength E_0 is defined by the voltage amplitude applied to the upper electrode $V_{\max}$ divided by the horizontal distance $d = 0.25\,\mathrm{mm}$ between the electrodes.

$$E_0 = \frac{V_{\max}}{d} \tag{2.17}$$

The model by Shyy suggests a linear decrease of the maximum electric field strength in both spacial directions:

$$E(x, y) = E_0 - k_1 x - k_2 y \tag{2.18}$$

The coefficient of decrease is constant for each direction and is calculated with the maximum electric field strength E_0, the breakdown field strength E_b and the geometry factors a and b.

$$k_1 = \frac{E_0 - E_b}{b}, \qquad k_2 = \frac{E_0 - E_b}{a} \tag{2.19}$$

These coefficients are used to calculate the electric field in both directions:

$$E^X(x, y) = \frac{E(x, y) k_2}{\sqrt{k_1^2 + k_2^2}}, \qquad E^Y(x, y) = \frac{E(x, y) k_1}{\sqrt{k_1^2 + k_2^2}} \tag{2.20}$$

For discharge formation, the local electric field strength E must exceed the breakdown field strength E_b. The spatial boundary of this discharge region is estimated to resemble a triangular shape with a height of $a = 1.5\,\mathrm{mm}$ and $b = 3\,\mathrm{mm}$ as shown in 2.12. The values of a and b is estimated from a picture of the plasma discharge [26].

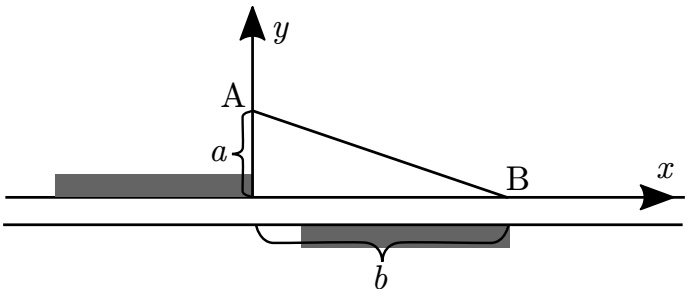

Figure 2.12.: Boundaries of the area where the local electric field strength exceeds the breakdown field strength E_b, based on Shyy *et al.* [28].

In later applications, a numerical model of the body force field should be able to estimate the behavior of the actuator for varying configurations. Yet, the investigations of Kriegseis (2016) show a strong dependency of the actuation frequency and voltage on the spatial boundary of the discharge area. Thus, the geometry factors would have to be estimated for each configuration.

Figure 2.13 displays the body force field as suggested by Shyy. The maximum body force is located at the downstream edge of the exposed electrode and decays in a triangular shape. Already on first sight, the extreme simplification of the experimental phase-averaged body force field (as in fig. 2.18a) is visible.

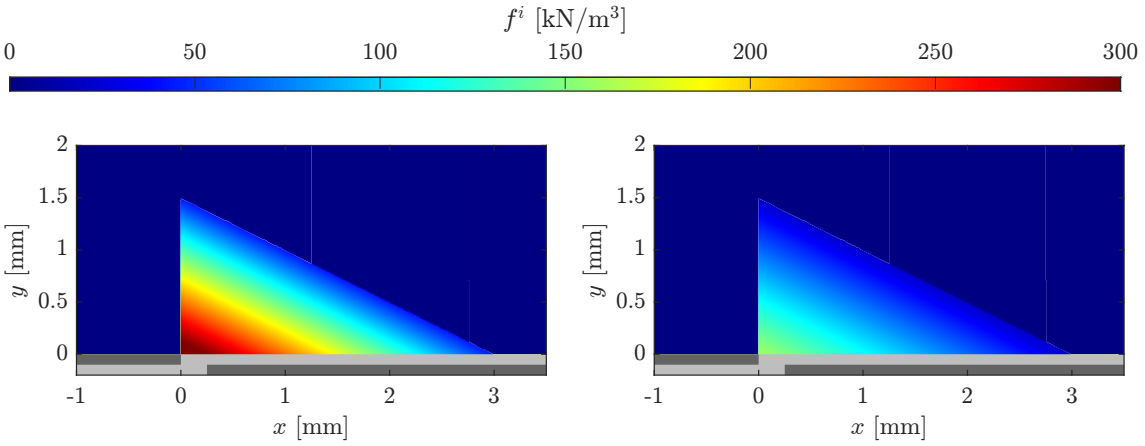

(a) X - direction (b) Y - direction

Figure 2.13.: Body forces, computation based on the model by Shyy *et al.* [28].

Nevertheless, for an actuation with 7 kV, the integral body force is computed with a relative error of about 20 % compared to experimental results according to Jayaraman *et al.* [14]. For lower actuation voltages the relative error decreases. Considering the rather rudimentary approach, the model by Shyy and Jayaraman offers remarkable accuracy.

2.5.2. Model by Suzen *et al.*

Suzen and his team [32] presented a model that is closer to physical reality. The body force is determined with applying electrostatic potential theory (eq.2.9) into the electro-hydrodynamic link between the body force and the electric field (eq.2.12):

$$\vec{f} = -\rho_c \nabla \Phi \tag{2.21}$$

The potential Φ is separated in two parts: The external electric field generated by the electrodes (ϕ), and the other one resulting from the ionized particles in the fluid (φ):

$$\Phi = \phi + \varphi \tag{2.22}$$

The first part of the equation is the potential resulting from the external electric field can be written with the relative permittivity $\epsilon = \epsilon_\mathrm{r} \cdot \epsilon_0$ as following.

$$\nabla \cdot (\epsilon_\mathrm{r} \nabla \phi) = 0 \tag{2.23}$$

The boundary conditions to solve these equations for the numeric are shown in fig. 2.14a. The exposed electrode has a given potential $\phi(t)$ that depends on the given voltage. The potential of the downstream electrode is set to zero. The permittivity of the respective medium distinguishes air ($\epsilon_\mathrm{r} = 1.0$) from the dielectric material($\epsilon_\mathrm{r} = 2.7$). At the dielectric-air interface the permittivity is set to the mean of both adjacent values.

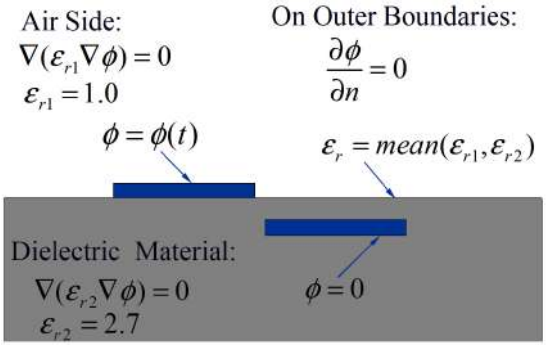

(a) Boundary conditions for computation of the external electric field

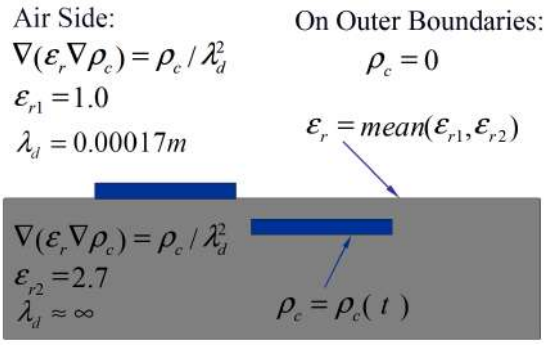

(b) Boundary conditions for computation of the electric field generated by free charges ρ_c

Figure 2.14.: Boundary conditions for the determination of the potential ϕ resulting from the external electric field and φ describing the influence of the charged particles in the field, according to Suzen *et al.* [31]

The potential due to free ionized particles is described by

$$\nabla \cdot (\epsilon_\mathrm{r} \nabla \varphi) = -\frac{\rho_\mathrm{c}}{\lambda_\mathrm{d}^2} \tag{2.24}$$

The modeling of the potential of an electrode is possible as described above, yet local charge densities (ρ_c in the upper equation) and the Debye length λ_d are unknown. Following experimental observations, Suzen assumes that the free charges behave similar to charges located in the embedded electrode. Therefore he set up the boundary conditions to solve eq. 2.24 as shown in fig. 2.16 with the time-dependent value $\rho_\mathrm{c}(t) = \rho_\mathrm{c}^\mathrm{max} f(t)$.

The value of $\rho_\mathrm{c}^\mathrm{max}$ as well als λ_d are calibrated with experimental PIV data. Therefore the value was fitted in such a way that the flow pattern and maximum velocity of the model was consistent to the experiment. It should be noted that Suzen refers to an actuator powered by a square wave with a frequency of 4.5 kHz and an amplitude of 5 kV. He observed a maximum velocity of approximately 1 m/s, leading to a value of $\rho_\mathrm{c}^\mathrm{max} = 0.0075\,\mathrm{C/m^3}$ and $\lambda_\mathrm{d} = 0.000\,17\,\mathrm{m}$. $f(t)$ was synchronized with the variation of the applied voltage.

The results of the modeling process can be seen in fig. 2.15 to 2.17. As predetermined by the boundary conditions and illustrated in fig. 2.15, the highest potential is located at the exposed electrode, dropping downstream until it reaches zero at the embedded electrode. The steepest decrease of potential (and hence highest electrical field strength) is located in between electrodes, indicating high body forces. Furthermore the flow streamlines show the suction of surrounding air as well as the acceleration into a wall jet as expected. On the right hand side the density of free charges is resolved according to equation 2.24. As Suzen models the free charges located on the embedded electrodes, the maximum charge density ρ_c^{max} is not visible.

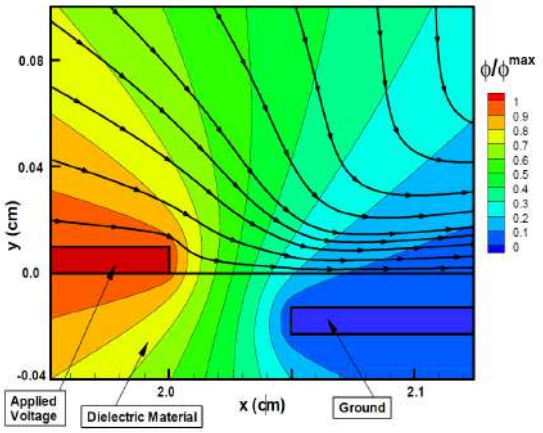

Figure 2.15.: Computed electric potential and flow streamlines induced by the external electric field according to Suzen *et al.* [31]

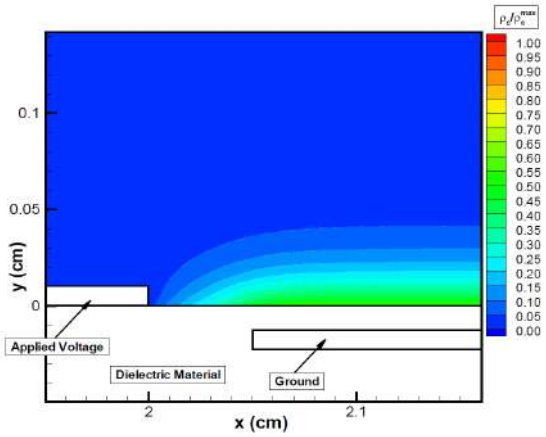

Figure 2.16.: Computed charge density due to free charges according to Suzen *et al.* [31]

With the solutions illustrated above, the body force field is computed with equation 2.21 and is displayed in fig. 2.17. Here the magnitude of the body force shows a maximum at the upstream edge of the embedded electrode. This is the region where both ϕ and ρ_c show major changes and again Suzen observes a good accordance to experimental observations.

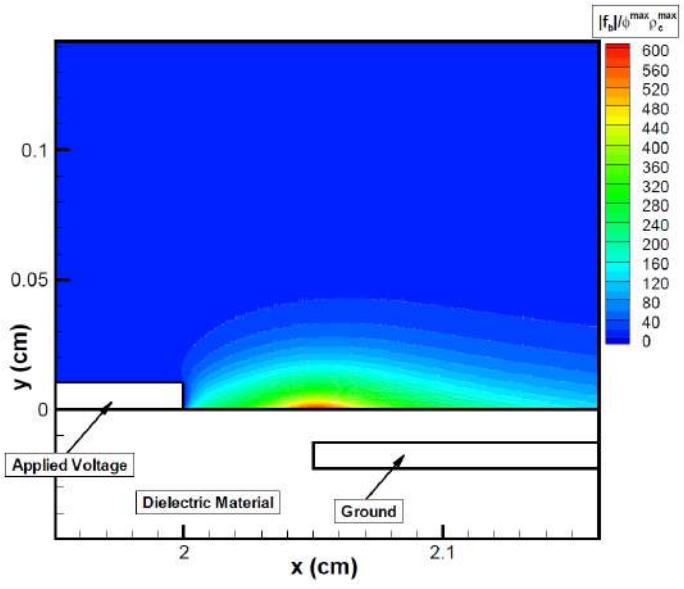

Figure 2.17.: Body force field, modeled by Suzen *et al.* [31]

Suzen does not give a quantitative evaluation of his results. This hampers the direct comparison to the other models.

2.5.3. Model by Maden *et al.*

Maden *et al.* [21, 23], was the first to develop a phase-averaged body force model on an empirical basis. He refers to the PIV measurements by Kriegseis [16] at 12 kV and with a frequency of 11 kHz. The body force field is derived out of the phase-averaged velocity measurements via the Navier-Stokes equations as suggested by Wilke[33] and is shown in fig. 2.18.

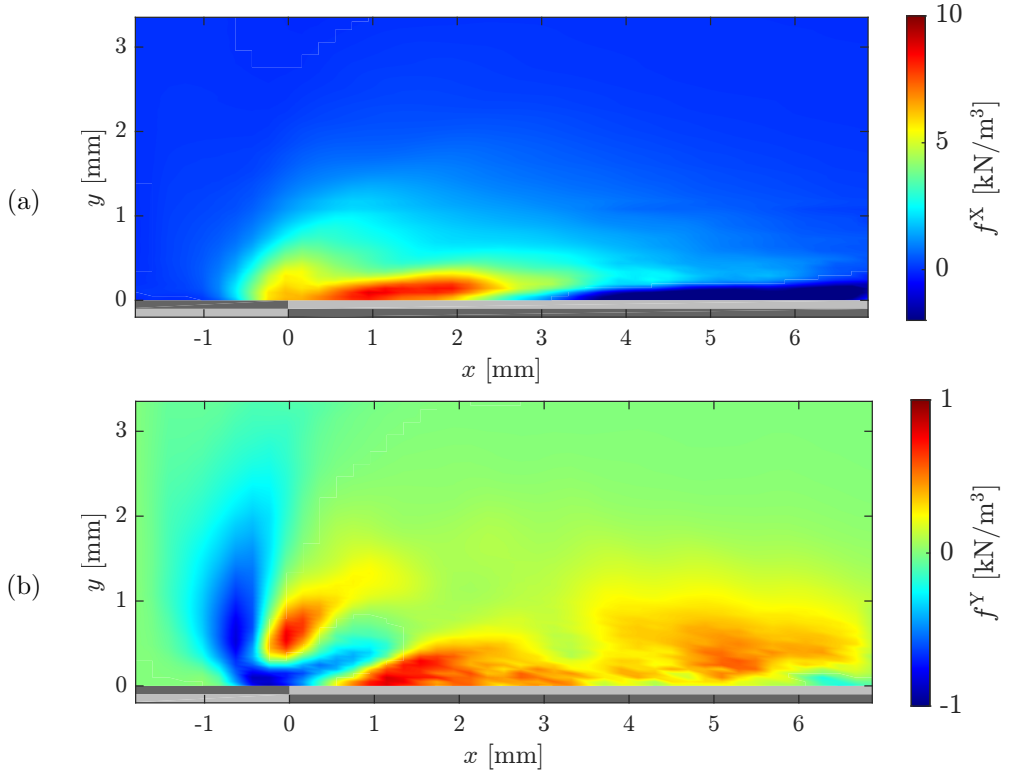

Figure 2.18.: The time-averaged body force field found, based on the experiment by Kriegseis [16]. The forces in x-direction are one order of magnitude larger than in y-direction.

Maden developed a mathematical formulation that is able to approach the topography of an experiment-based body force field. The body forces in vertical direction is neglected ($f^Y = 0$), as the phase-averaged body forces horizontal direction (f^X) are one magnitude larger.

Equation 2.25 describes the value of every point of the body force field with the multiplication of two independent equations $X(x)$ and $Y(y)$ with a variable c_0.

$$f(x, y) = c_0 X(x) Y(y) \tag{2.25}$$

A good accordance to the experimental data was found with following equations:

$$X(x) = (c_{x1}x + c_{x2}x^3)e^{-c_{x3}x}(1 + \tanh(c_{x5}x - c_{x6})) \tag{2.26}$$

$$Y(y) = (c_{y1}y + c_{y2}y^2)e^{-c_{y3}\cdot y^{\frac{1}{2}}} \tag{2.27}$$

With all coefficients $c_i \in \mathbb{R}$ and $x, y \geq 0$.

Subsequently, all coefficients c_i in 2.25, 2.26 and 2.27 are approximated to the experimental data with a least-square fit. Thus, the phase-averaged body force field in x-direction can be described by eight coefficients. Maden found an integral phase-averaged body force of $F/L = 25.45\,\mathrm{mN/m}$ with his model, compared to a value of $F/L = 25.28\,\mathrm{mN/m}$ from the PIV measurement. A surface plot of the empirical model is shown in fig. 2.19:

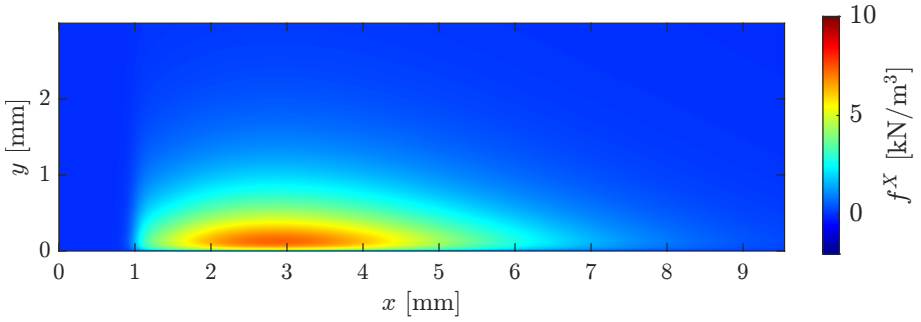

Figure 2.19.: Body force field, based on the model by Maden *et al.* [21]

Although the topography of the model matches the experimental data fairly well and sets a good benchmark for the integral body force, it shows clear deficits: The equations 2.26 and 2.27 are of pure mathematical nature, meaning they show no relation to the geometry or operation parameters of the actuator. As will be displayed in 3.3, the topography of the phase-resolved body force fields differs highly from the phase-averaged one. Hence new equations $X(x)$ and $Y(y)$ have to be found, as well as a time-dependent equation to describe each phase. In his PhD thesis, Maden provides the coefficients for a model of the body force field investigated by Kriegseis[16]. During the reconstruction of the model shown in fig. 2.19, some minor flaws of the model appeared: For example, the equations $X(x)$ and $Y(y)$ are only defined for positive values of the coordinates x and y. As shown in fig. 2.18a, the body force shows appearance also for negative x-values, meaning the position of the model relative to the coordinate system has to be evaluated in retrospect. Furthermore, the integral body force varies up to 10 % with the size of the grid cells that it is based on.

2.5.4. Comparison of Existing Models

All described models aim for a formulation of the body force field generated by a plasma-actuator that can be used as boundary conditions for CFD applications.

First, the models are discussed regarding their ability to describe phase-resolved and phase-averaged body force fields:
Only the model by Suzen provides the possibility for a phase-resolved description. Yet the according experiment was actuated with a square-wave AC voltage, so the usability for sine-wave actuation is questionable. Suzen estimates a linear relation between the actuation voltage and the magnitude of the electric field. This is in conflict to section 2.4, where a highly non-linear phase-resolved behavior the actuator is described. For phase-averaging, Shyy estimated that the discharge only acts for a small time during the cycle and reduced

the integrated body force value proportional to this time fraction. Maden on the other hand presented an empirical model that is fitted to experimental, phase-averaged body forces. As the topography of the phase-averaged body force field differs strongly from the phase-resolved fields, the equations suggested by Maden can not be applied to the phase-resolved data.

A further focus is set on the computation the body forces in both spatial directions:
The phase-averaged body force in horizontal direction is clearly dominant compared to the vertical one, hence the model by Maden neglects their influence and does not suggest a modeling approach. Shyy computes vertical body forces, yet the results are half as high as the horizontal body forces. We remember that the phase-averaged values in horizontal direction are one magnitude higher. The model by Suzen should be able to resolve the vertical direction, but the presented results only demonstrate the norm of both force directions. As examined by Kuhnhenn *et al.* [19] and confirmed in chapter 3.3, the phase-resolved body forces in horizontal and vertical direction are almost of the same order of magnitude and therefore both have to be considered for a phase-resolved model.

The model by Maden is of solely empirical nature, so only the other two are assessed regarding their physical plausibility:
As stated before, the model by Shyy calculates the maximum electric field on a physical basis, yet the further model is a coarse simplification of the discharge behavior. Regarding the model by Suzen, it should be noted that he centered the electric field originating from free charges around the embedded electrode. This resolves a plausible electric field, but it in contrary to a phenomenological explanation, as the charges are generated above the surface and can not pass through it.

This thesis does not apply the body force field models in CFD simulations to compute the velocity field. Instead, fig. 2.20 shows a comparison of the wall jets which Maden *et al.* [22] simulated with the respective body force models. The result can be seen in fig. 2.20. Here, the velocity profiles $u(y)$ are displayed for different streamwise positions (the origin of the coordinate system was set to the upper downstream corner of the exposed electrode). It is obvious that the accuracy of the wall jet computation differs strongly for the shown streamwise positions.
Though the model by Shyy was able to compute the integrated body force accurately, the poor physical causality of the model is visible in the velocity profiles. In the discharge region, the shape of the velocity profile does not resemble the experimental data, it even generates a slight back flow at $x = 3\,\mathrm{mm}$ and $y = 2\,\mathrm{mm}$. Yet, downstream of the discharge it simulates the experimental data quite acceptably. This can be explained with the accuracy of integral the body force in the discharge area that generates a mostly correct velocity profile downstream of the plasma.
At $x = 0$ the model by Suzen results in velocity peak that is approximately twice the value of the experimental data. For higher values of y, the modeled velocity decreases too soon and undershoots the experimental velocity. Further downstream, the velocity profile broadens a bit and therefore represents the experimental data better qualitatively, but the maximal velocity values are not reached anymore. This can be explained with the modeled body force maximum that is positioned further upstream and is confined horizontally. The best accordance to the experimental data for all velocity profiles is archived with the model by Maden. This is not surprising as the model is designed to reconstruct the body force field for the given actuation setup as accurately as possible.

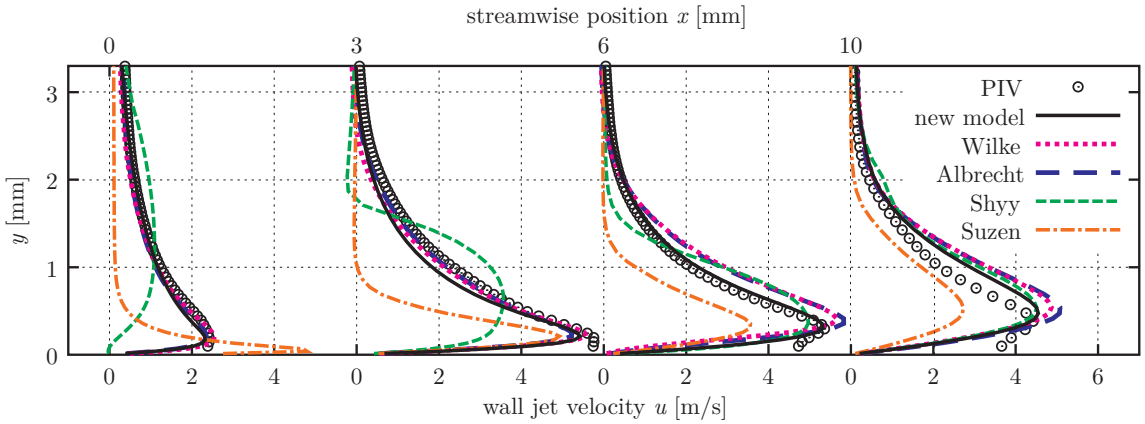

Figure 2.20.: Comparison of the wall jet generated by a body force field according to the different models. The line for "new model" refers to the model by Maden *et al.* [21, 23]. For "Wilke", the body forces were derived from the PIV velocity data via the Navier-Stokes equations and for "Albrecht" via the vorticity equation. Summarized by Maden *et al.* [22].

Figure 2.20 proves the influence of the topography of the modeled body force field on the simulated velocity field. The models by Shyy and Maden both compute acceptable phase-averaged, integrated body force values, yet the model by Shyy does not simulate satisfying velocity profiles. In future works the influence of the body force field topography has to be examined, to lay down quantitative requirements for the topography of new body force models.

The following table gives a summary of the different models, regarding the aspects that were discussed before. In conclusion, none of the known model formulations fulfills all requirements. Especially the lack of a phase-resolved model that is able to calculate both dimensional components of the body force shows the necessity of a new modeling approach. An evaluation of the new model is included in the last line for a complete overview.

model	body force integrated and phase-averaged	body force topography	physical correctness	both directions	velocity profile	phase resolution
Shyy	✔	✗	✗	✔	✗	✗
Suzen	?	✔	✔	✔	✔	✔
Maden	✔	✔	✗	✗	✔	✗
New Model	✔	✔	✔	✔	?	✔

Table 2.2.: Summary of the characteristics of the described body force models. Colored marks indicate good performance, black marks sufficient one. Suzen does not specify the value of the integrated, phase-averaged body force. For a better comparison, the new model that is introduced in this thesis is listed as well.

3. Experimental Setup

The empirical model that will be described later on is based on the data by Hehner *et al.* ([12, 13]) For an improved understanding of this basis, their experimental setup will be outlined. Subsequently, the derivation of body forces out of the velocity measurements will be retraced and discussed.

3.1. DBD Actuator and PIV Setup

The experiment was set up in a blower-type wind tunnel at the Institute of Fluid Mechanics at the KIT (Karlsruhe Institute of Technology). The plasma actuator was installed on a flat plate that features an elliptic leading edge to minimize friction effects upstream of the actuator. Both electrodes are made out of copper with an area of 2.5 x 10 mm^2, and the dielectric is composed of Kapton tape with a thickness of 0.3 mm. A high-voltage generator (Minipuls 2, GBS Elektronik GmbH) supplies the actuator with a sinusoidal waveform with peak-to-peak voltage of $V_{pp} = 12\,\mathrm{kV}$ at a frequency of $f_{ac} = 10\,\mathrm{kHz}$.

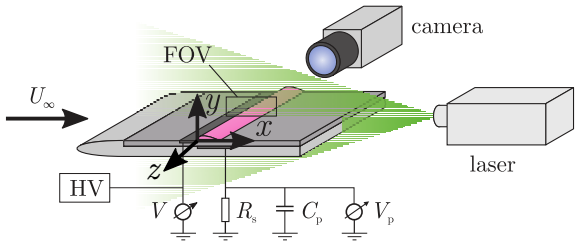

Figure 3.1.: Sketch of the experimental setup in the test section according to Hehner *et al.* [12, 13]. The displayed coordinate system will be referred to in all further explanations.

The measurement points in relation to the discharge characteristics are displayed in fig. 3.2. Therefore the slope of the voltage is plotted versus the charge of the actuator (solid black line). The area within the Lissajous line describes the electrical power of the actuator. The red line refers to the electric current along the slope. The first and third quarter of the phase is dominated by high discharges as indicated by the peaks. In contrast the zones of collapsed discharge are framed by dashed boxes. The yellow dots mark the points of PIV-velocity measurements.

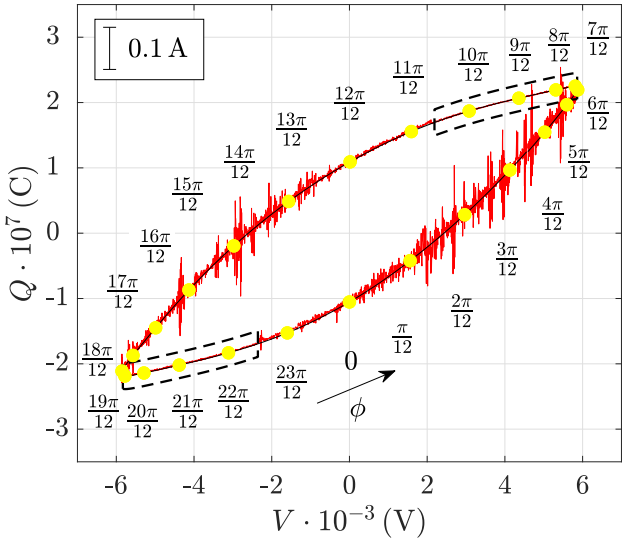

Figure 3.2.: Electrical characteristics of the DBD plasma actuator, adapted from Hehner *et al.* [12, 13].

The PIV high-speed system consists of a Nd:YLF dual-cavity laser (Quantronix Darwin Duo) and a Photron Fastcam SA4 camera that is placed outside the test section. The camera was equipped with a Nikon AF micro Nikkor 200 mm f/4D IF-ID lens, and an extension of 108 mm total length was additionally applied, in order to simultaneously obtain a suitable object distance and high spatial resolution. It was operated at $f_{\#} = 8$ and imaged a field of view (FOV) of $9 \times 4.5\,\mathrm{mm}^2$ yielding a spatial resolution of 114 px/mm. The used coordinate system is sketched in fig. 3.1.
The flow was visualized with di-ethyl-hexylsebacat (DEHS) tracers, resulting in a Stokes number of $Stk \leq 6.66 \times 10^{-2}$. For each PIV run 5400 image pairs were recorded, converting into 225 image pairs per phase position. The repeatability of the experiments was assured taking three independent PIV runs for each tested free stream velocity.
A multigrid/multipass approach processed the pictures, yielding a final interrogation window size of 32×16 px^2 with overlaps of 50 %. The accuracy of the PIV-velocity fields was evaluated with an uncertainty-quantification strategy, as reported by Sciaccitano and Wieneke [27]. The strategy determines the uncertainty of the time-averaged velocity data from the standard deviation of the velocity field, being computed with fluctuation components and measurement errors. Individual analysis of the uncertainty associated to each single PIV case with plasma actuation resulted in a maximum uncertainty of $< 2\,\%$.

3.2. Derivation of Body Forces

The components f_i of body force field were derived from the velocity data with application of the two-dimensional Navier-Stokes equations as described by Wilke [33] and applied by Kuhnhenn *et al.* [19]:

$$f_i = \underbrace{\rho \frac{\partial u_i}{\partial t}}_{\substack{\text{time} \\ \text{dependency}}} + \underbrace{\rho u_j \frac{\partial u_i}{\partial x_j}}_{\text{convection}} - \underbrace{\mu \frac{\partial^2 u_i}{\partial x_j \partial x_j}}_{\text{diffusion}} \tag{3.1}$$

As proposed by Wilke, the air is approximated as a Newtonian, incompressible fluid with constant dynamic viscosity μ and negligible pressure gradient. The convection and diffusion components of the force are calculated directly from the respective phase velocity

$u_i(x, y, \varphi)$. It should be noted that the numeric derivation was computed with the gradient function by Matlab that calculates central differences, resulting in a second-order error. The time-dependent forces were approximated via central differences in dependence of the phase step $\Delta\varphi$ between two measurements:

$$\frac{\partial u(x,y,t)}{\partial t} \approx \frac{u(x,y,\varphi+\Delta\varphi) - u(x,y,\varphi-\Delta\varphi)}{t(\varphi+\Delta\varphi) - t(\varphi-\Delta\varphi)} \tag{3.2}$$

As equation 3.2 is a numeric approximation, its accuracy increases with a greater number of distinguished phases. The body force $f_i(x, y, \varphi)$ integrated across the control volume (CV) is not only assumed to be a good indicator of the quality of body force models (as applied in section 2.5.4), but is also used to compare the phase-resolved influence of the different terms in equation 3.1. As the CV approximately consists of a two-dimensional sheet, the integral body force is described as integral body force $F^i(\phi)$ per actuator length L and will be abbreviated only as f^i_{int}:

$$\begin{aligned} f^X_{\mathrm{int}}(\varphi) &= \frac{F^X_{\mathrm{int}}(\varphi)}{L} = \iint_{CV} f^X(x,y,\varphi)\,\mathrm{d}A = \Delta x \cdot \Delta y \cdot \sum_{y=y_{\min}}^{y_{\max}} \sum_{x=x_{\min}}^{x_{\max}} f^X(x,y,\varphi) \\ f^Y_{\mathrm{int}}(\varphi) &= \frac{F^Y_{\mathrm{int}}(\varphi)}{L} = \iint_{CV} f^Y(x,y,\varphi)\,\mathrm{d}A = \Delta x \cdot \Delta y \cdot \sum_{y=y_{\min}}^{y_{\max}} \sum_{x=x_{\min}}^{x_{\max}} f^Y(x,y,\varphi) \end{aligned} \tag{3.3}$$

For the sake of completeness the latter part of the equations shows the discrete implementation of the integration for a grid with constant cell sizes of Δx and Δy.

Evaluations of the force components as shown in equation 3.1 have proved the clear dominance of the time-dependent term, as it is several orders of magnitude greater as both the convection and diffusion. In conclusion the model described later will be focused on reproducing the phase-resolved body force fields.

3.3. Phase-Resolved Body Force Fields

The results of the body force computations are shown in fig. 3.3 and fig. 3.3. The underlying PIV measurements can be found in the appendix: fig. A.1 and fig. A.2.

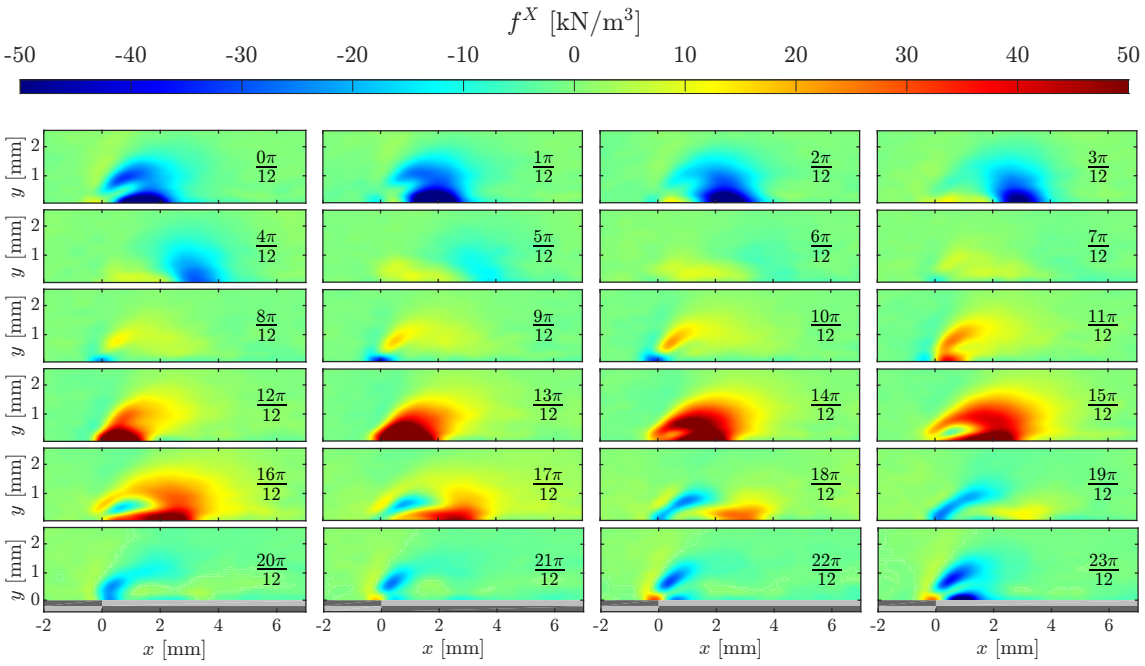

Figure 3.3.: Phase resolved body force fields in horizontal direction (f^X) by Hehner *et al.* [12, 13].

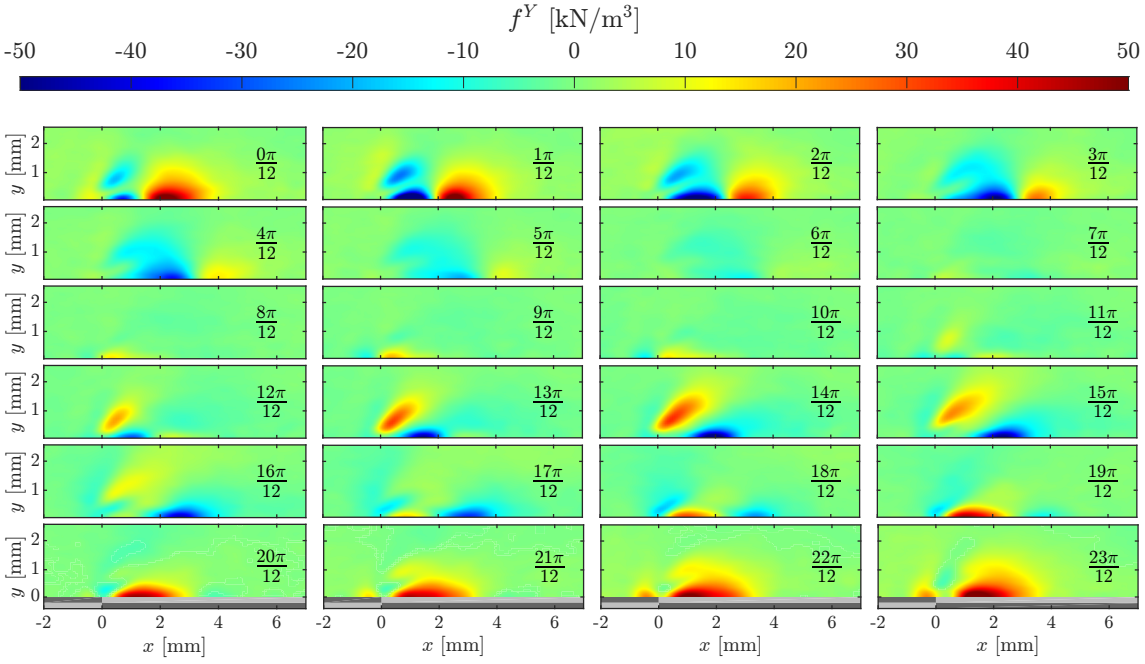

Figure 3.4.: Phase resolved body force fields in vertical direction (f^Y) by Hehner *et al.* [12, 13].

The body force fields were integrated as shown in eq. 3.3. The results are displayed in fig. 3.5. These results are in accordance to the investigations by Enloe *et al.* [7]. He divided the actuation phases in a forward- and a backward stroke (marked in fig. 3.5) and found differences in their contribution to the jet velocity. He traced this effect back to the "self-induced drag" that counteracts the jet formation and is more powerful during the backstroke. Yet the experiment by Enloe was only able to resolve the influence of the horizontal jet or rather wall friction. Nevertheless the self-induced drag explains the higher

values for positive integrated body forces than for negative ones in x-direction, leading to a phase-averaged positive body force.

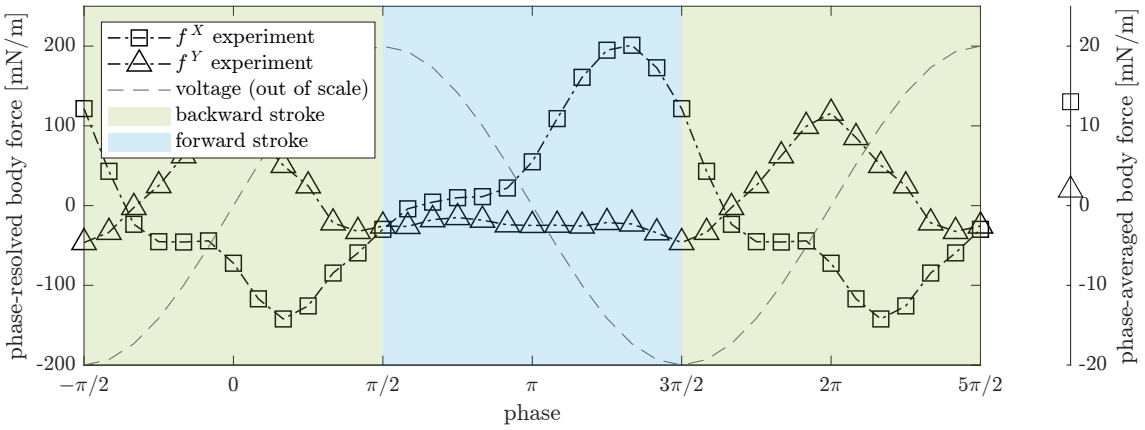

Figure 3.5.: Phase-resolved integrated and phase-averaged body forces in both directions. The body forces are based on experimental data by Hehner *et al.* [12, 13], the distinction of backward and forward stroke is according to Enloe *et al.* [7].

4. Empirical Body Force Modeling

In this chapter a new approach for an empirical model of the body forces originating from dielectric barrier discharge will be described. First a rationale will introduce the concept of body force potentials. Subsequently, the positioning of body force potentials is discussed, which then leads towards the characterization of the potentials and their gradients. These gradients are implemented in a system of linear equations which is approximated with a least-square method.

4.1. Potential-Based Approach for Empirical Modeling

The idea of a body force model with the basis of positioning potentials originates from the phase-resolved body force measurements by Hehner [12, 13] (figs. 3.3 and 3.4). At first sight, it seems as if there are regions in the CV that act as a source, or sink, of body force. These sources and sinks move and change their magnitude in dependence of the phase progression. Thus, describing the body force field by evaluating the position and intensity of a number of potentials appears evident.
As mentioned before, in fluid dynamics, the gradient of the velocity potential describes the velocity field, while in electrostatics the gradient of the electric potential is the negative electric field. The electric field is a value for the force generated by one charge multiplied with another charge, acting on this first charge.
Hence, a *body force potential* is introduced, inspired both by the topology of the phase-resolved body force measurements as well as the analogies to velocity and electric potentials. In these scientific fields, the spatial components of the velocity (or electric field) is described by the gradient of single, superimposed velocity (or electric) potentials. Following this analogy, the gradient of the body force potential computes the spatial components of the body force:

$$\nabla\phi = \begin{pmatrix} f^X \\ f^Y \end{pmatrix} \tag{4.1}$$

This means, the new model is centered around finding a spatial distribution of body force potentials. This distribution aims to resemble the experimental body forces through the gradient of the super positioned potentials. First, three different basic concepts are evaluated with the position $(x_0(t), y_0(t))$ of the potentials in the CV. An additional variable

to describe the potential is its magnitude $M(t)$ that will be introduced later. The concepts are visualized through the example of the experimental body force in x-direction at the phase $2\pi/12$ field by Hehner on the left-hand side. Each of the right-hand side pictures shows an estimation of the resulting potential positions and magnitudes.

1. $\phi(M(t),\ x_0(t),\ y_0(t))$: The potentials in the numeric field that vary their x and y position and magnitude M.

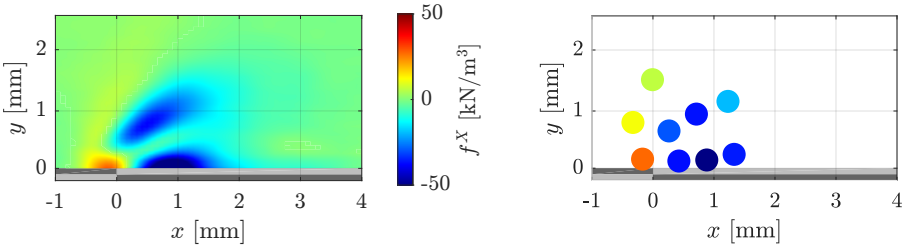

2. $\phi(\pm M,\ x_0(t),\ y_0 = 0)$: The potentials with constant positive or negative magnitude are located on the actuator surface ($y = 0$), but vary their x-position.

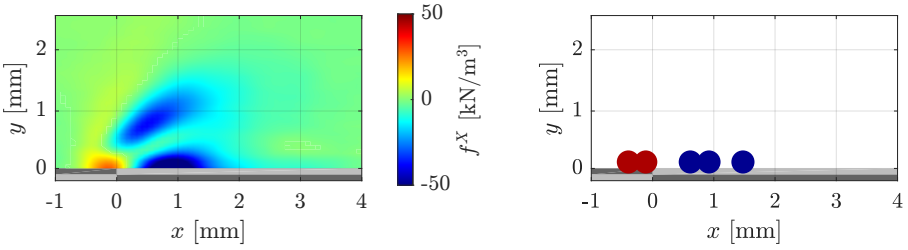

3. $\phi(M(t),\ x_0(t) = x_k,\ y_0 = 0)$: A number of $k_{\max}$ potentials are located on the actuator surface equidistantly, comparable to pearls on a string, and only vary in their magnitude. $(k = 1, 2, 3...k_{max})$

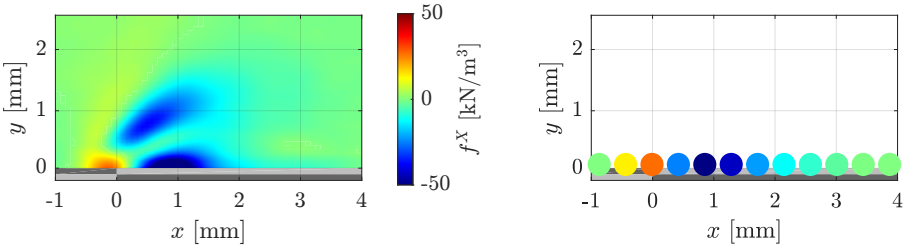

The introduced concepts demonstrate different advantages and disadvantages. Concept (1) promises good accordance with the experimental data, as local body force maxima and minima can be described throughout the CV. Nevertheless, it shows a lack of physical correctness as the force-generating, charged particles are not expected to exist in the whole CV. Also, the gradient of a single potential has a shape that is displayed in fig. 4.2b, meaning that the formation of a single "maximum" at one point is not achievable without generating a "minimum" next to it. This impedes the intuitive positioning of potentials in the field.
In a model closer to physical effects, the positions of charges and therefore their corresponding potentials are expected to be located close to the electrodes. As a simplification they are positioned directly on the actuator surface, as suggested by concept (2) and (3). These concepts are expected to generate similar solutions. Yet, as will be shown in fig. 4.4, the topography generated by the superposition of two gradients is highly dependent on their distance. In order to minimize this difficulty, concept (3) was chosen. As the single potential is only dependent on one variable (M), the concept is expected to show promising results, while the implementation is comparatively simple. In addition, this concept highly reduces the complexity of the description of the body force topography. The whole

field can be determined only by a single potential line at the actuator surface.

4.2. Characteristics of Positioned Potentials

As mentioned in 2.2, there are different formulations for single point potentials. The ones found in literature, $\phi = \ln(r)$ and $\phi = 1/r$ show a singular point for $r \to 0$, meaning that the potential heads for infinity. This causes difficulties in the calculation. First, this issue was circumvented by implementing the potential $\phi = \exp(-r^2)$ which does not have a singular point. None the less, this Gaussian formulation was dismissed as it is not as numerically stable as the other two and shows poorer results when comparing integral body forces (as will be shown in 5.1.3).
To avoid numerical problems due to the singular nature of the logarithm and broken rational function, the singular points were not set to the knots of the numerical grid but insted into the gaps between the knots, as sketched in fig. 4.1. Thanks to this method, the value of the potential and its gradient is decreased far enough to be computable at the evaluated grid knots.

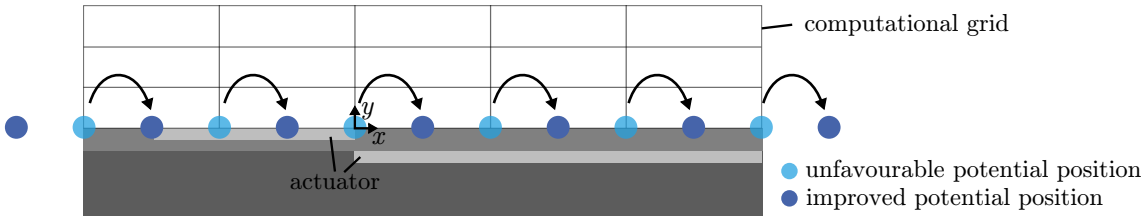

Figure 4.1.: Improved positioning of single point potentials to avoid computational errors due to the singularity

Figure 4.2 shows the topology resulting in the CV by positioning a single potential as well as its derivatives, in respect to both directions. Due to the high gradient of the logarithm close to the singular point, the derivatives display values that are several orders of magnitude higher than the potential itself on the same computation grid.

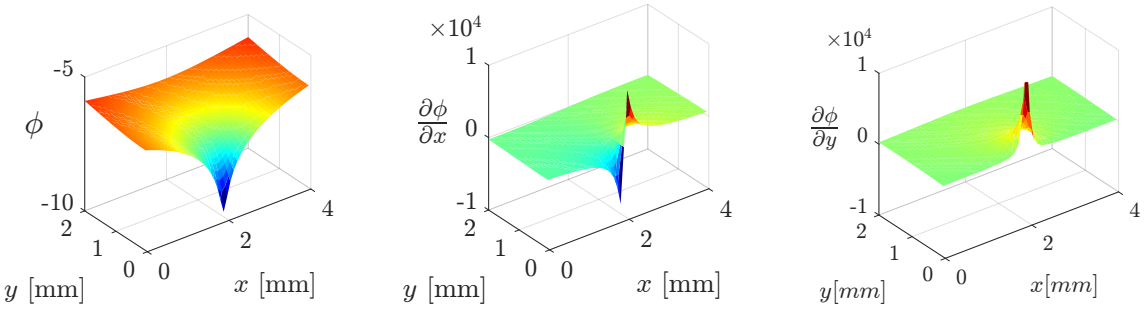

(a) Potential in CV

(b) Potential derivative with respect to x

(c) Potential derivative with respect to y

Figure 4.2.: A single potential positioned in CV at $x = 2\,\text{mm}$ with both derivatives

The potentials described by this new model will be super positioned. To visualize the effects that occur by overlaying the gradients of potentials, in fig. 4.3, potentials of the same magnitude are superimposed for different distances in relation to the grid cell length ($\Delta x = 8.3 \times 10^{-2}\,\text{mm}$).

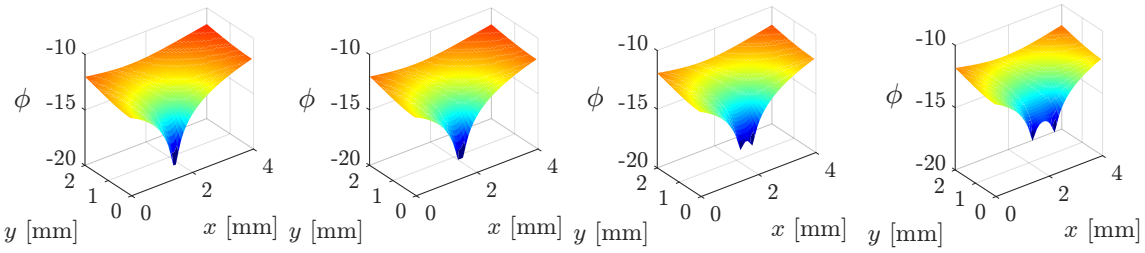

(a) Distance $1 \cdot \Delta x$ (b) Distance $2 \cdot \Delta x$ (c) Distance $5 \cdot \Delta x$ (d) Distance $10 \cdot \Delta x$

Figure 4.3.: The result of overlaying two potentials at varying distances, in relation to the grid cell length $\Delta x = 8.3 \times 10^{-2}\,\mathrm{mm}$

Figure 4.4 displays the result of the derivation of the super positioned potentials in x-direction. Note how for the large distance of ten grid cell (4.4d) the derivations are clearly separated from another. For decreasing distances, the peaks start interacting and form smaller interference peaks. A distance of one grid cell seems to eliminate these interference peaks, but this effect could also be due to the relatively coarse numerical grid.

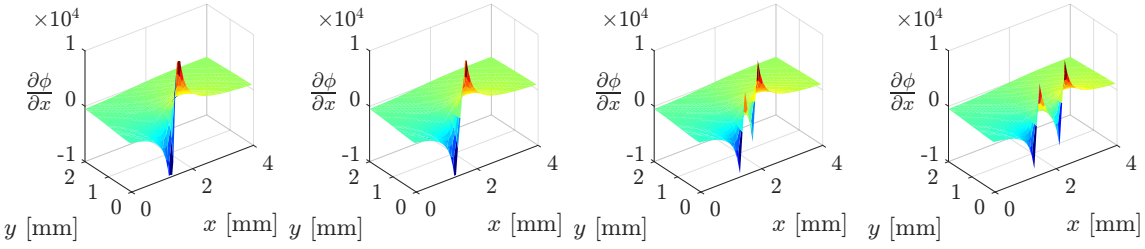

(a) Distance $1 \cdot \Delta x$ (b) Distance $2 \cdot \Delta x$ (c) Distance $5 \cdot \Delta x$ (d) Distance $10 \cdot \Delta x$

Figure 4.4.: The result of overlaying the gradients with respect to x of two potentials at varying distances, in relation to the grid cell length $\Delta x = 8.3 \times 10^{-2}\,\mathrm{mm}$

The derivation of the potentials with respect to y is shown in fig. 4.5. Theoretically, this derivation of the axially symmetrical potential should show a behavior similar to the derivation in x, with a positive and negative maximum. Yet, as body forces only affect the air around the actuator and not on the electrodes or dielectric, this negative part of the derivation field is not relevant. The result is a far more intuitive derivation field, with single spikes summed up for low distances as shown in fig. 4.5c. For the lowest distance of one grid cell (fig. 4.5a), it seems that the derivations form one single broadened peak, but it is expected to see single peaks for a finer numerical grid.

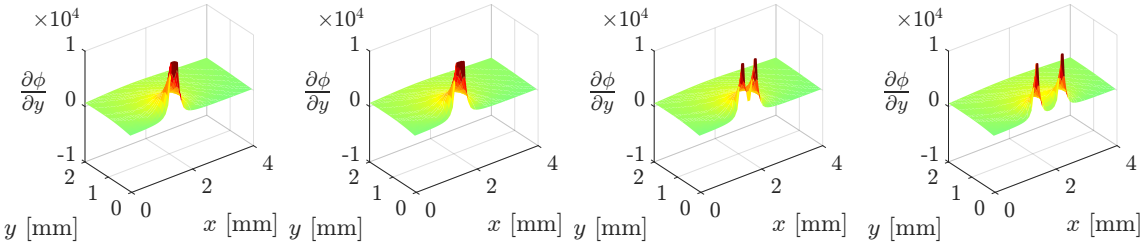

(a) Distance $1 \cdot \Delta x$ (b) Distance $2 \cdot \Delta x$ (c) Distance $5 \cdot \Delta x$ (d) Distance $10 \cdot \Delta x$

Figure 4.5.: The result of overlaying the gradients with respect to y of two potentials at varying distances, in relation to the grid cell length $\Delta x = 8.3 \times 10^{-2}\,\mathrm{mm}$

Thus, as a baseline state, the logarithmic potentials will be positioned with a distance of

the length of the measurement grid cells used by Hehner, as shown in fig. 4.1. Adding at one potential at both ends of the line of potentials was found to be useful, hence the baseline number of potentials is one more than the number of grid cells in x-direction (resulting in 118 potentials in this case).

A further note concerns the unit of body force potentials. In accordance to equation 4.1, the spatial derivation of the body force potential should be in N/m^3. This conclusion leads towards the unit of body force potentials: N/m^2. For improved clarity, body force potentials will be displayed without unit throughout this thesis, yet its meaning will be contextualized if needed.

4.3. Numerical Setup

As the new model will be fitted to the experimental data by Hehner [12],[13], his measurement grid was taken as a basis for calculations. It comprises 117 cells in x- and 41 cells in y-direction, with a cell size of 8.3×10^{-2} mm x 6.3×10^{-2} mm. The numerical process is derived from the working principles of the finite volume method, but with an evaluation at the knots instead of at the center of the volume.

First, the formulation of the potential, described by the distance or radius r from the singular point in an axial-symmetric formulation, is transformed into Cartesian coordinates. This is done applying the Theorem of Pythagoras, with the position x_0, y_0 of the single potential.

$$r = \sqrt{(x - x_0)^2 + (y - y_0)^2} \tag{4.2}$$

By application to 2.5, a line potential and its derivations are expressed in Cartesian coordinates:

$$\phi = \frac{M'}{2\pi} \ln(\sqrt{(x - x_0)^2 + (y - y_0)^2}) \tag{4.3}$$

$$\begin{aligned} \frac{\partial \phi}{\partial x} &= \frac{M'}{2\pi} \frac{x - x_0}{(x - x_0)^2 + (y - y_0)^2} \\ \frac{\partial \phi}{\partial y} &= \frac{M'}{2\pi} \frac{y - y_0}{(x - x_0)^2 + (y - y_0)^2} \end{aligned} \tag{4.4}$$

As stated before, the potentials ϕ_k are positioned on the actuator surface ($y_0 = 0$) equidistantly, similar to a string of pearls. The gradient of each potential spreads into the CV individually. As shown in equation 4.5 and 4.6, the resulting body force in one cell $f_{x,y}$ in the grid is a superposition of the gradient of every potential of the string of pearls on this cell:

$$f^X_{x,y} = \frac{\partial}{\partial x} \sum_{k=1}^{max} \phi_k = \sum_{k=1}^{max} \frac{\partial \phi_k}{\partial x} = \sum_{k=1}^{max} \frac{1}{2\pi} \underbrace{\frac{x - x_0}{(x - x_0)^2 + (y - y_0)^2}}_{A^X_{M_k,x,y}} M'_k \tag{4.5}$$

$$f^Y_{x,y} = \frac{\partial}{\partial y} \sum_{k=1}^{max} \phi_k = \sum_{k=1}^{max} \frac{\partial \phi_k}{\partial y} = \sum_{k=1}^{max} \frac{1}{2\pi} \underbrace{\frac{y - y_0}{(x - x_0)^2 + (y - y_0)^2}}_{A^Y_{M_k,x,y}} M'_k \tag{4.6}$$

For further simplification the constant $1/2\pi$ was included in the magnitude M_k: $M_k = M'_k/2\pi$. In conjunction with the unit of the body force, the unit of the magnitudes can be derived from eq. 4.3 and is equal to the unit of the body force potential: $\mathrm{N/m^2}$.
Theoretically, the gradient of one string of potentials should resolve both components of the body force f^X and f^Y. This will be investigated in chapter 5.1.2, but first the X- and Y-dimensions are decoupled. This results in two vectors that contain the magnitudes of every body force potential on the string of pearls: $\vec{M}^X$ and $\vec{M}^Y$. The goal of further calculations then becomes the determination of these body force potential magnitudes. Therefore the latter equations 4.5 and 4.6 are summed up as shown in eq. 4.7. The force in every point (x,y) is the sum of the influence $(A^{X/Y}_{M_k,x,y})$ of each single potential $M^{X//Y}_k$:

$$\begin{aligned} f^X_{x,y} &= \sum_{k=1}^{max} A^X_{M_k,x,y} M^X_k \\ f^Y_{x,y} &= \sum_{k=1}^{max} A^Y_{M_k,x,y} M^Y_k \end{aligned} \tag{4.7}$$

With the information above, a system of equations is set up to relate the body force potentials to the empirical body force measurements by Hehner ($\vec{f}^X$, respectively $\vec{f}^Y$), in the common form as shown in equation 4.8 with the solution vector $\vec{M}^X$ (respectively $\vec{M}^Y$):

$$\begin{aligned} \mathbf{A}^X \vec{M}^X &= \vec{f}^{\,X} \\ \mathbf{A}^Y \vec{M}^Y &= \vec{f}^{\,Y} \end{aligned} \tag{4.8}$$

Inserting 4.7 in 4.8, the full equation system is shown. It is noted independent from the direction and can be mapped to either direction by inserting the respective values of $\mathbf{A}^i$ and $\vec{f}^{\,i}$.

$$\begin{pmatrix} A_{M_1,x_1,y_1} & A_{M_2,x_1,y_1} & \cdots & A_{M_{max},x_1,y_1} \\ A_{M_1,x_2,y_1} & A_{M_2,x_2,y_1} & \cdots & A_{M_{max},x_2,y_1} \\ \vdots & \vdots & \ddots & \vdots \\ A_{M_1,x_{max},y_1} & A_{M_2,x_{max},y_1} & \cdots & A_{M_{max},x_{max},y_1} \\ A_{M_1,x_1,y_2} & A_{M_2,x1,y_2} & \cdots & A_{M_{max},x_1,y_2} \\ \vdots & \vdots & \ddots & \vdots \\ A_{M_1,x_{max},y_{max}} & A_{M_2,x_{max},y_{max}} & \cdots & A_{M_{max},x_{max},y_{max}} \end{pmatrix} \begin{pmatrix} M_1 \\ M_2 \\ \vdots \\ M_{max} \end{pmatrix} = \begin{pmatrix} f_{x_1,y_1} \\ f_{x_2,y_1} \\ \vdots \\ f_{x_{max},y_1} \\ f_{x_1,y_2} \\ \vdots \\ f_{x_{max},y_{max}} \end{pmatrix} \tag{4.9}$$

This matrix A in its baseline-state as in 4.9 has the dimension 41 x $(41 \cdot 118)$. The number of columns depends on the number of potentials. As stated in section 4.2, the baseline state comprises 118 potentials. Every line in the equation system describes a single cell in the numerical grid, thus the matrix A comprises $41 \cdot 118 = 4838$ lines. Consequently, the equation system is highly overdetermined and the solution vector $\vec{M}$ has to be approximated.
The equation system was implemented in Matlab R2020a and approximated with by the *LSMR* code by Fong and Saunders [8]. It is related to least-square algorithms, but is

numerically more robust and generally terminates faster. In the basic configuration it minimizes the value of

$$\|A^i \vec{M}^i - \vec{f}^{\,i}\|^2 \tag{4.10}$$

In chapter 5 different configurations of the new model are evaluated. Unless otherwise stated, the x- and y- directions are always computed independently using the same $LSMR$-function, but varying in the derivation of the potential field ($\vec{A^X}$, respectively $\vec{A^Y}$) and the experimental body force vector ($\vec{f}^{\,\mathrm{X}}$, respectively $\vec{f}^{\,\mathrm{Y}}$) of course.
The full body force field generated by the new model is computed by multiplying the matrix A^i to the solution vector $\vec{M}^i$:

$$\begin{aligned} \vec{f}^{\,\mathrm{X}}_{\mathrm{newmodel}} &= A^X \, \vec{M}^X_{\mathrm{solution}} \\ \vec{f}^{\,\mathrm{Y}}_{\mathrm{newmodel}} &= A^Y \, \vec{M}^Y_{\mathrm{solution}} \end{aligned} \tag{4.11}$$

The potential field can be computed in the same way. The graphic result for a line of constant potential magnitudes is shown in fig. 4.6. The potential field 4.6a shows a major minimum in the center of the potential line as the single potentials accumulate most at this point. In figure 4.6b, the derivation of the outer potentials show their last minimum and maximum. These structures will be referred to as flaps. Due to the linear increasing nature of the logarithm the plane between these points is inclined. As a result of positioning the potentials exactly on the actuator surface, the derivation of superimposed potentials with respect to y does not show the same interference behavior as the derivation with respect to x (shown in 4.4). This means that the derivation with respect to y (4.6c) can be derived more intuitively from the potential field, as the positive magnitude of a single potential leads to a positive derivation for $y > 0$ and vice versa.

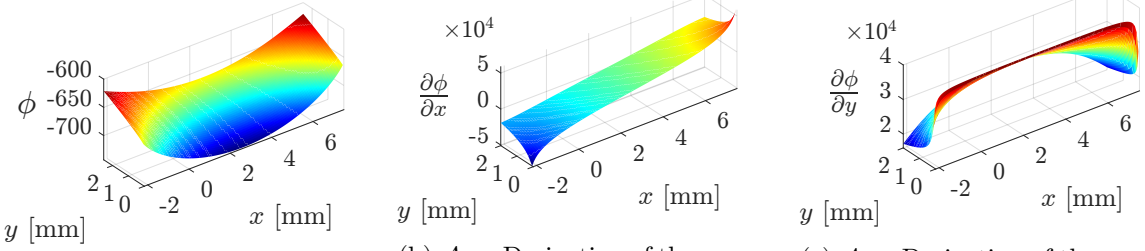

(a) Potential field

(b) A_X : Derivation of the potential with respect to x

(c) A_Y : Derivation of the potential with respect to y

Figure 4.6.: The potential and its derivations, resulting from a line of potentials of constant magnitude The potentials are positioned with a constant distance of one grid cell along the whole abscissa at $y = 0$. Note that in contrast to the figures in the previous section, here the field dimensions resemble the experimental CV and the ordinate of the derivation in y-direction does only display positive values.

5. Results and Discussion

In this chapter the new model is applied. First, a baseline state of the model is evaluated. On this basis, various configurations are computed and discussed. As this is the first attempt at a potential-based empirical model for the plasma-induced body forces, different configurations are recorded, despite not directly improving the model. This will enhance insight into the model behavior, in order to facilitate future investigations. A complete documentation of all configurations and phase-resolved results is attached in the appendix. The model was compared to the experimental data regarding its ability to reproduce the topography of the body force field and the integral body force (phase-averaged as well as phase-resolved). The computed magnitudes of the body force potentials themselves are evaluated regarding their validity, as they are expected to resemble a plausible distribution of charged particles in the CV. Finally, the new model will be brought into context with existing modeling approaches.

5.1. Modeling Results

Hehner *et al.* [12, 13] examined 24 AC-phases. In order to maintain a comprehensive overview, not every phase is displayed and evaluated. Instead, six phases were chosen: 0, $2\pi/12$, $8\pi/12$, $12\pi/12$, $14\pi/12$ and $20\pi/12$. These display a representative mix of phases with strong positive or negative values (relating to a high discharge) as well as nearly neutral phases. For simplification, the abbreviation *EBFs* will describe the experimental body forces by Hehner *et al.* [12, 13], *PMs* the computed potential magnitudes and *MBFs* the new, modeled body forces. The unit of body force potentials was discussed in section 4.2 and will contextualized further in section 5.2.2. Yet, especially for configurations with implausible PM courses, the units do not refer to physical quantities. Therefore, the PMs will be indicated without unit.

5.1.1. Baseline State

This configuration of the numerical setup is the most puristic. The x-and y-direction are computed independently and the logarithmic line potentials are positioned along the actuator surface with a distance of one grid cell.

X-Direction

A comparison of the experimental data to the new model is shown in fig. 5.1. The left column comprises the EBFs for the chosen phases. The central column displays the computed magnitudes of the body force potentials that are positioned in a single line on the

actuator surface as discussed in 4.1. The MBFs in the right column are computed by inserting the PMs into the equation system, as shown in eq. 4.11.

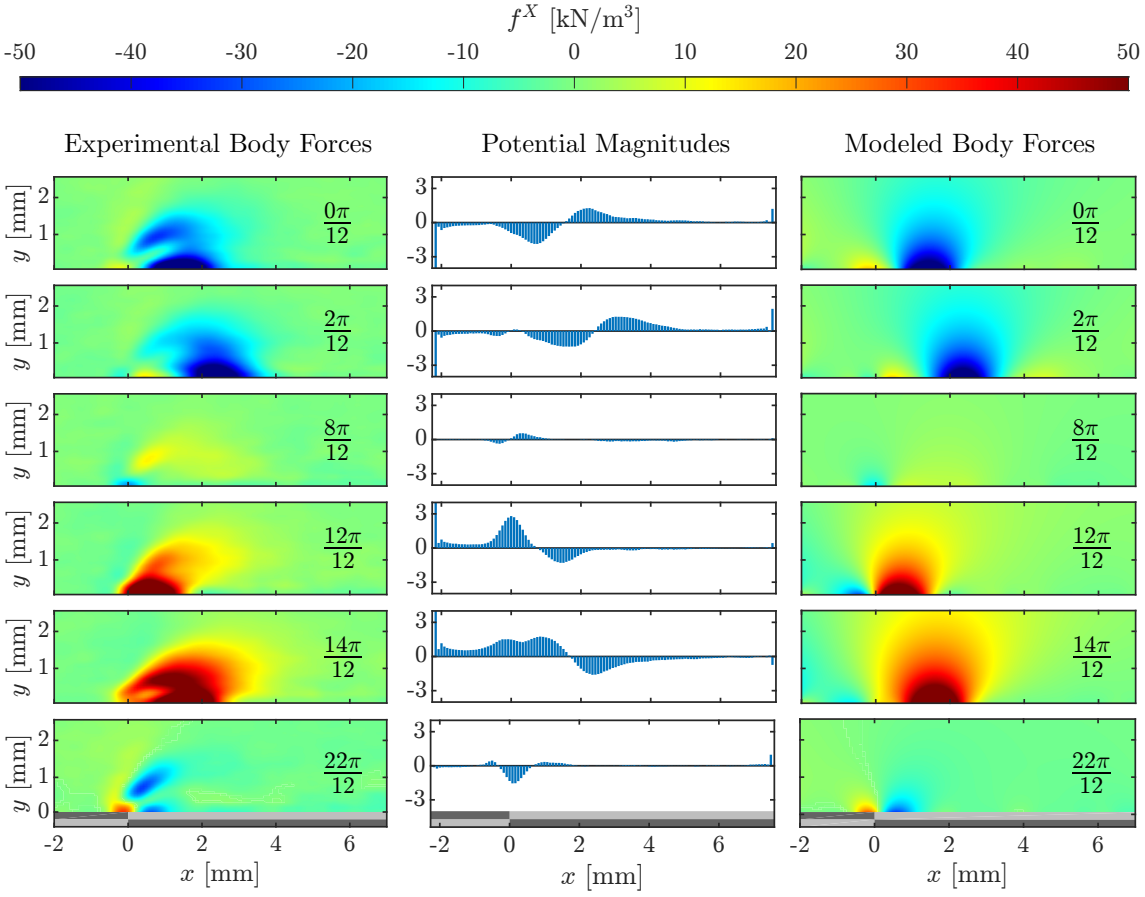

Figure 5.1.: Baseline state: Comparison of the experimental data, the computed magnitudes of positioned potentials and the resulting body force field in x-direction for chosen phases. EBFs according to Hehner *et al.* [12, 13].

A primary discussion of the new model is done on the basis of the first line of figures, referring to phase $0\pi/12$. The PMs show a nearly continuous course with a clear zeropoint at $x \approx 1.5\,\text{mm}$. This zeropoint is slightly shifted compared to the respective one in the EBFs ($x \approx 0.5\,\text{mm}$). Yet this position of the zeropoint is resolved quite accurately in the MBFs.
Both outer values of the PMs are about twice as high as the other maxima. The reason for this behavior can be found in 4.6b. The outer potentials result in a flap-like shape of the derivation field. The fitting algorithm tries to balance these flaps, resulting in the displayed outer peaks of the PMs. A slight yellow shadow on the left side of the MBFs indicates an influence of these peaks. The flaps in the MBFs are displayed more clearly in the 3D-plot of the MBFs, to bee seen in fig. 5.4. These peaks will occur in various PM sets in the following chapter and will be cut off when required for an improved visualization of the remaining PMs.
Comparing the EBFs and MBFs, a clear disadvantage of the chosen positioning of the potentials is obvious: The new model is not able to resolve topographies as the second local maximum in the body force that is located at $x \approx 1\,\text{mm}$ and $y \approx 1\,\text{mm}$. Never the less it is able to generate body force maxima with a slight skewness as shown for $14\pi/12$. Here an otherwise symmetric maximum is skewed with the neighboring minimum.

When regarding the PMs for different phase progressions, it becomes evident how a strong body force field generates higher PMs, compared to phases with low experimental body forces. Intuitively, this connection seems inaccurate, as the computed MBFs only depend on the slope of the potential field. Here, it should be kept in mind that the body force field rises from values close to zero at the edges of the CV to its maximum within. In order to follow this ascent, the derivatives of the PMs must have high values as well, resulting in higher values of the PMs themselves.

Y-Direction

While first correlations of the PMs in x-direction to spatial charge distributions can be estimated in x-direction, the results of the y-direction in fig. 5.2 are not straightforward. For most phases, the PMs show peaks altering in different directions (eg. $2\pi/12$ and $22\pi/12$). Yet the resulting MBFs show the expected correlations to the EBFs, caused by the envelope of the peaks. Never the less, especially these strongly implausible PMs indicate the numerical failure of the modeling in y-direction. Further evaluations offer reasons for this failure in chapter 5.1.6.

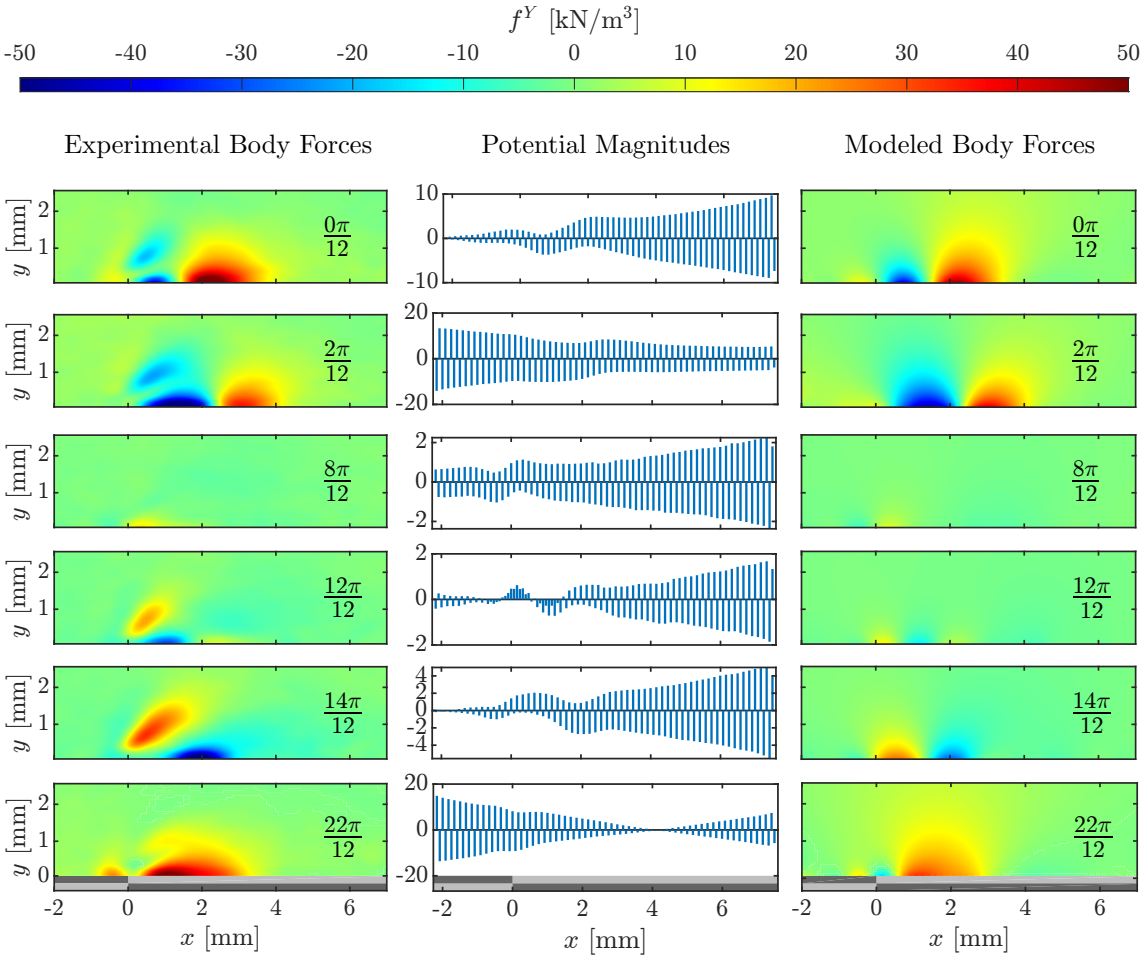

Figure 5.2.: Baseline state: Comparison of the experimental data, the computed magnitudes of positioned potentials and the resulting body force field in y-direction for chosen phases. Note that the potential magnitudes spread over two orders of magnitude due to numerical flaws. Therefore the ordinate axes are not uniform. EBFs according to Hehner *et al.* [12, 13].

Integrated Phase-Resolved and Phase-Averaged Results

In fig. 5.3, the integrated body forces of the MBFs are compared to those of EBFs. It is evident that the MBFs represent the original data quite accurately for phases with low integral body forces. For high integral body forces, the MBFs overshoot the EBFs slightly. This can be explained with the example of phase $14\pi/12$ in fig. 5.1 as the EBFs shows a local minimum at $x \approx 0.5\,\text{mm}$ and $y \approx 0.4\,\text{mm}$. The new model is not able to resolve these structures, hence the equivalent spot in the MBFs is filled with higher values, leading to a higher integral value.
Never the less, the relative error of the phase-averaged integral body forces of new model in its baseline state is as low as 4 % in the x-direction and 10 % in the y-direction.

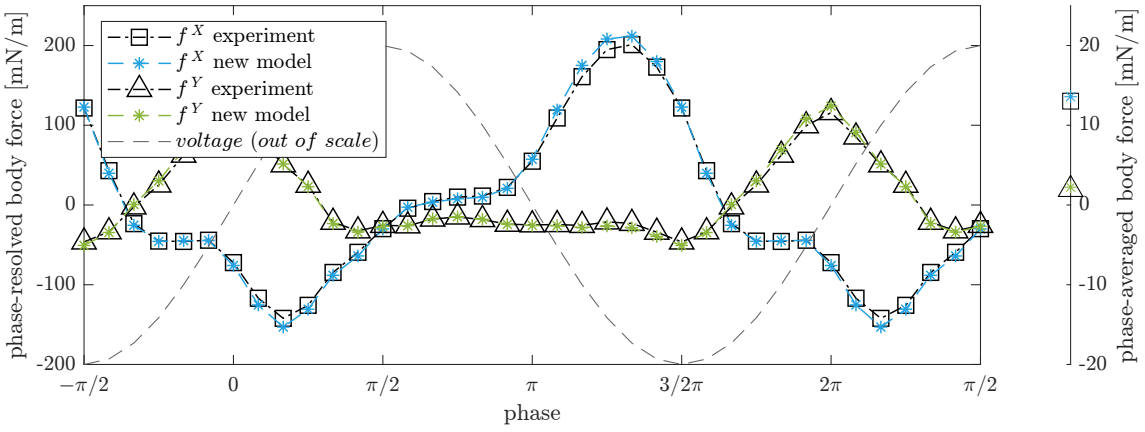

Figure 5.3.: Comparison of the integrated body forces. The left hand side describes the phase-resolved values, the right hand side shows their mean value. The dashed gray line refers to the voltage slope and is only drawn qualitatively. Experimental body forces according to Hehner *et al.* [12, 13].

Another performance evaluation of the new model is the attempt to compute the phase-averaged MBFs by averaging the PMs computed in 5.1.1. The result can be seen in fig. 5.4. A 3D-plot was chosen, as the resemblance of the experiment and MBFs can be displayed more intuitively (a 2D-plot of a comparable experiment can be found in fig. 2.18). The PMs show a reasonable course, with the exepteion of the two peaks on either end. The MBFs do not reach the maximum values displayed by the EBFs. This is counter intuitive, as fig. 5.3 shows a higher integrated and phase-averaged body force for the MBFs than for the EBFs. Phase-averaging each PM seems to cancel out the high values. The influence of the peaks on both ends of the PMs are clearly visible in the MBFs. Yet, the new model is able to approximate the topography of the EBFs. For instance, the skewness of the positive maximum to the right side is maintained in the MBFs.

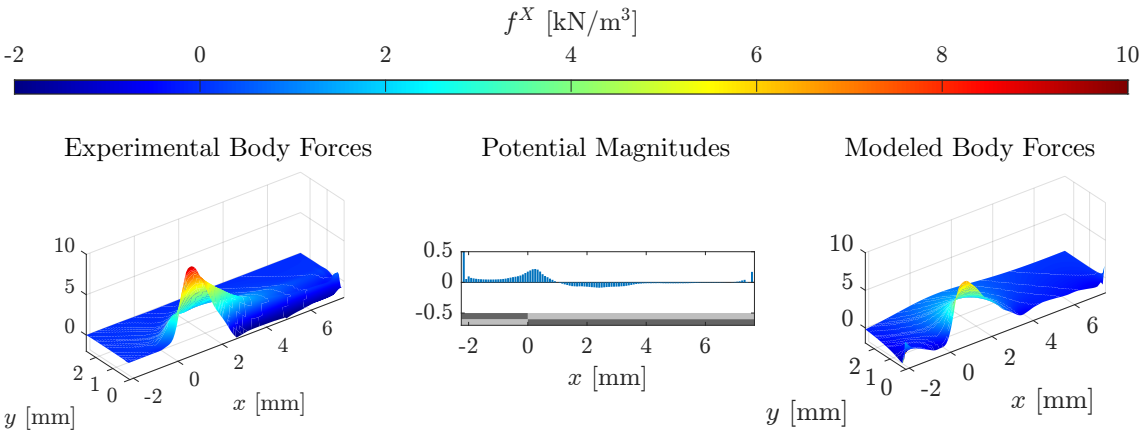

Figure 5.4.: The left column shows the phase-averaged EBFs in x-direction. The PMs in fig. 5.2 were phase-averaged to generate the displayed set and calculate the MBFs. EBFs according to Hehner *et al.* [12, 13].

The same calculation was made for the y-direction. Although neither the phase-resolved PMs nor the phase-averaged PMs show physical plausibility, the MBF topography resembles the EBFs. It can therefore be concluded that the topography of the phase-averaged new model can in fact be computed with the phase-resolved PMs. Yet, the correctness of the phase-averaged body force topography does not verify the course of the phase-resolved PMs themselves.
In contrast to the x-direction, the MBFs in y-direction rather exceed the maximum values. Furthermore, the new model is not able to resolve structures such as the ridge-like maximum at the actuator surface between $x \approx 2\,\text{mm}$ and $x \approx 4\,\text{mm}$.

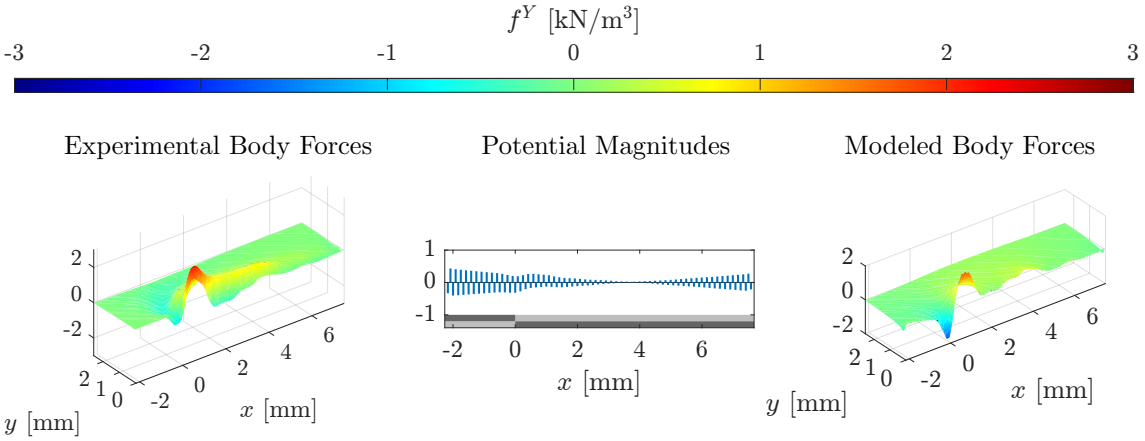

Figure 5.5.: The left column shows the phase-averaged EBFs in y-direction. The PMs in fig. 5.2 were phase-averaged to generate the displayed set and calculate the MBFs. EBFs according to Hehner *et al.* [12, 13].

Calculation of the Body Force Field in y-Direction with the PMs in x-Direction

The physical background of the model predicts the existence of a single set of PMs that is able to describe the EBFs in both directions with the components of the gradient. As the PM vector in y-direction lacks correctness, the MBFs were calculated with the PM vector in x-direction, but by multiplication with the derivation with respect to y. Here as aforementioned, the position of sign change along the actuator surface is resolved within the new model. An example of this can be seen for phase $0\pi/12$ at $x \approx 1.5\,\text{mm}$. The accuracy of resolving the right position of the sign change is good for phases of high

discharge and body forces as $0\pi/12$, $2\pi/12$. On the second half of the cycle, the region of negative body forces seems detached from the actuator surface ($12\pi/12$ and $14\pi/12$). To reiterate from beforehand, the new model is not able to accurately show minima or maxima that are not centered on the actuator surface.

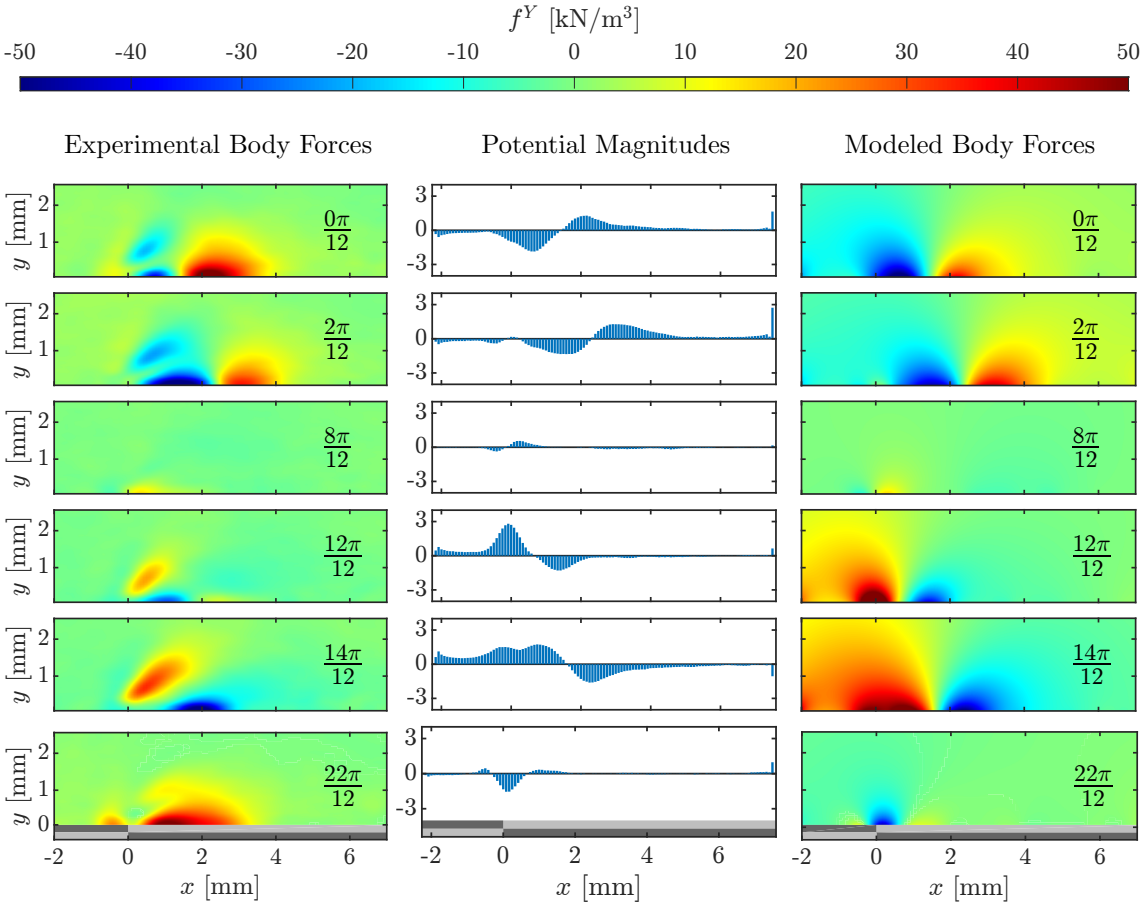

Figure 5.6.: Modeling results in y-direction, with the input of PMs in x-direction. EBFs according to Hehner *et al.* [12, 13].

5.1.2. Computation of One PM Vector for Both Directions

In addition to the previous section, the new model was also tested on its ability to compute a single sets of potentials that are able to describe both spatial directions. In order to do so, equation system 4.9 was extended as following, with the upper indices resembling the respective direction:

$$\begin{pmatrix} A^X_{M_1,x_1,y_1} & A^X_{M_2,x_1,y_1} & \cdots & A^X_{M_{max},x_1,y_1} \\ A^X_{M_1,x_2,y_1} & A^X_{M_2,x_2,y_1} & \cdots & A^X_{M_{max},x_2,y_1} \\ \vdots & \vdots & \ddots & \vdots \\ A^X_{M_1,x_{max},y_1} & A^X_{M_2,x_{max},y_1} & \cdots & A^X_{M_{max},x_{max},y_1} \\ A^X_{M_1,x_1,y_2} & A^X_{M_2,x1,y_2} & \cdots & A^X_{M_{max},x_1,y_2} \\ \vdots & \vdots & \ddots & \vdots \\ A^X_{M_1,x_{max},y_{max}} & A^X_{M_2,x_{max},y_{max}} & \cdots & A^X_{M_{max},x_{max},y_{max}} \\ \\ A^Y_{M_1,x_1,y_1} & A^Y_{M_2,x_1,y_1} & \cdots & A^Y_{M_{max},x_1,y_1} \\ A^Y_{M_1,x_2,y_1} & A^Y_{M_2,x_2,y_1} & \cdots & A^Y_{M_{max},x_2,y_1} \\ \vdots & \vdots & \ddots & \vdots \\ A^Y_{M_1,x_{max},y_1} & A^Y_{M_2,x_{max},y_1} & \cdots & A^Y_{M_{max},x_{max},y_1} \\ A^Y_{M_1,x_1,y_2} & A^Y_{M_2,x1,y_2} & \cdots & A^Y_{M_{max},x_1,y_2} \\ \vdots & \vdots & \ddots & \vdots \\ A^Y_{M_1,x_{max},y_{max}} & A^Y_{M_2,x_{max},y_{max}} & \cdots & A^Y_{M_{max},x_{max},y_{max}} \end{pmatrix} \begin{pmatrix} M_1 \\ M_2 \\ \vdots \\ M_{max} \end{pmatrix} = \begin{pmatrix} f^X_{x_1,y_1} \\ f^X_{x_2,y_1} \\ \vdots \\ f^X_{x_{max},y_1} \\ f^X_{x_1,y_2} \\ \vdots \\ f^X_{x_{max},y_{max}} \\ \\ f^Y_{x_1,y_1} \\ f^Y_{x_2,y_1} \\ \vdots \\ f^Y_{x_{max},y_1} \\ f^Y_{x_1,y_2} \\ \vdots \\ f^Y_{x_{max},y_{max}} \end{pmatrix} \tag{5.1}$$

The results can be seen in the following figures. The courses of the PMs in fig. 5.7a are similar to the baseline state. However, especially the PMs in the latter three phases are half as high as the corresponding PMs in the baseline state. An explanation is found by regarding the integral body forces in y-direction (fig. 5.7b) that exhibit lower values for these phases. This leads to a damping in the common PMs.
The computed EBFs in y-direction (fig. 5.7b) show satisfactory results, despite the maximum body forces not being reached. Never the less, the positions of the maxima, minima and zero crossings are resolved accurately.

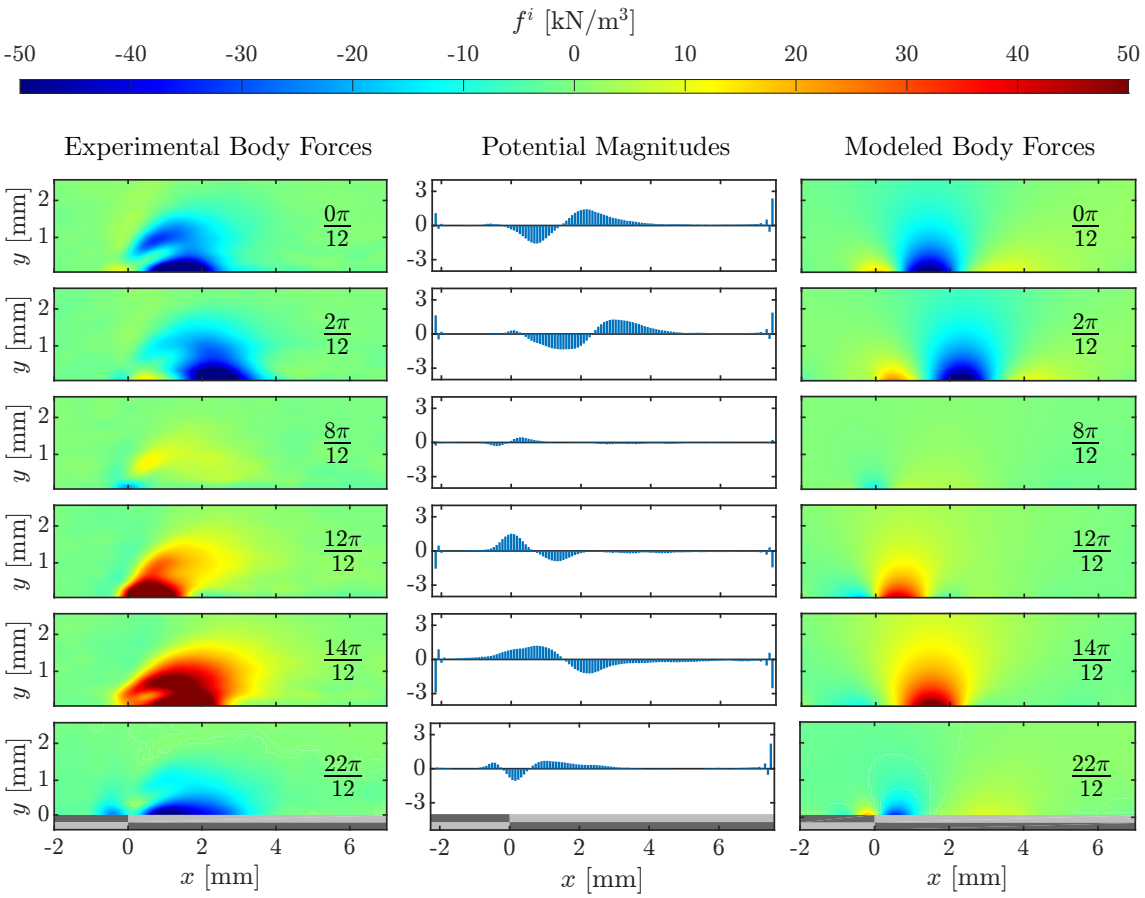

(a) X-direction

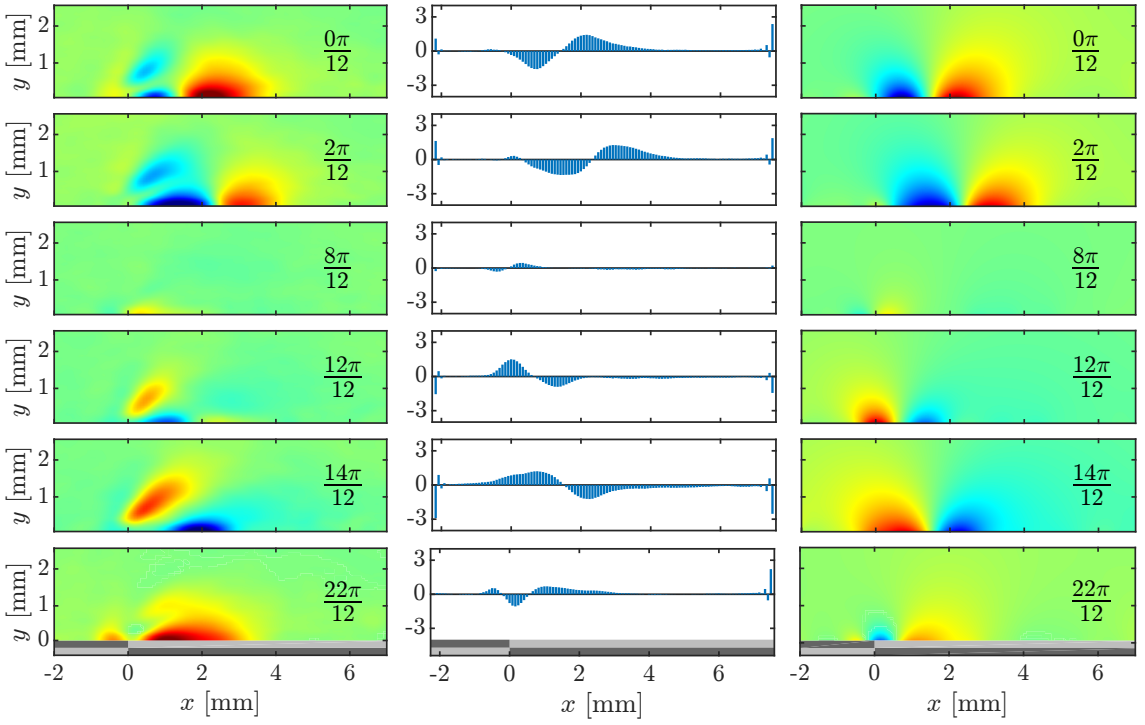

(b) Y-direction

Figure 5.7.: Modeling results in for a common set of PMs in both directions. EBFs according to Hehner *et al.* [12, 13].

Subsequently, the integrated body force values are compared in fig. 5.8. It is clearly visible that the shared PMs impair the performance of the MBFs in x-direction. Especially phases of high discharge and therefore high integrated body forces are only modeled with half of their experimental value. The results in y-direction on the other hand, show good accordance to the experimental data. This can be ascribed to the generally lower body force values that damp the common PM values, but are less affected themselves.

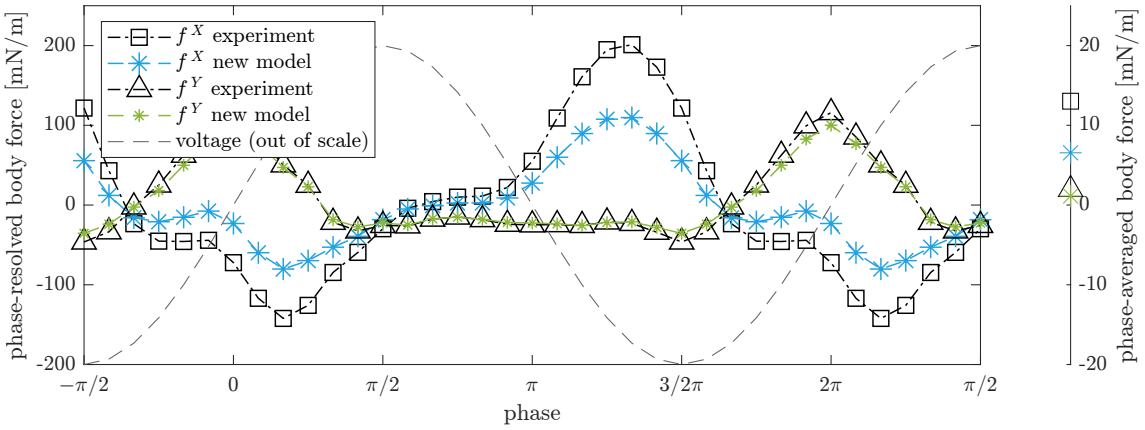

Figure 5.8.: Comparison of the integrated body forces for a common set of PMs. The left hand side describes the phase-resolved values, the right hand side shows their mean value. The dashed gray line refers to the voltage slope and is only drawn qualitatively. EBFs according to Hehner *et al.* [12, 13].

Summarizing, it can be said that a modeling process as presented by the equation system 5.1 is desired, as it is in accordance to the physical background of the new model. Particularly, the course of the phase-resolved, integrated body forces in fig. 5.8 and the plausibility of the PMs themselves indicate the validity of a common set of PMs. Yet, the absolute values of the integral body forces do not meet the requirements.

5.1.3. Comparison of Different Potential Formulations

As described before, different potential formulations are examined. The detailed figures can be found in the appendix: C to D. The comparison of integral body forces in fig. 5.9 and fig. 5.10 show the clear dominance of the chosen logarithmic approach as it models both components of the integrated body force best, especially for phases with high values.

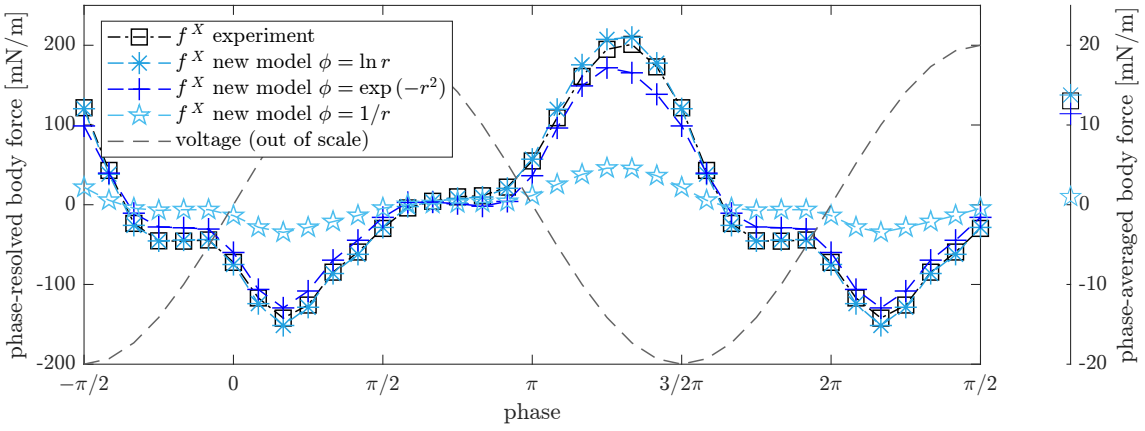

Figure 5.9.: Integral body force in x-direction for different formulations of the potential decay. EBFs according to Hehner *et al.* [12, 13].

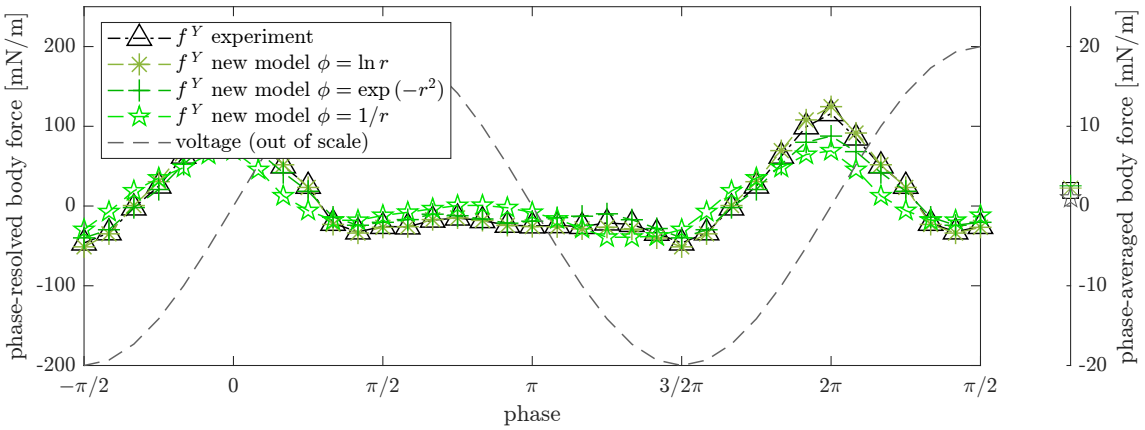

Figure 5.10.: Integral body force in y-direction for different formulations of the potential decay. EBFs according to Hehner *et al.* [12, 13].

The broken rational potential description does not resolve the integral body forces for high discharge, nor does it for low discharge phases. Yet, here, information that confirms a previous explanation can be found in the PMs in D: The first and last five values of the PMs are set zero. In conclusion, the numerical process is theoretically able to null the PMs on the outer bounds and additionally, the peaks of the outer baseline state PMs in fact relate to the flaps of the derivation.
Nevertheless, the MBFs of the broken rational potential description show clear overshoots in regions that are neutral in the EBFs (eg. C, phase $1\pi/12$), leading to a lower integral body force. The PMs and MBFs in y-direction show less peaks in the broken rational formulation than in the baseline state, and their integral values perform better in y- than in x-direction, but their integral values lag behind.

A physical explanation for the better performance of the logarithm-based approach is found in fluid dynamics, as well as electrodynamics. In both scientific fields the logarithmic formulation describes two-dimensional problems with constant potential values in z-direction as displayed in fig. 5.11b. The broken rational formulation on the other hand describes a single point potential in thee dimensions (5.11a). The extension of the electrodes in z-direction (coordinate system as in fig. 3.1) is large compared to the width in x-direction. Thus, the electric field is uniform in z-direction and reasons the logarithmic potential formulation.

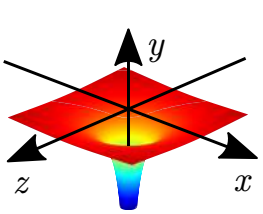

(a) A single point potential described by $\phi = {}^{-1}/\sqrt{x^2+y^2+z^2}$.

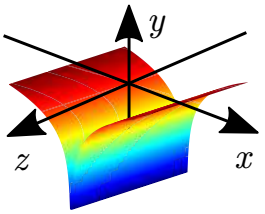

(b) A line potential described by $\phi = \ln\sqrt{x^2+y^2}$. The extension is independent from the z-direction.

Figure 5.11.: Spatial description of a single point and a line potential. In accordance to the coordinate system in the experimental setup (fig. 3.1), the z-coordinate refers to the length of the electrodes. The discharge is uniform in this direction and therefore irrelevant for the experimental measurements.

The integrated body force values of the exponential potential formulation nearly reach the experimental data in x-direction. Nevertheless, the PMs in x-direction consist of non-physical peaks. These peaks can be softened through numerical tricks in the $LSMR$-code, as it has the option to extend equation 4.10 with a "damping factor" λ according to 5.2. Yet this damping causes lower integral body forces and is therefore not a promising practice.

$$\|A^i\vec{M}^i - \vec{f}^i\|^2 + \lambda^2\|\vec{M}^i\|^2 \tag{5.2}$$

In y-direction a clear lack of accuracy is shown for nearly all phases. The reason for this behavior can be seen in the MBFs in fig. D.19. The derivation with respect to y of potentials positioned on the actuator surface show their influence for values of $y \approx 0.8\,\text{mm}$ due to the nature of the Gaussian distribution. This proves the non-physical performance of this approach. Still, the exponential formulation contributed highly to the development of the numerical setup as it does not have a singular point. Therefore, it was used to debug the model.

5.1.4. Extension of the Numerical Grid

The next evaluated configuration of the numerical model addresses the non-physical peaks of the outer PMs in the baseline state. In accordance to the previous chapter, these peaks originate from the derivation of the logarithm in x-direction of the outermost potentials , which in turn results in flaps. These outer potentials still influence the body forces inside the CV. In order to provide incentives for the least-square algorithm to lower the values of the outer potential magnitudes, the experimental body force field was extended by 20 grid cells up- and downstream. These additional grid cells were assigned to contain body forces of the value zero.

A complete list of the respective solutions is found in the appendix (E). For simpler visualization, the PMs are shown in their fully extended length whereas the MBFs are shortened to the experimental CV. As the extension does not significantly affect the integrated body force values, the evaluation of this model configuration concentrates on the plausibility of the PMs.

In fig. 5.12, the PMs for the first phase $0\pi/12$ in x-direction without extension as well as those extended by 20 grid cells, are singled out. The positive effect of the extended field quarters the upstream peak of the PMs and generally lowers the PMs close by, while not affecting the maximum values in the discharge area. On the downstream side this improvement does not eventuate. The extension of the numerical grid improves the plausibility of the solution, though the peaks could not be lowered by further extensions.

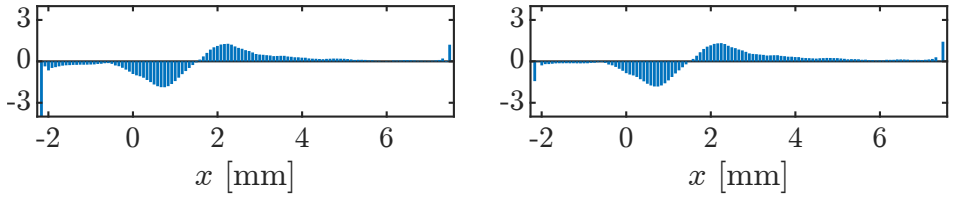

(a) Baseline without extension (b) Extension with 20 grid cells

Figure 5.12.: X-direction: Comparison of the PMs in baseline state and for a numerical grid, extended by 20 grid cells for phase $0\pi/12$

The influence of the extension in y-direction is best visible in the comparison of the phases with the highest amplitude of PM peaks: $2\pi/12$ (5.13). Here, the baseline state leads to

a magnitude amplitude of up to 20. This value is decreased dramatically, by an entire order of magnitude, by extending the numerical grid. Just as in x-direction, an extension of more than 20 grid cells did not enhance the solution further.

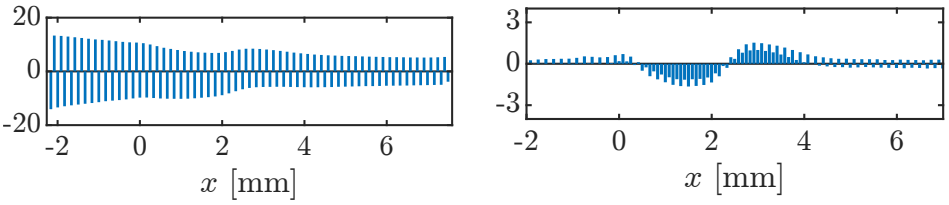

(a) Baseline without extension (b) Extension with 20 grid cells

Figure 5.13.: Y-direction: Comparison of the PMs in baseline state and for a numerical grid, extended by 20 grid cells for phase $2\pi/12$

5.1.5. Extension of the Numerical Grid and Additional Potentials

For further reduction of the outer split peaks, body force potentials were placed outside of the experimental CV. The expectation is that these potentials are able to smooth the peaks on the borders of the CV. They are influenced less by the body forces inside the CV and decreased by the extended grid cells that contain the value 0. Therefore the numerical grid of the baseline state is extended by 40 grid cells as shown before and 20 additional potentials were placed up- and downstream of the numerical grid. These values were chosen in accordance to the results of the last section. The logarithmic potential formulation is sensitive for changes of the numeric grid up to 20 cells, thus the influence of 20 additional potentials on either side was investigated, with a numerical grid extended by 40 cells. Likewise, the full set of figures is included in the appendix (F), but the essence of the impact of additional potentials can be visualized by considering certain PMs.

The left-hand side of figure 5.14 shows the PMs for a numerical grid extended by 40 cells up- and downstream and is similar to the result of the previous section. The right hand side shows the same numerical grid as the left one, but with additional 20 potentials in each horizontal direction. Note that due to the additional potentials, the abscissa in the following figures reaches further than in previous sections.
A first examination draws attention to the original boundaries of the numerical grid at $x = -2.1\,\text{mm}$ and $x = 7.5\,\text{mm}$. The, by now well-known, peaks are visible in fig. 5.14a and still exist in the PMs in fig. 5.14b, yet their height is extremely reduced. All the same, the influence of the flaps is only shifted to the new boundaries, despite these accrued peaks being slightly lower than the original ones.

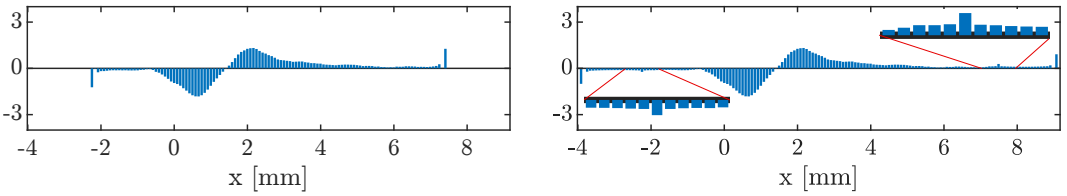

(a) Extension of the numerical grid by 40 cells on each side. (b) Extension of the grid by 40 cells and 20 additional potentials on each side.

Figure 5.14.: X-direction: Impact of the extension of the numerical grid with 40 grid cells and 20 additional potentials up- and downstream for phase $0\pi/12$

In continuing in the improvement of the PMs in y-direction for phase $2\pi/12$, fig. 5.15 compares the sole extension of the numerical field on the left side with the positioning of

additional potentials on the right side. While the overall peaks are further diminished, the only additional impact on the upstream half of the PMs are the small values for $x < -2.1\,\text{mm}$. On the contrary, the peaks in the downstream half show values very close to zero, between $x = 4.5\,\text{mm}$ and $x = 7\,\text{mm}$, but start alternating again for higher x-values.

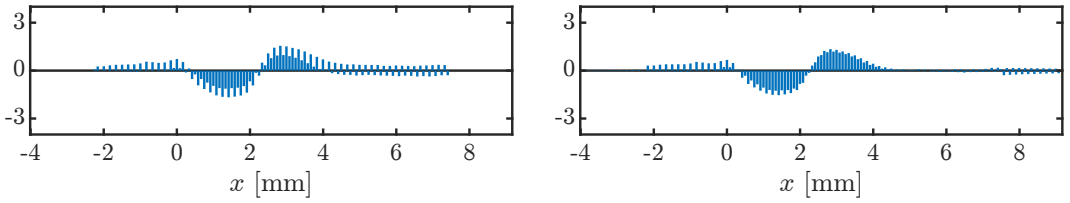

(a) Extension of the numerical grid by 40 cells on each side.

(b) Extension of the grid by 40 cells and 20 additional potentials on each side.

Figure 5.15.: Y-direction: Impact of the extension of the numerical grid with 40 grid cells and 20 additional potentials up- and downstream for phase $2\pi/12$.

Concluding, the extension of the numerical grid and additional potentials enhance the plausibility of the PMs and thus should be considered in future modeling activities. Even so, it should be said that the PMs that are computed with the extended grid should not simply be multiplied with the original, non-extended matrix A^i. This would lead to an unbalanced influence of the flaps and therefore to unsatisfactory results.

5.1.6. Influence of the Distance of Potentials

As described in chapter 4.2, an increased distance is expected to compute insufficient results due to interference effects (shown in fig. 4.4b). A future workaround not examined in this thesis could be an approach that does not simply overlay two single potentials, but instead builds upon broader potentials, as sketched in fig. 5.16. Early new model formulations on the basis of the exponential approach (that does not involve singular points) showed promising results for ten single potentials in the numerical grid. This means, a potential formulation similar to the one displayed on the right hand side could lead towards a simplified model that is numerically more efficient and stable. Nevertheless, the Nyquist Theorem should be kept in mind: Horizontally, the closest distance between two body force maxima are found at $11\pi/12$ for the y-direction with a distance of roughly 1 mm. This refers to about 12 grid cells. Hence, to avoid alialising effects, the distance between two potentials should not exceed 6 grid cells or around 0.5 mm.

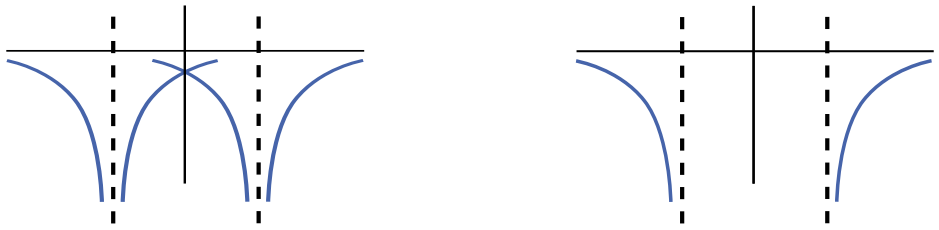

(a) Superposition of potentials as applied in this thesis. Prone to interference effects if the distance between the potentials is to large.

(b) Suggested new concept. The numerical behavior close in the singular area has to be examined.

Figure 5.16.: Sketch of suggestion for an alternative formulation of super positioned potentials. The new concept on the right is promising not to create undesired interference effects.

The importance of further examinations regarding an optimized distance between the single potentials becomes apparent in the results shown next. As expounded before, a simple increase in the distance between potentials in the current formulation does not make sense. Instead the distance was decreased in relation to the experimental grid distance $\Delta x = 8.3 \times 10^{-2}$ mm. For distances below $0.9 \cdot \Delta x$, the PMs in both directions solely consist of spikes and are therefore not physically plausible.

Interesting effects can be found for distance close to the original grid cell size, for example for $0.9999 \cdot \Delta x$. Here, the PMs in x-direction show a spiky behavior very similar to the PMs of the baseline solution in y-direction. Yet, with the new distance, the PMs in y-direction form a plausible course disregarding the normal peaks of the outer values. This confirms the former assumption that numerical flaws cause the implausible spiky behavior of the respective PMs.

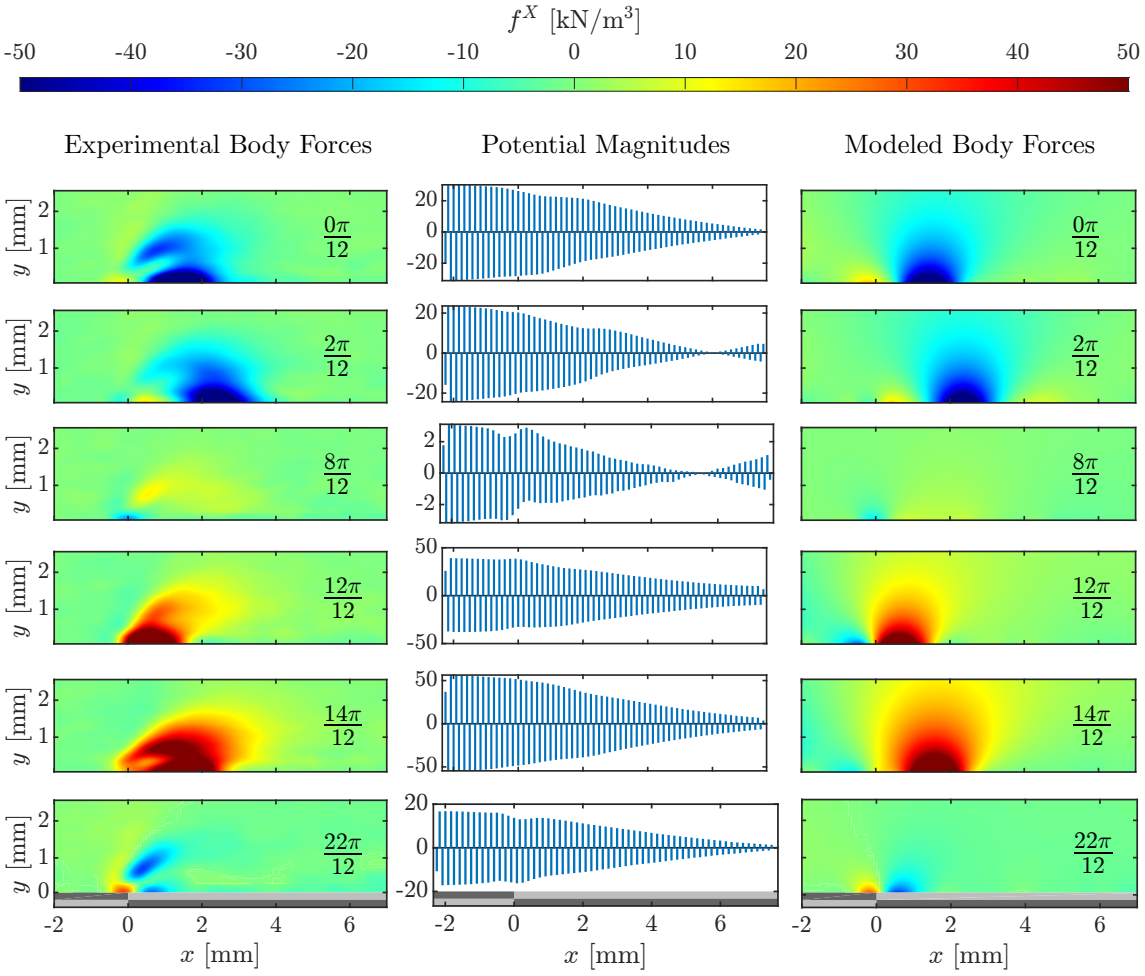

Figure 5.17.: Comparison of EBFs, computed PMs and the resulting MBFs in x-direction for a potential distance of $0.9999 \cdot \Delta x$. Note that the ordinate limits for the PMs vary due to the described numerical flaws. EBFs according to Hehner *et al.* [12, 13].

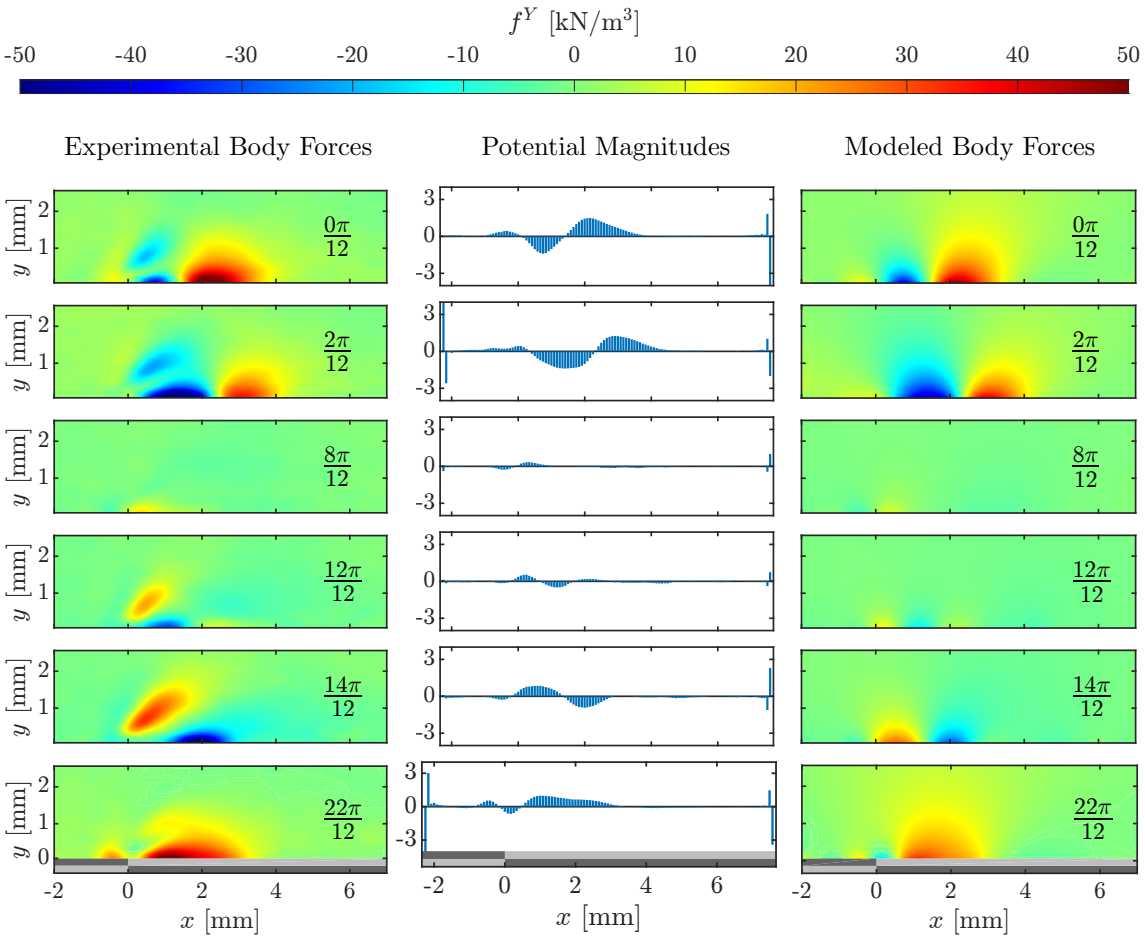

Figure 5.18.: Comparison of EBFs, computed PMs and the resulting MBFs in y-direction for a potential distance of $0.9999 \cdot \Delta x$. EBFs according to Hehner *et al.* [12, 13].

5.1.7. Additional Potential Rows Above the Actuator Surface

The state examined next gives unprecedented insights into the determination of the maximum vertical distance from the actuator, where free charges induce body forces. Therefore, potentials are not only placed on a string on the actuator surface, but are also located equidistantly up to certain grid cells. Just as before, the singular points were set between the computational knots of the numerical grid.

First, the results of placing 10 rows of potentials, up to a height of $y \approx 0.65\,\text{mm}$, are displayed in fig. 5.19 and fig. 5.20. In comparison to former figures, the abscissa of the PMs in these figures does not directly represent the horizontal position in the numeric grid, but refers to the respective row.

On first sight the lack of plausibility in the PMs of both fig. 5.19 and fig. 5.20 is obvious. Even though the course of the PMs in x-direction could be compared to the courses seen before, the magnitudes of the first two rows of potentials are several orders of magnitude above former results. Despite the magnitudes decreasing for higher row numbers, it is not until the eighth row that the PMs are comparable to previous results.
In the MBFs in x-direction the highest row is clearly visible with a horizontal cut in the continuous topography of the field. Never the less, local maxima are resolved accurately even slightly outside the area of positioned potentials.

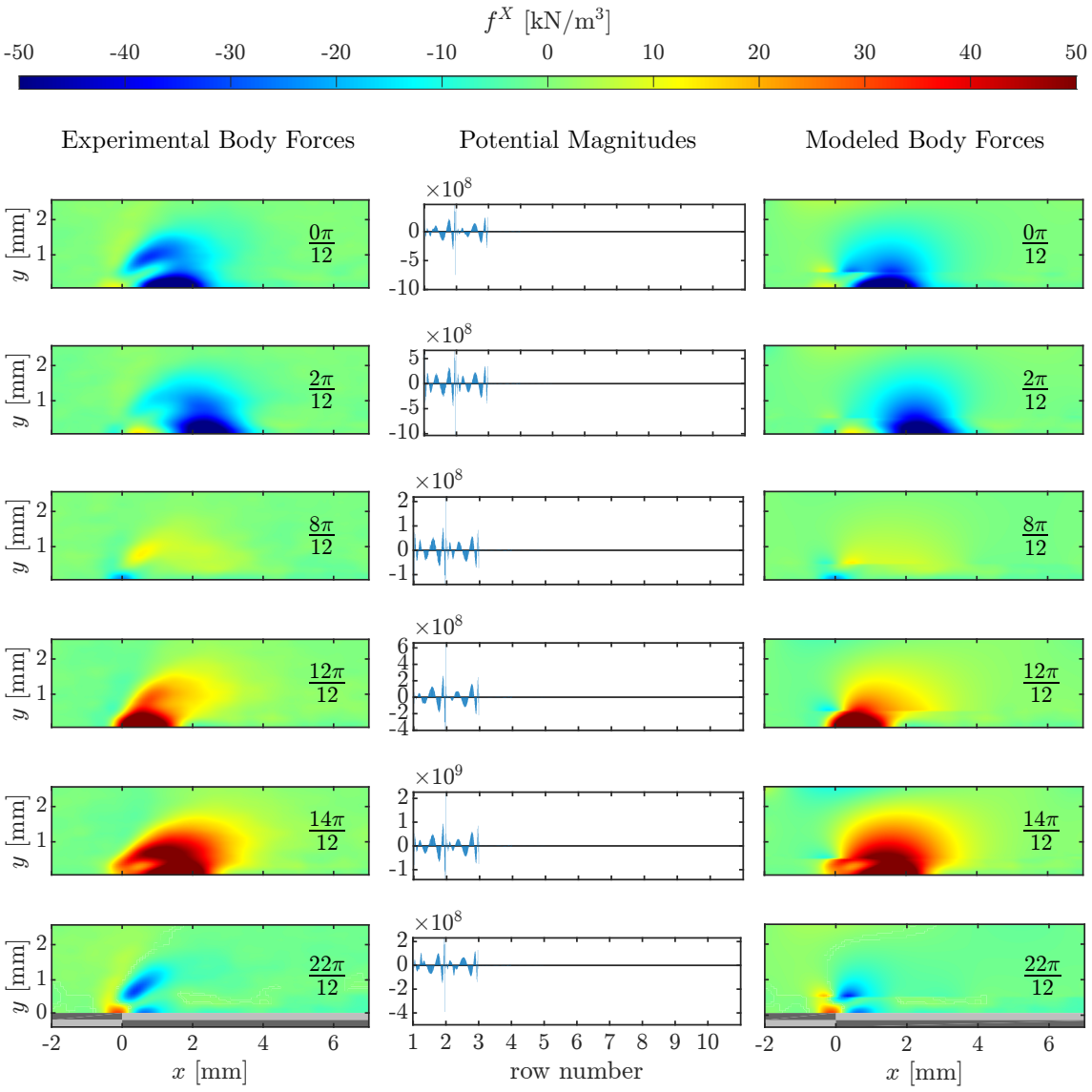

Figure 5.19.: Modeling results in x-direction for 10 vertical rows of potentials above the actuator surface. Note that the abscissa of the PMs refers to the respective row number and the limits of the ordinate are not uniform. EBFs according to Hehner *et al.* [12, 13].

The PMs in y-direction in fig. 5.20 do not exceed the orders of magnitude like the PMs in x-direction They are more comparable to the baseline state, as each row of PMs is of a triangular shape which results from the spiky behavior seen before. Furthermore, the rows alter between two orders of magnitude, meaning a row of high magnitude is followed by a row of lesser magnitude and so on.
The MBFs are similar to the results in x-direction: The position of the last row of potentials is visible and local maxima that are located further away from the actuator can be resolved. A complete figure list of the model with ten potential rows is found in the appendix (H). It is clearly visible that an increasing number of rows improves the new model topography, while the PMs still lack plausibility. A further point to considerate is that by positioning potentials solely at $y = 0$, the symmetry of the potentials inhibits body force to act through the actuator surface and therefore meet the experimental data. With the positioning of potentials further above, this advantage is gone. An approach for future investigations could be the implementation of a stream function as done in fluid dynamics. This stream

function could mimic the actuator surface.

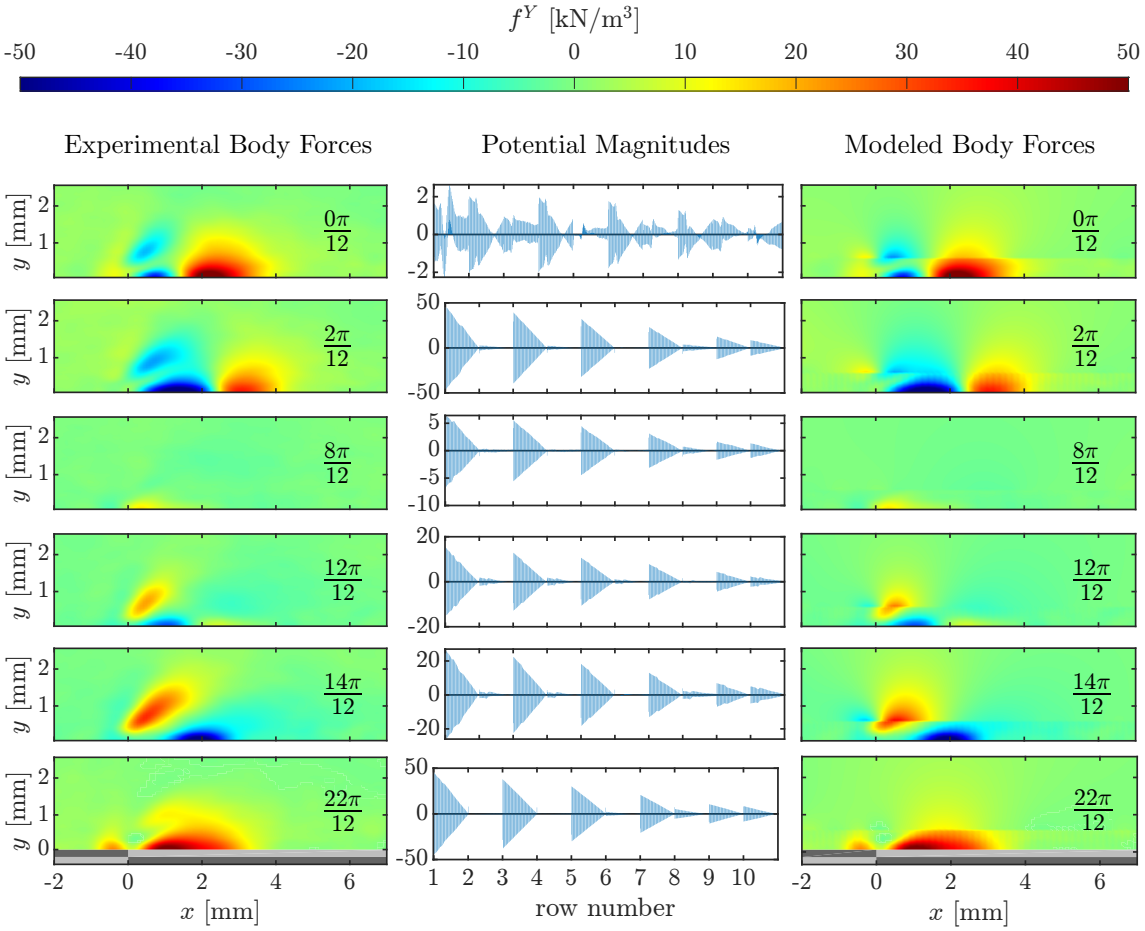

Figure 5.20.: Modeling results in y-direction for 10 vertical rows of potentials above the actuator surface. Note that the abscissa of the PMs refers to the respective row number and the limits of the ordinate are not uniform. EBFs according to Hehner *et al.* [12, 13].

While the configuration above improves the MBF topography, it is at the expense of the computational run time. Every additional potential enlarges the system of equations by one line, thus, the additions above greatly increase the complexity of the fitting process. As a consequence, the constituted configuration could be considered in future investigations, if combined with a general decrease of the number of potentials as described in the last section.
In the end, this configuration was included in the thesis to prove the ability of the new model to resolve the EBFs accurately. The positioned body force potentials are expected to associate with free charges above the actuator. Therefore, it seems logical to locate potentials only as high es they are expected in the discharge. It should be kept in mind that one huge advantage of the new model is the reduction of the complexity of modeling two components of body forces towards a single set of potentials. This advantage shrinks as the number of potential rows increases.

5.2. Discussion of Results

The results presented in the previous section will be contextualized here. The baseline state offers the best possibility for interpreting the PMs in x-direction in the context of the

phase-resolved charge distribution and also gives an understanding for future approaches of PM interpretations.

5.2.1. Discussion and Interpretation of the Baseline State

The figures 5.21 and 5.22 display the PM course for all phases. Note that, contrary to presentations in previous chapters, the phases now start from the respective maximum voltage, as practiced by other authors (Enloe[7], Kriegseis[16]). This order allows the observation of discharge formation from the collapsed state, which is observed around the maximum voltage. Still, the phases are named as before and one figure line comprises two PM courses. They are phase-shifted by π for a direct comparison with the opposite phase. Additionally, the figures show the respective course of potential magnitudes (blue/purple line) and their derivation in x-direction (pink line) in spatial relation to the newly computed body forces in x-direction. This compilation visualizes the link between the potential magnitudes and the new model. Especially for phases of high discharge, it is obvious how the derivation of the potential magnitudes refers directly to the topography of the new model.

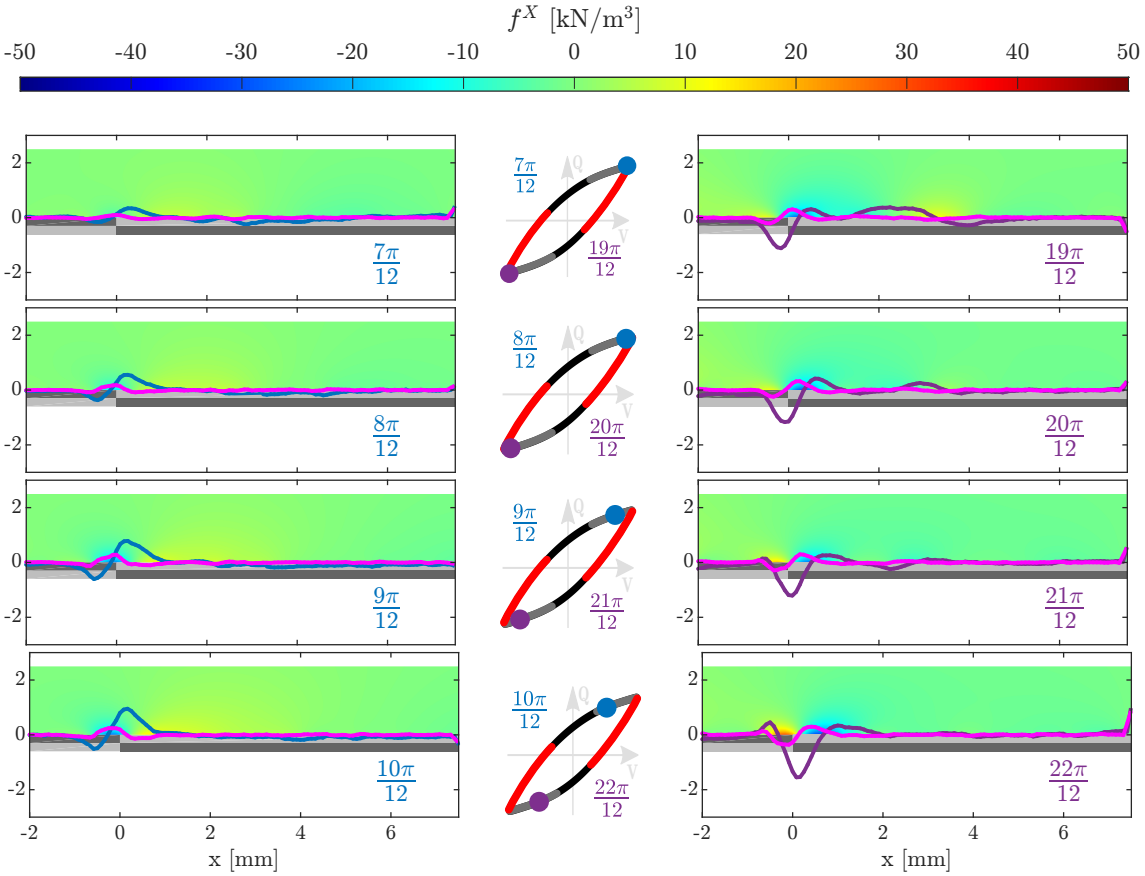

Figure 5.21.: First part: Summary of all PMs in x-direction for the baseline state. The Lissajous figure is based on Hehner *et al.* [12, 13]. The red line marks phases of high discharge and hence large body forces. The gray line marks phases with collapsed discharge. The PMs on either side of the Lissajous refer to the phase marked in the same color. The ordinate is displayed without value, as it specifies the y-coordinate in [mm] for the surface plot and the potential magnitude for the line plots (displayed without units). EBFs according to Hehner *et al.* [12, 13].

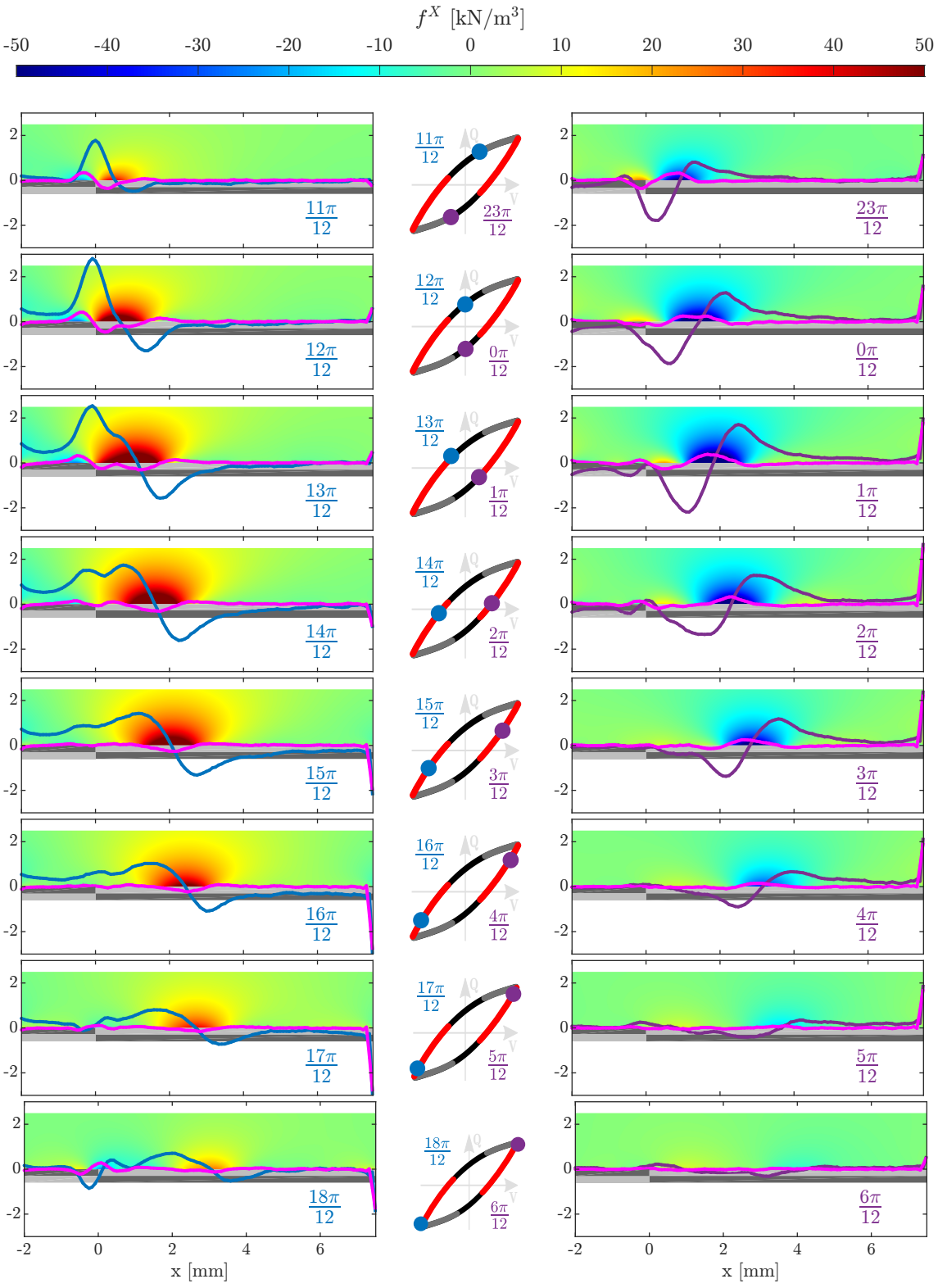

Figure 5.22.: Second part: Summary of all PMs in x-direction for the baseline state. The Lissajous figure is based on Hehner *et al.* [12, 13]. The red line marks phases of high discharge and hence large body forces. The gray line marks phases with collapsed discharge. The PMs on either side of the Lissajous refer to the phase marked in the same color. The ordinate is displayed without value, as it specifies the y-coordinate in [mm] for the surface plot and the potential magnitude for the line plots (displayed without units). EBFs according to Hehner *et al.* [12, 13].

At this time, the computation of the new model out of the potential magnitudes is described with the example of phase $12\pi/12$ and $0\pi/12$ (last line in fig. 5.21). The zero crossing of the MBFs results from local maxima in the PMs. It is clearly visible how the location of the zero crossing of PMs correlates with the local maxima of the MBFs for phases with high discharge. This fact is not as intuitive as it seems on first sight. A high modeled body force stems from a high gradient of PMs and not necessarily from a zero crossing. Yet the computation of the PMs yields a zero-crossing at this point. This is of interest considering the location of the zero-crossing in the experimental body forces in y-direction, as displayed in fig. 5.23 for the same chosen phases as evaluated in the previous section. Especially for the first three phases, the zero crossing in the PMs in x-direction coincides with the zero crossing in the experimental body forces close to the actuator in y-direction. The body force minima in the latter three phases are located above the actuator surface and seem to have a slight downstream drift. In accordance to previous evaluations, the new model in its current state is not able to resolve these topographies.

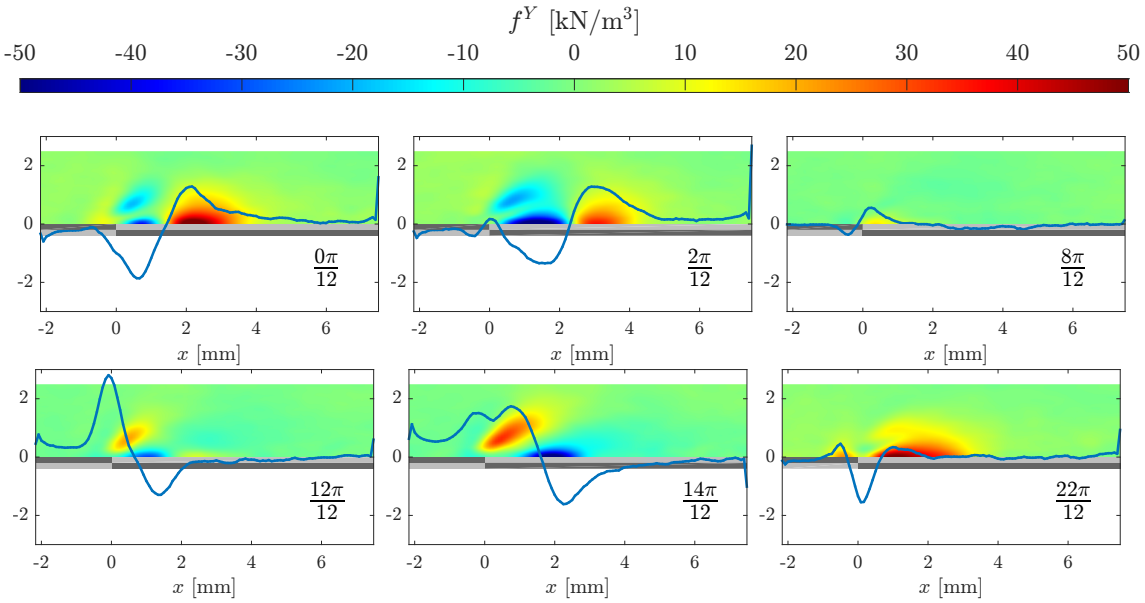

Figure 5.23.: Compilation of experimental body forces in y-direction (surface plot) and potential magnitudes for the x-direction (blue line). Note that the ordinate is displayed without units. It represents the y-coordinate in [mm] for the surface plot and the potential magnitudes for the line plot. EBFs according to Hehner *et al.* [12, 13].

Up until now, no direct physical link between potential magnitudes and charge densities as suggested in 2.3.2 could be found. Still, the course of the PMs for different phases can be compared to the expected charge densities causing capacitance changes as described in 2.4.

Following this theory, one can interpret the course of the PMs for the different phases. The principle is explained regarding the forward stroke (as suggested by [7]), displayed in the left column of fig. 5.21 and fig. 5.22. The suggested effect begins in phase $12\pi/12$, briefly before the voltage sign change. Hereinafter, outer PMs resulting from flaps will be neglected.

The main zero crossing of PMs is located at $x \approx 0.7\,\text{mm}$, between the upstream global maximum (magnitude ~ 2.8) and the downstream global minimum (magnitude ~ -1.3). For proceeding phases, the zero crossing of PMs moves downstream, accompanying the location of the body force maximum. While doing so, the sequence of a maximum, followed by a zero crossing and then a minimum in the PMs is maintained. Yet the maximum has

the highest value at the phase $12\pi/12$ and widens and decreases for the following ones. The last PM set of a comparable sequence is computed for $17\pi/12$ with a zero crossing at $x \approx 2.9\,\mathrm{mm}$.
At this point the sign of the potentials can be related to the respectively applied voltage. For all phases described in the last paragraph, the potential magnitudes at and adjacent to the exposed electrode are positive, while the voltage is negative. Hence, in compliance with the nature of the logarithmic potential formulation, a positive potential magnitude relates to negative charges.
This accordance leads to the conclusion that the course of the PMs indicates the spatial distribution of free charges. Subsequently, the afore-mentioned phase-resolved course of PMs will be compared to the capacitance changes as in 2.4. According to Kriegseis [16] in figure 2.9, the actuator has the cold capacitance C_0 slightly after every positive and negative voltage maximum. This would mean that no charges are in the electric field, yet the measurements reveal non-zero body force and hence the new model computes low potential magnitudes. Yet, these body forces can be traced back to measurement errors in the PIV and hence associated phases are considered to be significant. The zero crossing of the PMs moves downstream with the phase progression, as described before, corresponding to a virtual prolonging of the exposed electrode and hence an increased capacitance. The phase with the clearest and longest virtual electrode is $16\pi/12$ and is approximately in accordance to the measurements. Afterwards, the virtual electrode collapses and also the interpretation of the PM courses becomes vague.

All of the interpretations above can also be applied to the forward stroke. Yet, due to the different masses of the involved charges, the course of the PMs, the maximum values and the position of the zero-crossing will differ from the backward stroke.

5.2.2. Approaches for a Relation Between Potential Body Force Magnitudes and Electric Charges

So far, the new model is only able to describe effects that are already contained in the experimental body forces. Yet the approach could lead towards a more profound understanding of the phase-resolved charge distribution of the actuator. Therefore a direct link between the computed potential magnitudes and the net charge of the associated numerical grid cell has to be found.

Following, a few approaches will be described to facilitate further considerations. Building on the basic electrohydrodynamic relation as shown in section 2.3.2, takes up the idea of the direct link between fluid mechanic body forces and the electric field:

$$\vec{f} = q_\mathrm{c}\vec{E} \tag{5.3}$$

The latter part of the equation describes the influence of the electric field (a superposition of all charges) on a single charge. The new model builds upon the idea to describe the influence of the body force field (a superposition of all body force potentials) on a single potential. Therefore the upper equation can be transformed into a parallel definition of body force potentials ϕ_f and electric potentials ϕ_e:

$$PM(x)\ \nabla\phi_\mathrm{f} = -q_\mathrm{c}(x)\ \nabla\phi_\mathrm{e} \tag{5.4}$$

As before, the electric field is simplified as a single line charge at the actuator surface and observe a discrete grid. Inserting the definition of the body force and electric potential

(with the permittivity of vacuum ϵ_0) leads towards a relation between the PM or charge density at a certain point k to the respective sum of all PMs or charges.

$$PM_k \nabla \sum_{i=1}^{max} PM_i \ln(r_i - r_k) = -q_{c,k} \nabla \sum_{i=1}^{max} \frac{q_{c,i}}{2\pi\epsilon_0} \ln(r_i - r_k) \tag{5.5}$$

This equation could pave the way to a coefficient α that directly links the PM to the local charge density:

$$PM = \alpha \cdot q_c \tag{5.6}$$

If future investigations do not reveal an algebraic solution to the relation above, a different approach for the determination of α could start from a calibration of the PMs.
A first idea did not suceed: The nearly constant positive PMs at the exposed electrode ($-1.8\,\text{mm} < x < 0.8\,\text{mm}$) for phases $12\pi/12$ to $16\pi/12$ in fig. 5.21 and fig. 5.22 could refer to the charge of the electrode. This would mean that the corresponding PMs in the backwards stroke should show constant negative values. This is not the case.
Further concepts could involve the separation of potential as suggested by Suzen *et al.* [32, 31] into the influence of electrodes and free charges. As the relation between the voltage and potential of the electrodes is understood at that point, the PMs could be separated in the same manner to investigate the distribution of free charges.

5.2.3. Applicability of the New Model for Free Stream Velocities

An important step for a body force model of a DBD actuator is its integrability to numerical simulations of real-life applications. Most examples of these applications, with an airfoil being the most prominent one, involve free stream flow fields.
Hehner *et al.* ([12, 13]) run PIV measurements, equivalent to those in chapter 3.1, with free stream velocities ranging from 5 m/s to 30 m/s. As described before, Hehner applied the Navier-Stokes-equations to compute the body force field. The resulting body forces can be seen in fig. 5.24. It is obvious how the free stream has only slight influence on the topography of the body forces.

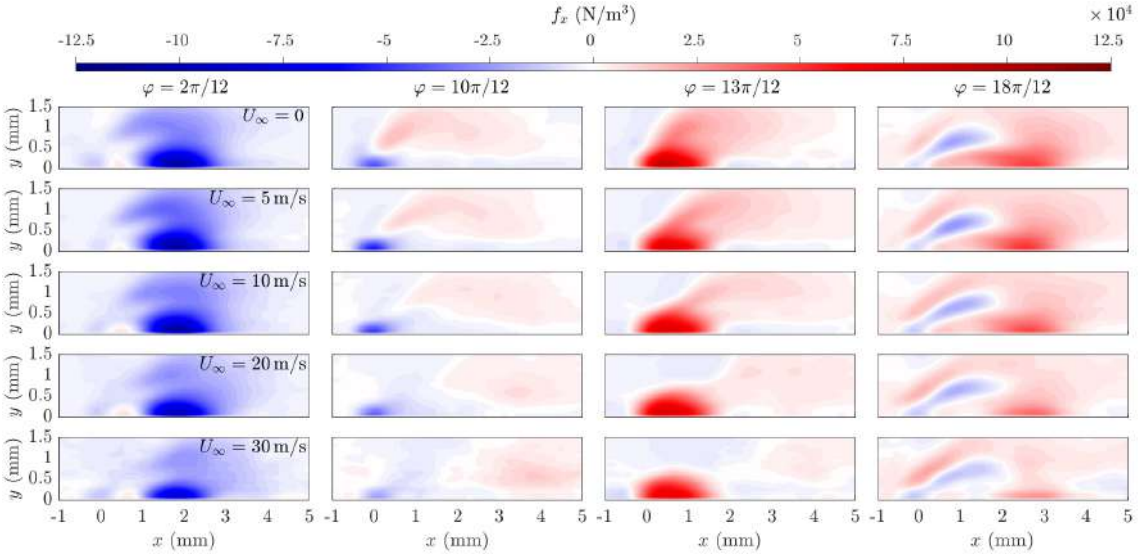

Figure 5.24.: The body forces in x-direction derived from PIV measurements with different free stream velocities by Hehner *et al.* [12, 13].

Until now, the new model is based on the positioning of potentials that originate from electric charges. A free stream, on the other hand, is solely of fluid dynamical nature.
Both electrostatics and fluid dynamics describe similar fields, known as uniform electric field (e.g. found in a parallel-plate capacitor) and parallel flow field. The underlying potential for a parallel flow field in x-direction has the following form :

$$\phi = U_\infty x \tag{5.7}$$

An extended model which is able to compute the effects of a free stream, could be build up on the same equation system as the current model (4.9), but with the superposition of the free stream potential that is included in the equation system as an additional row.
Yet, fig. 5.24 shows the low influence of the free stream on the body forces, while a formulation as in eq. 5.7 resolves in constant body forces in x-direction. A better, but not physically correct approach could be the application of the new model in its basic state to the experimental body forces measured with a free stream. This could reveal an influence that can not be estimated yet, such as a constant offset in the PMs.

5.3. Comparison to Existing Models

The idea of the derivation of the body forces from the electric quantities was already applied by Shyy *et al.* and Suzen *et al.* as shown in 2.5. In contrast to these two approaches, the new empirical model builds upon the same physical framework, yet does not give a detailed input of the charge distribution. It rather suggests possible positions, as the line of potentials, but lets the model dictate the magnitude of each potential. The clear advantage of this proceeding is that the new model does not make estimations about the resulting potential magnitudes. The only constraint that was made is the general potential position. In comparison with the model by Maden, it can not compete with the accuracy of the phase-averaged body force topography. Yet the model by Maden is only able to beat the new one in this aspect, whereas the new one offers a basis for a variety of numerical configurations.
Table 2.2 summarized the characteristics of the described modeling approaches. The new model did already prove its proficiency regarding the integrated body forces, especially in a phase-resolved consideration. The velocity profile will be part of future numerical studies and can therefore not be evaluated in this thesis. The remaining aspects ”body force topography”, ”physical correctness” and a straightforward calculation of ”both directions” show promising results as described above. On a further note, the influence of the boundary layer should be taken into consideration, as potential theory is not able to describe viscous effects in flows. It is estimated that further investigations will improve the model in order to meet all requirements adequately.

6. Conclusions

In this thesis a new approach for an empirical model of the body forces induced by a DBD plasma actuator has been established and different parameter configurations have been evaluated with respect to their numerical impact.

Initially, the physical background of DBD actuation and the application of potential theory in fluid dynamics and electrostatics have been introduced in order to elaborate the concept of the new model. Subsequently, the phase-resolved PIV velocity measurements by Hehner ([12],[13]), which were used to parameterize the new model and validate its quality, have been described. The derivation of the required two-dimensional body forces out of the PIV measurements with the Navier-Stokes equations have been retraced and discussed.

The new empirical model is based on the idea of positioning body force potentials of varying magnitudes in a numerical grid. The superposition of these potentials forms a scalar potential field, whose gradient represents the two dimensions of the body force. A least-square fitting process determines a set of potential magnitudes with gradients that approximate the experimental body force field. The modeled body force field has been validated through comparison with the experimental data, regarding the accuracy of the phase-averaged and phase-resolved integral body force and the spatial body force distribution. Additionally, the physical plausibility of the potential magnitudes has been discussed. Beginning from a base-line state, different configurations of the numerical setup have been presented.

Although none of these configurations was able to meet all requirements, the physical validity of the empirical model based on body force potentials is clearly indicated. In particular the integrated phase-resolved body forces show good accordance to the experimental data and thus are expected to meet the requirements as boundary conditions in CFD applications. The new model comprises a line of body force potentials on the actuator surface. This means that the complexity of modeling the body force field in two dimensions is reduced to the determination of a comparatively low quantity of potential magnitudes. Another benefit of the new model is anticipated regarding the phase-resolved spatial distribution of body force potentials, as similarities to the estimated distribution of free charges have been found. This could lead to an improved understanding of the phase-resolved discharge behavior of the actuator.

A comparison to previous models by Shyy *et al.* [28] and Jayaraman *et al.* [14], Suzen *et al.* [31] and Maden *et al.* [23] demonstrates the strengths of the new model. It is the only one with the ability to describe both dimensions of the phase-resolved body force distribution. In addition, though the current new model is solely of empirical nature, the links to the physical behavior of the plasma actuator promise further developments towards a future model that will be independent from experimental validations.

Further investigations could take a step back from the modeling process itself and start with the definition of quantitative requirements that the body force model must meet. Therefore the influence of the spatial distribution of body forces on the resulting flow field has to be analyzed.
In any case, the new model offers a basis for a vast field of examinations, aiming for improved and numerically stable potential magnitudes. Hence the numerical flaws leading to non-physical peaks of potential magnitudes, either in x- or y-direction, should be addressed. Another issue to deal with is the incorrect sign in the body forces in vertical direction. This will pave the way for a set of potential magnitudes that is able to resolve both dimensions and is expected to correspond even better to estimations of the phase-resolved charge distribution. In a next step the approach for the presented new model should be extended by the capability of reproducing different actuator configurations, as the actuation voltage and frequency or the geometry of the electrodes.
An important future step towards the integration of the new model in CFD applications, is the investigation of the effects of free stream velocities on the body force potentials. The corresponding experimental measurements have been performed by Hehner *et al.* [12, 13] and are available at the institute for further application.

Symbols and Abbreviations

Latin Formular Signs

SYMBOLS	DIMENSION	MEANING
A_S	m^2	surface of a sphere
A	m^2	surface of grid cell
$A^i_{M_k,x,y}$	$1/\mathrm{m}$	relation between local potential and local body force
$\mathbf{A}^i$	$1/\mathrm{m}$	relation between potentials and body forces
a	–	electrostriction parameter
a	m	height of discharge area
b	m	length of discharge area
c_i	–	coefficients applied by Maden *et al.* [21, 23]
$C/C(t)/C_i$	F	capacitance
C^+_eff	F	effective capacitance of positive half-cycle
C^-_eff	F	effective capacitance of negative half-cycle
C_0	F	cold capacitance
$\vec{D}$	–	displacement vector
$\vec{E}/E$	$\mathrm{V/m}$	electric field
E_b	$\mathrm{V/m}$	breakdown field strength
E_0	$\mathrm{V/m}$	maximum electric field strength
e	C	electron charge
$\vec{F}_\mathrm{e}$	N	electrostatic force
$\tilde{F}$	J	thermodynamic potential
F_0	J	thermodynamic potential in the absence of an electric field
F^i_int	N	integrated body force for the whole actuator
f^i_int	$\mathrm{N/m}$	integrated body force per actuator length
$\vec{f}/\vec{f}_\mathrm{b}$	$\mathrm{N/m}^3$	body force
f^X	$\mathrm{N/m}^3$	body force in x-direction

f^Y	$\mathrm{N/m^3}$	body force in y-direction
$f_\#$	–	f-number
I	A	electric current
i, j	–	control variables of the coordinates
k	–	control variables of the potential position
k	$\mathrm{kg\ m^2/s^2K}$	Boltzmann's constant
k_1/k_2	$\mathrm{V/m^2}$	coefficients applied by Shyy *et al.* [28]
L	m	length of electrodes (z-direction)
M	–	potential magnitude
m	kg	mass
$\vec{n}$	–	surface normal
n	$\mathrm{1/m^3}$	charge number density
n_i	$\mathrm{1/m^3}$	density of ions
n_n	$\mathrm{1/m^3}$	density of neutrals
p_st	$\mathrm{N/m^2}$	electrostrictive force
Q	C	electric charge
q_i	C	single electric charge
q_c	$\mathrm{C\ m^3}$	charge density
R	Σ	electric resistance
R_i	$\mathrm{kg/m^3\ s}$	chemical production rate of component i
r	m	radius
Stk	–	Stokes number
T	K	temperature
T_e	K	temperature of electrons
T_i	K	temperature of ions
T_n	K	temperature of neutrals
T'	eV	kinetic temperature
t	s	time
U_∞	m/s	free stream velocity
$\vec{u}/u$	m/s	velocity
t_i	s	time step i
$V/V(t)$	V	voltage (peak-to-peak)
V_max	V	maximum operating voltage (peak-to-peak)
V_supply	V	supply voltage
$\vec{v}_\mathrm{d}$	m/s	drift velocity

X	–	chordwise direction
x	m	chordwise coordinate
x_0	m	chordwise position of the potential singularity
$x_{\min}/x_{\max}$	m	lowest/highest chordwise coordinate in the numerical grid
Y	–	wall normal direction
y	m	wall normal coordinate
y_0	m	wall normal position of the potential singularity
$y_{\min}/y_{\max}$	m	lowest/highest wall normal coordinate in the numerical grid

Greek Formular Signs

SYMBOLS	DIMENSION	MEANING
α	–	degree of ionization
α	–	coefficient for a relation between potential magnitudes and charge density
ΔL	m	length of virtual electrode
$\Delta\varphi$	–	discrete phase step
Δx	m	chordwise grid cell length
Δy	m	wall normal grid cell height
ϵ	C/Vm	permittivity
ϵ_0	C/Vm	permittivity of vacuum
ϵ_r	C/Vm	relative permittivity
λ_d	m	Debye length
μ_m	N s/m^2	collision frequency
ν_m	1/s	collision frequency
ρ	kg/m^3	density
τ	N/m^2	stress tensor
Φ	V	sum of electric potential of the external electric field and free charges
ϕ	V	electric potential of the external electric field
ϕ	–	electric/velocity/body force potential

φ	V	electric potential of free charges
φ	–	phase

Abbreviations

SYMBOLS	MEANING
AC	alternating current
CFD	Computational Fluid Dynamics
CV	control volume
DBD	Dielectric Barrier Discharge
DC	direct current
DEHS	di-ethyl-hexylsebacat
EBFs	experimental body forces
EHD	electrohydrodynamic
FOV	field of view
HV	high voltage
KIT	Karlsruhe Institute of Technology
MBFs	modeled body forces
Nd:YLF	eodymium-doped yttrium lithium fluoride
PhD	Doctor of Philosophy
PIV	Particle Image Velocimetry
PMs	potential magnitudes

List of Figures

List of Tables

Bibliography

[1] N. Benard, A. Debien, and E. Moreau. Time-dependent volume force produced by a non-thermal plasma actuator from experimental velocity field. *Journal of Physics D: Applied Physics*, 46:245201, 2013.

[2] N. Benard and E. Moreau. Electrical and mechanical characteristics of surface ac dielectric barrier discharge plasma actuators applied to airflow control. *Experiments in Fluids*, 2014.

[3] A. Castellanos. *Electrohydrodynamics*. Springer-Verlag Wien GmbH, 1998.

[4] L. Cattafesta and M. Sheplak. Actuators for active flow control. *Annual Review of Fluid Mechanics*, 43:247–272, 2011.

[5] T. Corke, C. L. Enloe, and S. Wilkinson. Dielectric barrier discharge plasma actuators for flow control. *Annual Review of Fluid Mechanics*, 42:505–529, 2009.

[6] C. L. Enloe, T. Corke, E. Jumper, K. Kachner, T. McLaughlin, and R. Dyken. Mechanisms and responses of a single dielectric barrier plasma actuator: Plasma morphology. *AIAA Journal*, 42:589–594, 2004.

[7] C. L. Enloe, M. Mcharg, G. Font, and T. McLaughlin. Plasma-induced force and self-induced drag in the dielectric barrier discharge aerodynamic plasma actuator. *47th AIAA Aerospace Sciences Meeting including the New Horizons Forum and Aerospace Exposition*, 2009.

[8] D. Fong and M. Saunders. LSMR: An iterative algorithm for sparse least-squares problems. *Computing Research Repository*, 33, 2010.

[9] G. Francis. The glow discharge at low pressure. *Encyclopedia of Physics*, 22:53–61, 1956.

[10] M. Gad-el Hak. *Flow Control: Passive, Active, and Reactive Flow Management*. Cambridge University Press, New York, 2007.

[11] C. Gerthsen and H.Vogel. *Gerthsen Physik*. Springer-Verlag Berlin Heidelberg New York, 01 1999.

[12] M. Hehner, G. Coutinho, S. Najam, R. Pereira, and J.Kriegseis. Phase-resolved body-force estimation of AC-DBD plasma actuator at various airflow speeds. *15th International Conference on Fluid Control, Measurements and Visualization*, 2019.

[13] M. Hehner, G. Coutinho, R. Pereira, N. Benard, and J. Kriegseis. On the interplay of body forces and flow speed for DBD-based flow control. In *In proceedings for Journal of Physics D: Applied Physics*.

[14] B. Jayaraman and W. Shyy. Flow control and thermal management using dielectric glow discharge concepts. *American Institute of Aeronautics and Astronautics*, 2003.

[15] M. Kotsonis. Diagnostics for characterisation of plasma actuators. *Measurement Science and Technology*, 26, 09 2015.

[16] J. Kriegseis. *Performance Characterization and Quantification of Dielectric Barrier Discharge Plasma Actuators*. PhD thesis, TU Darmstadt, 2011.

[17] J. Kriegseis, C. Schwarz, C. Tropea, and S. Grundmann. Velocity-information-based force-term estimation of dielectric-barrier discharge plasma actuators. *Journal of Physics D: Applied Physics*, 46:055202, 2013.

[18] J. Kriegseis, B. Simon, and S. Grundmann. Towards in-flight applications? a review on dielectric barrier discharge-based boundary-layer control. *Applied Mechanics Reviews*, 68:020802–1:020802–41, 2016.

[19] M. Kuhnhenn, S. Bernhard, I. Maden, and J. Kriegseis. Interrelation of phase-averaged volume force and capacitance of dielectric barrier discharge plasma actuators. *Journal of Fluid Mechanics*, 809, 2016.

[20] L. Landau and E. Lifchitz. Electrodynamique des milieux continus. *MIR Moscow*, 87:336–344, 1966.

[21] I. Maden. *Numerische Untersuchung zur aktiven Strömungsbeeinflussung durch Plasma-Aktuatoren: Modellentwicklung und Anwendung*. PhD thesis, 2017.

[22] I. Maden, J. Kriegseis, R. Maduta, S. Jakirlić, C. Schwarz, S. Grundmann, and C. Tropea. Derivation of a plasma-actuator model utilizing quiescent-air piv data. *20th Annual Conference of the CFD Society ofCanada, Canmore, AB, Canada*, 2012.

[23] I. Maden, R. Maduta, J. Kriegseis, S. Jakirlić, C. Schwarz, S. Grundmann, and C. Tropea. Experimental and computational study of the flow induced by a plasma actuator. *International Journal of Heat and Fluid Flow*, 41:80–89, 2013.

[24] E. Moreau. Airflow control by non-thermal plasma actuators. *Journal of Physics D: Applied Physics*, 40:605, 2007.

[25] J. R. Roth. *Industrial Plasma Engineering; Volume 1: Principles*. Institute of Physics Publishing, 1995.

[26] J. R. Roth, D.M. Sherman, and S.P Wilkinson. Proceedings of the AIAA 36th aerospace sciences meeting and exhibit. *Reno, NV*, 1998.

[27] A. Sciacchitano and B. Wieneke. PIV uncertainty propagation. *Measurement Science and Technology*, 27:084006, 2016.

[28] W. Shyy, B. Jayaraman, and A. Andersson. Modeling of glow discharge-induced fluid dynamics. *Journal of Applied Physics*, 92(11):6434 – 6443, 2002.

[29] J. Spurk and N. Aksel. *Strömungslehre: Einführung in die Theorie der Strömungen*. Springer-Verlag Berlin Heidelberg, 2019.

[30] C. Steffes. Erste Ansätze einer neuen Strategie zur effizienten Modellierung eines Plasma-Aktuators auf Basis des Verständnisses bestehender Modelle. Master's thesis, TU Darmstadt, 2008.

[31] Y. Suzen, P. Huang, and D. Ashpis. Numerical simulations of flow separation control in low-pressure turbines using plasma actuators. *Collection of Technical Papers - 45th AIAA Aerospace Sciences Meeting*, 16, 2007.

[32] Y. Suzen, P. Huang, J. Jacob, and D. Ashpis. Numerical simulations of plasma based flow control applications. *AIAA 35th Fluid Dynamics Conference and Exhibit*, 2005.

[33] B. Wilke. *Aerodynamische Strömungssteuerung mittels dielektrischen Barriereentladungs-Plasmaaktuatoren.* PhD thesis, TU Darmstadt, DLR Göttingen, 2009.

Appendix

The complete appendix is only available in the digital version of the thesis due to its extent.

A. Phase-resolved PIV velocity measurements

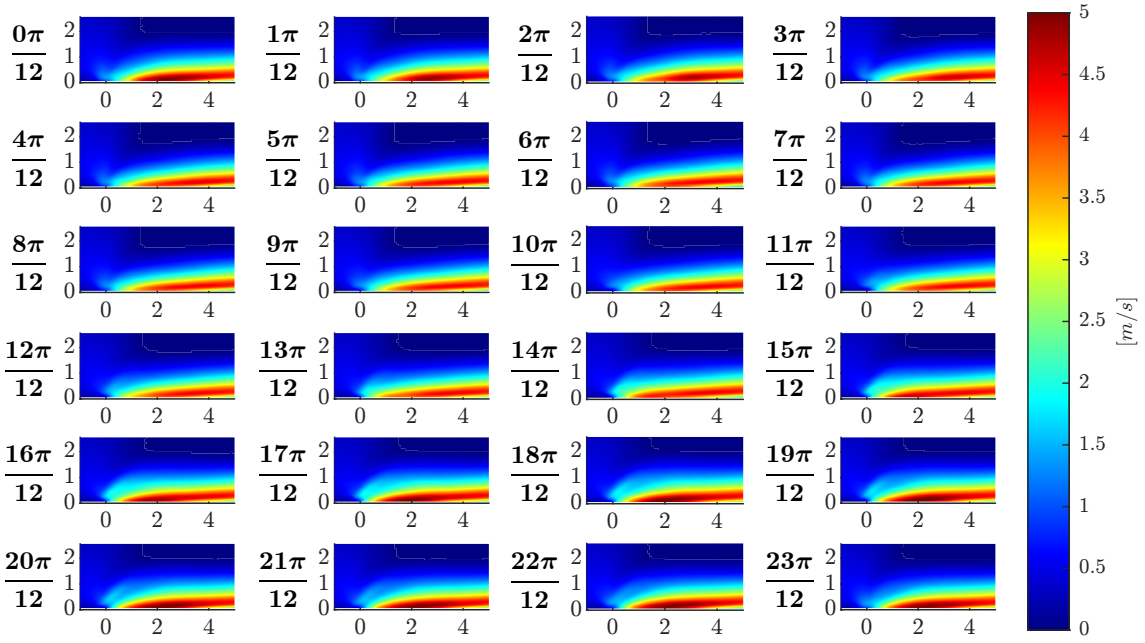

Figure A.1.: Phase resolved velocity measurements in horizontal direction (u) by Hehner *et al.* ([12],[13]). The coordinates are in [mm]

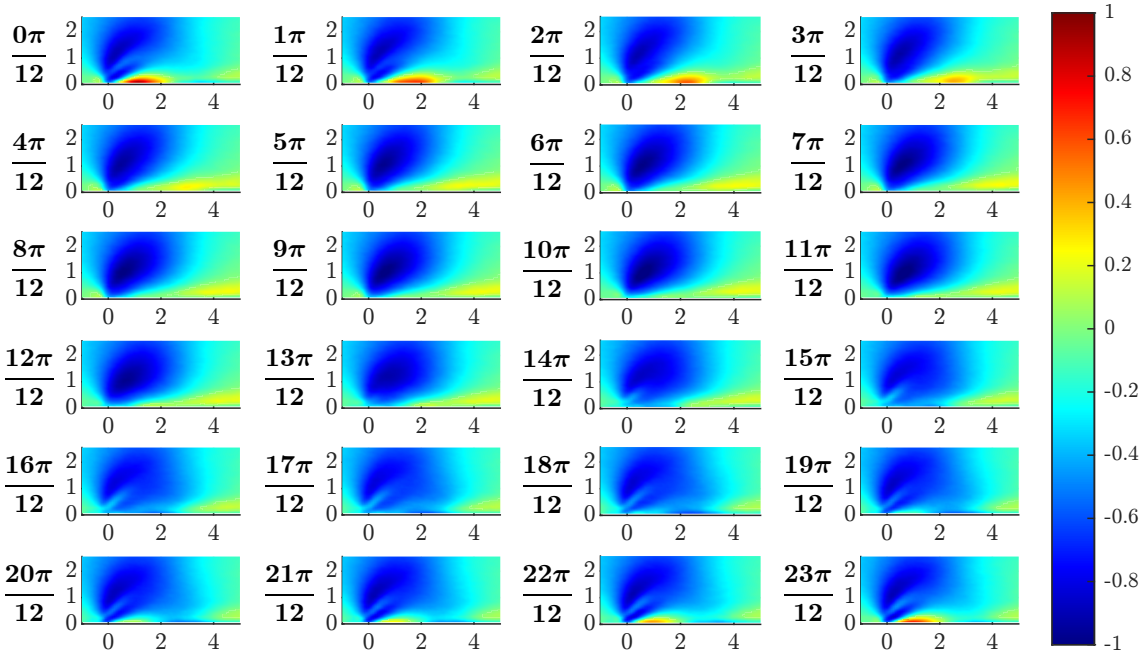

Figure A.2.: Phase resolved velocity measurements in vertical direction (v) by Hehner *et al.* ([12],[13]). The coordinates are in [mm]

B. Complete figure list of body force fields in baseline-state

X-Direction

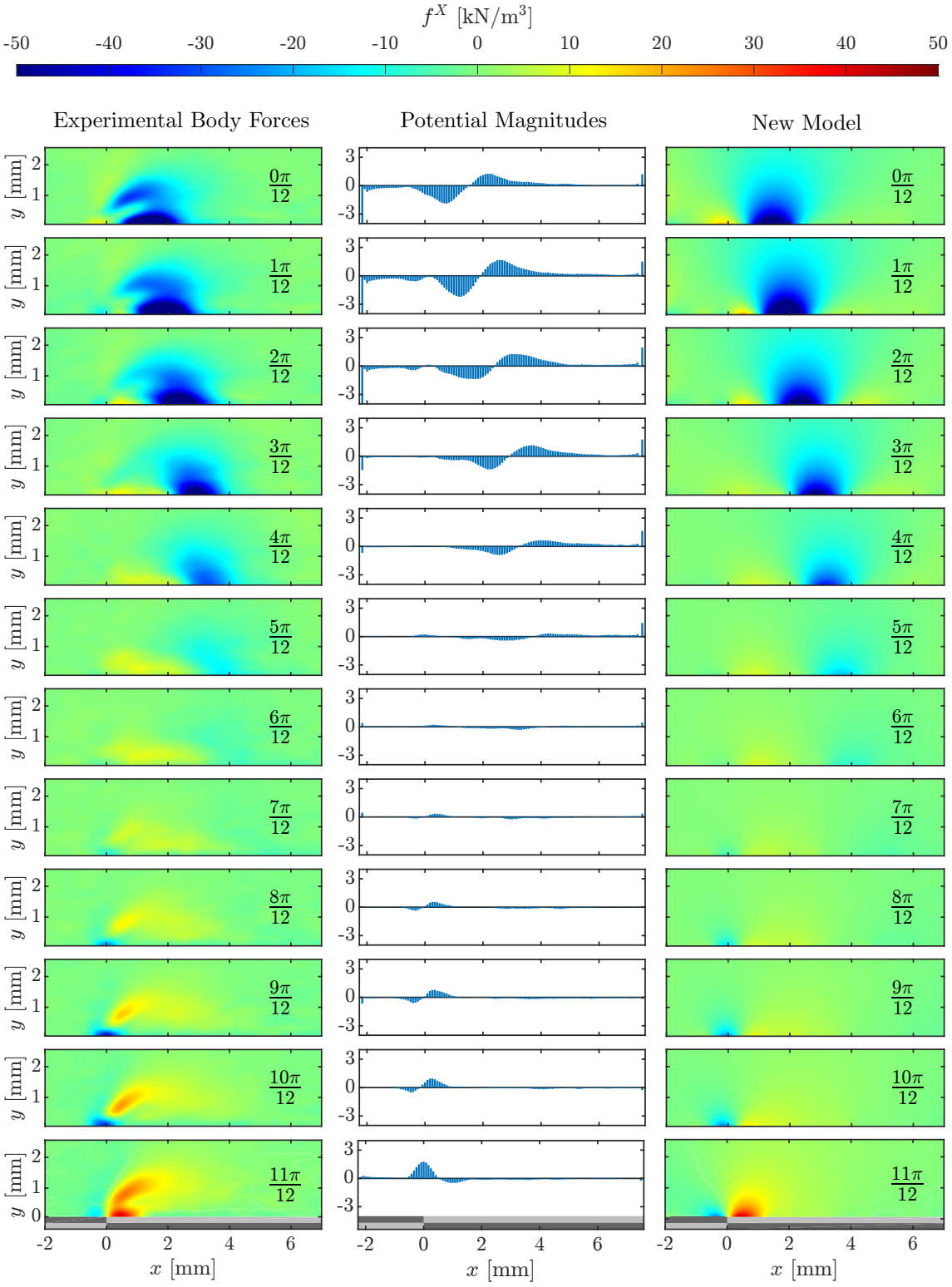

Figure B.3.: Baseline state: Modeling results in x-direction, phases 0 to $11\pi/12$. Experimental body forces according to Hehner *et al.* [12, 13].

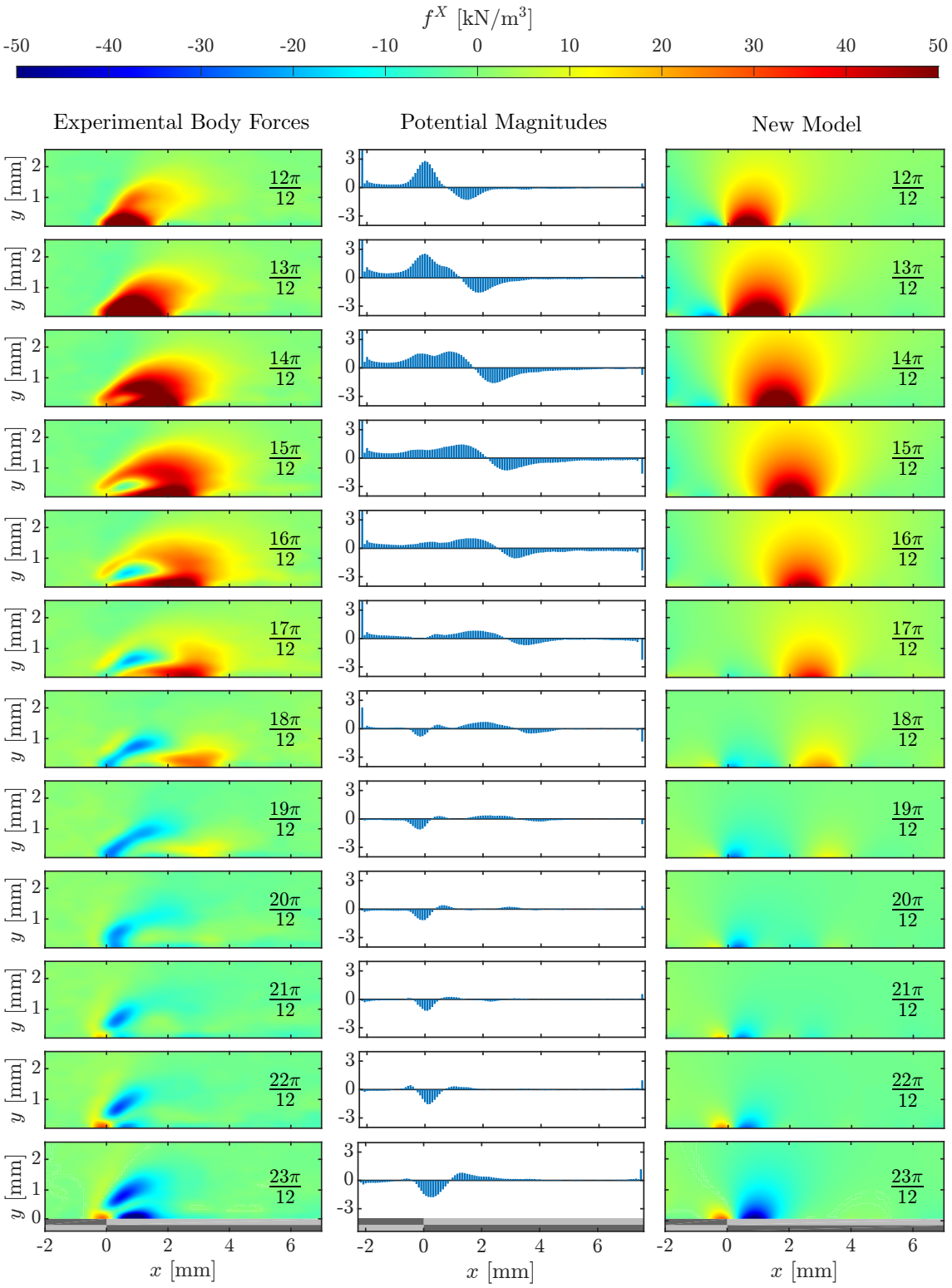

Figure B.4.: Baseline state: Modeling results in x-direction, phases $12\pi/12$ to $23\pi/12$. Experimental body forces according to Hehner *et al.* [12, 13].

Y-Direction

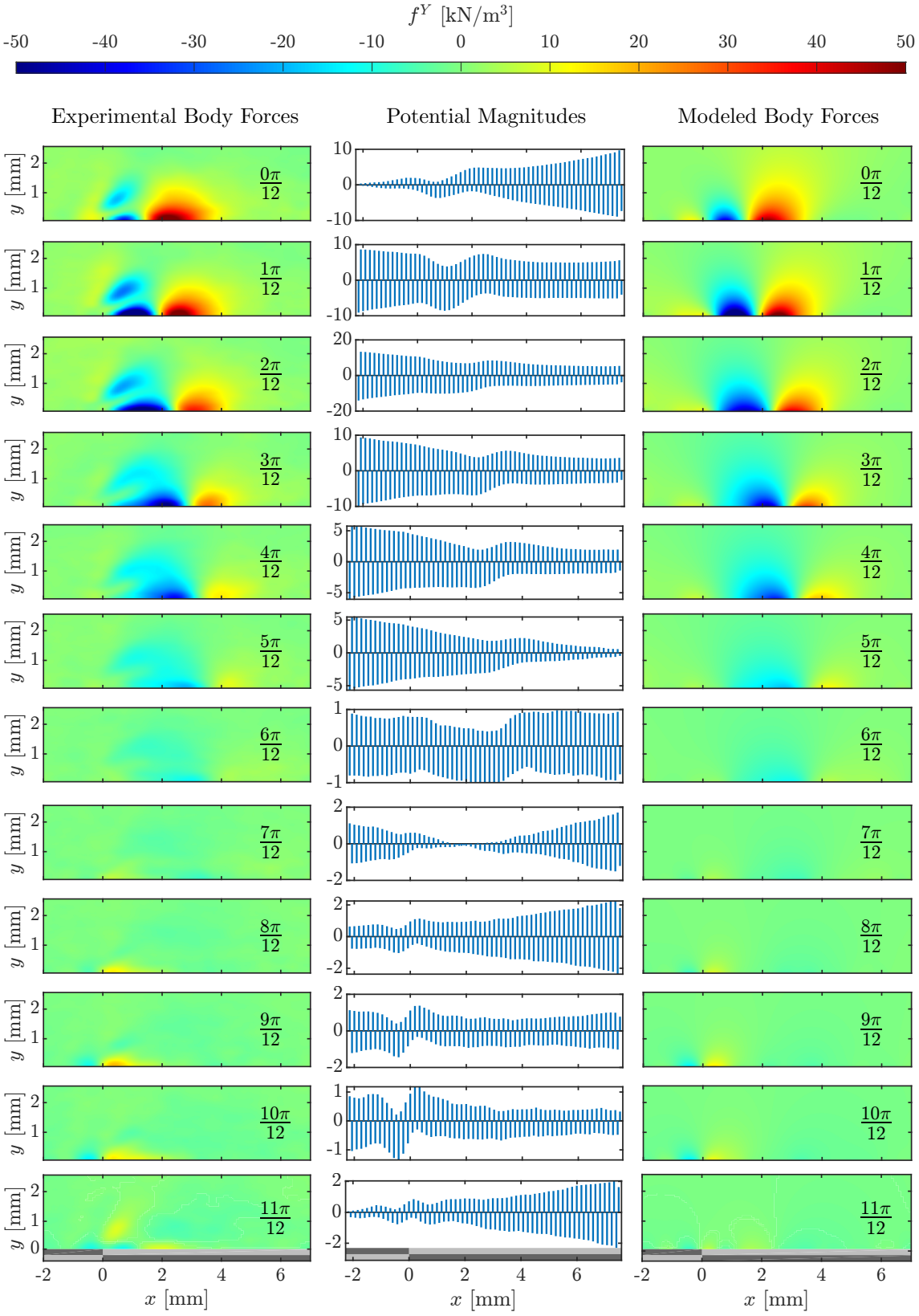

Figure B.5.: Baseline state: Modeling results in y-direction, phases 0 to $11\pi/12$. Note that the ordinate limits of the PMs are not uniform. Experimental body forces according to Hehner *et al.* [12, 13].

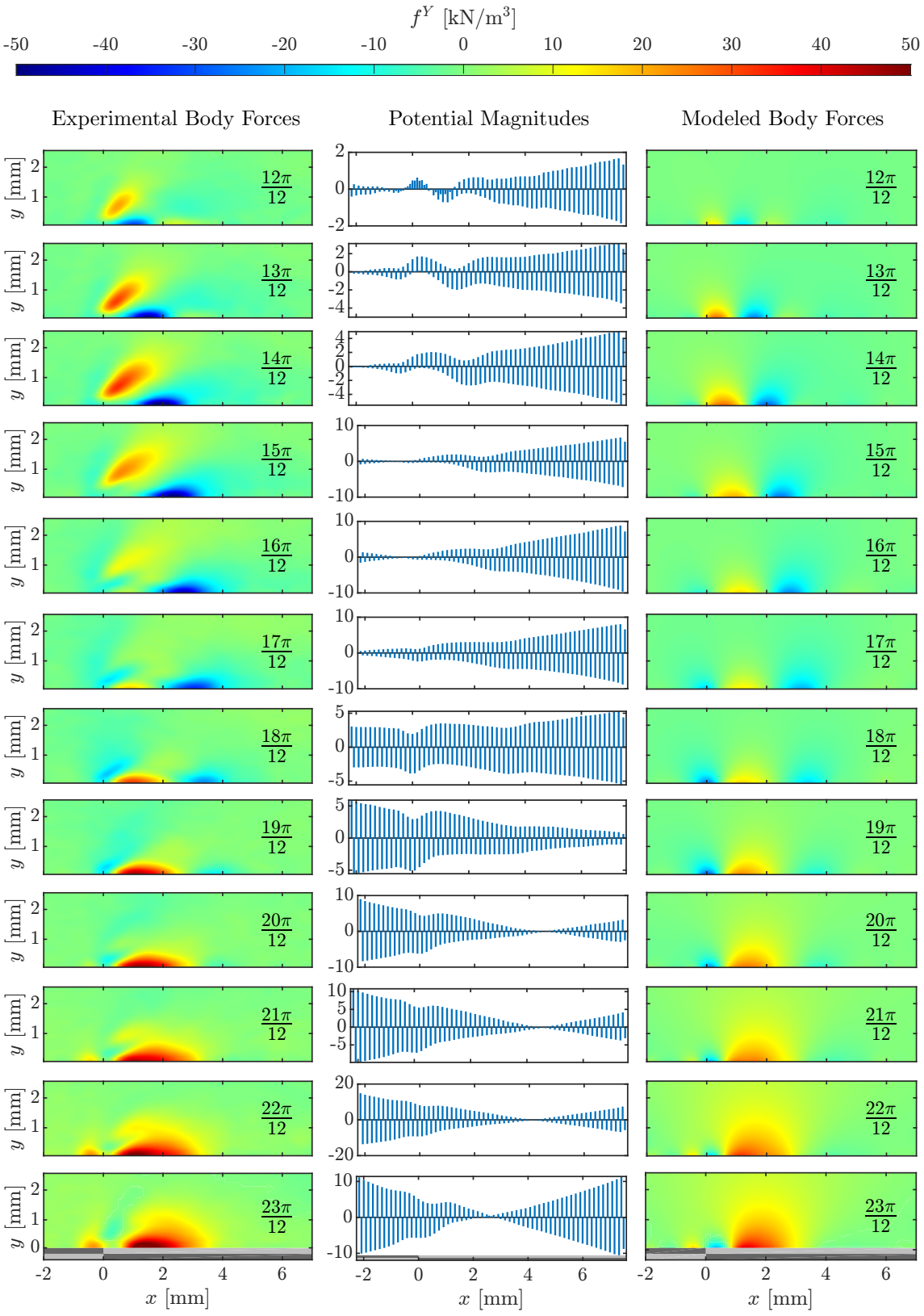

Figure B.6.: Baseline state: Modeling results in y-direction, phases $12\pi/12$ to $23\pi/12$. Note that the ordinate limits of the PMs are not uniform. Experimental body forces according to Hehner *et al.* [12, 13].

Y-Direction computed with PM x-vector

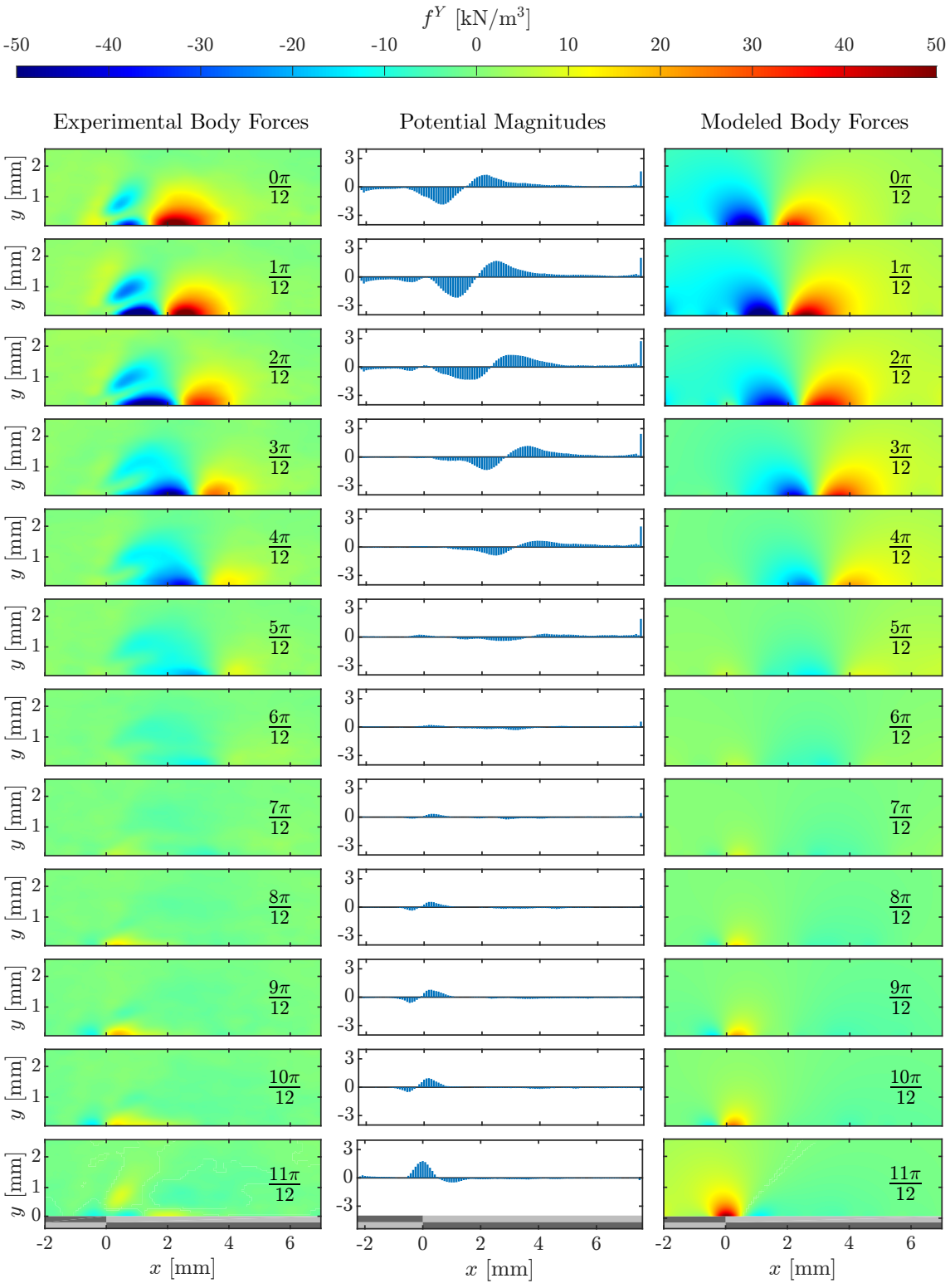

Figure B.7.: Modeling results in y-direction with the input of PMs in x, phases 0 to $11\pi/12$. Experimental body forces according to Hehner *et al.* [12, 13].

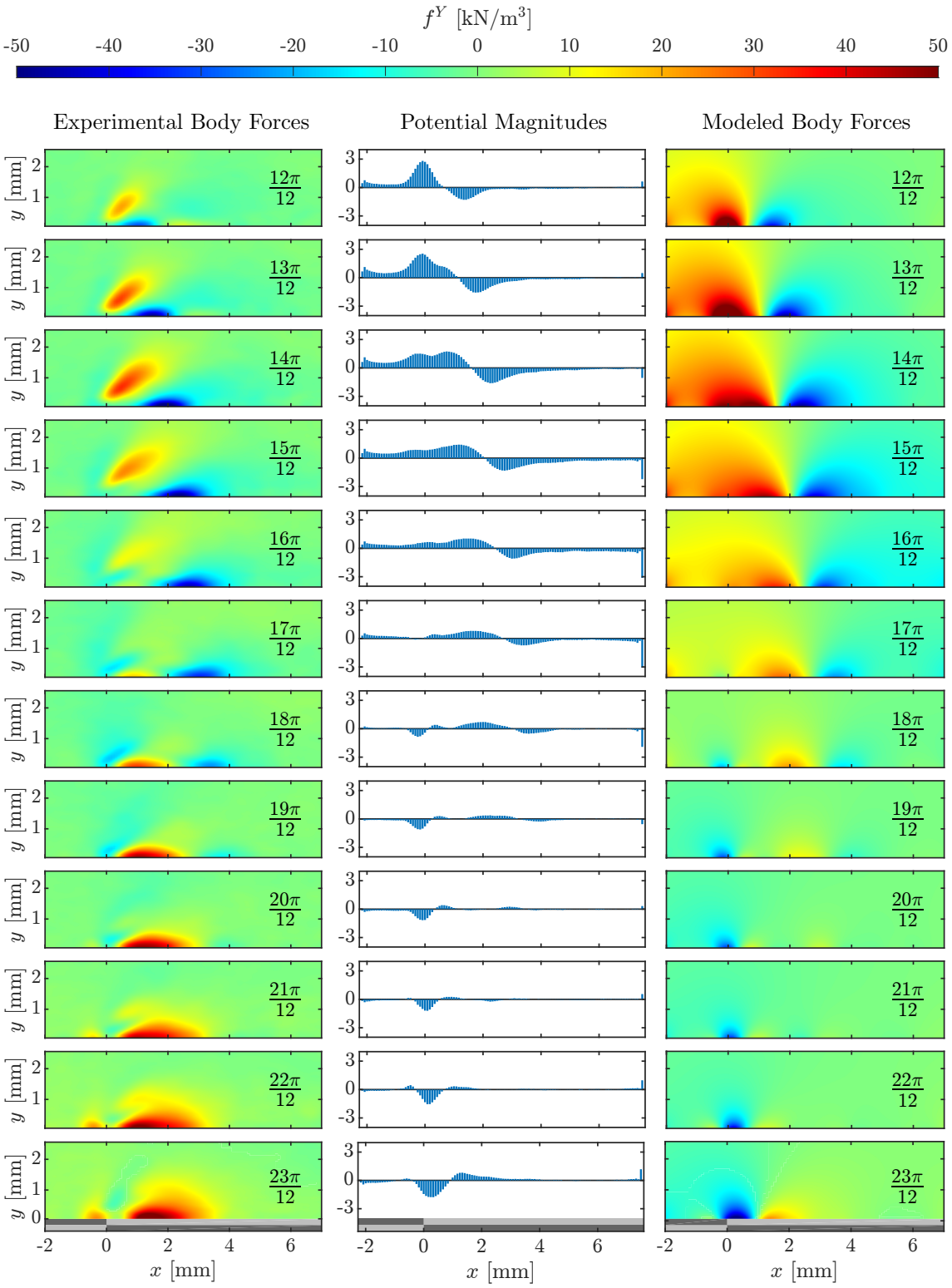

Figure B.8.: Modeling results in y-direction with the input of PMs in x, phases $12\pi/12$ to $23\pi/12$. Experimental body forces according to Hehner *et al.* [12, 13].

X-Direction for a common PM vector for x and y

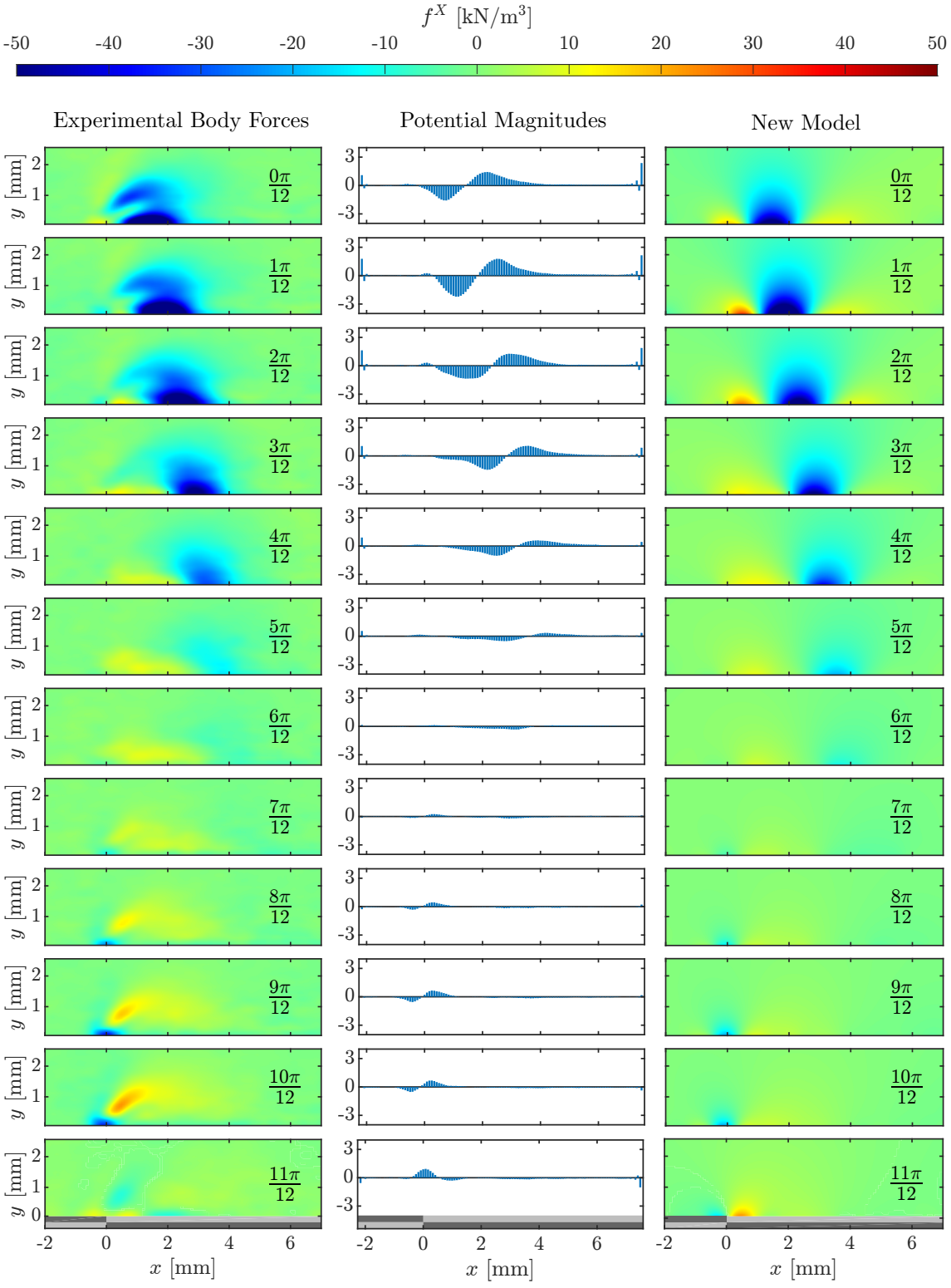

Figure B.9.: Modeling results in y-direction with common PMs for x and y, phases 0 to $11\pi/12$. Experimental body forces according to Hehner *et al.* [12, 13].

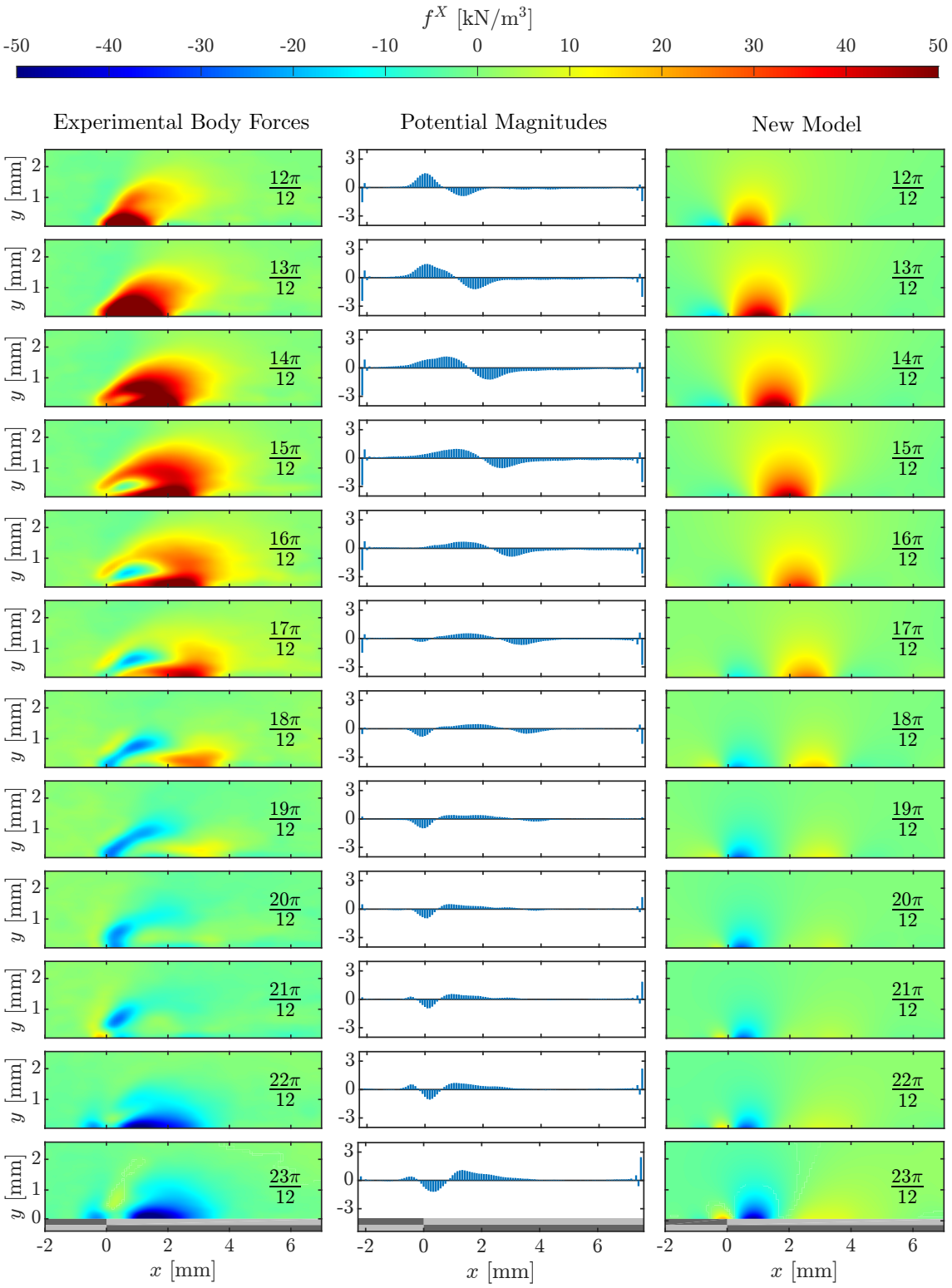

Figure B.10.: Modeling results in y-direction with common PMs for x and y, phases $12\pi/12$ to $23\pi/12$. Experimental body forces according to Hehner *et al.* [12, 13].

Y-Direction for a common PM vector for x and y

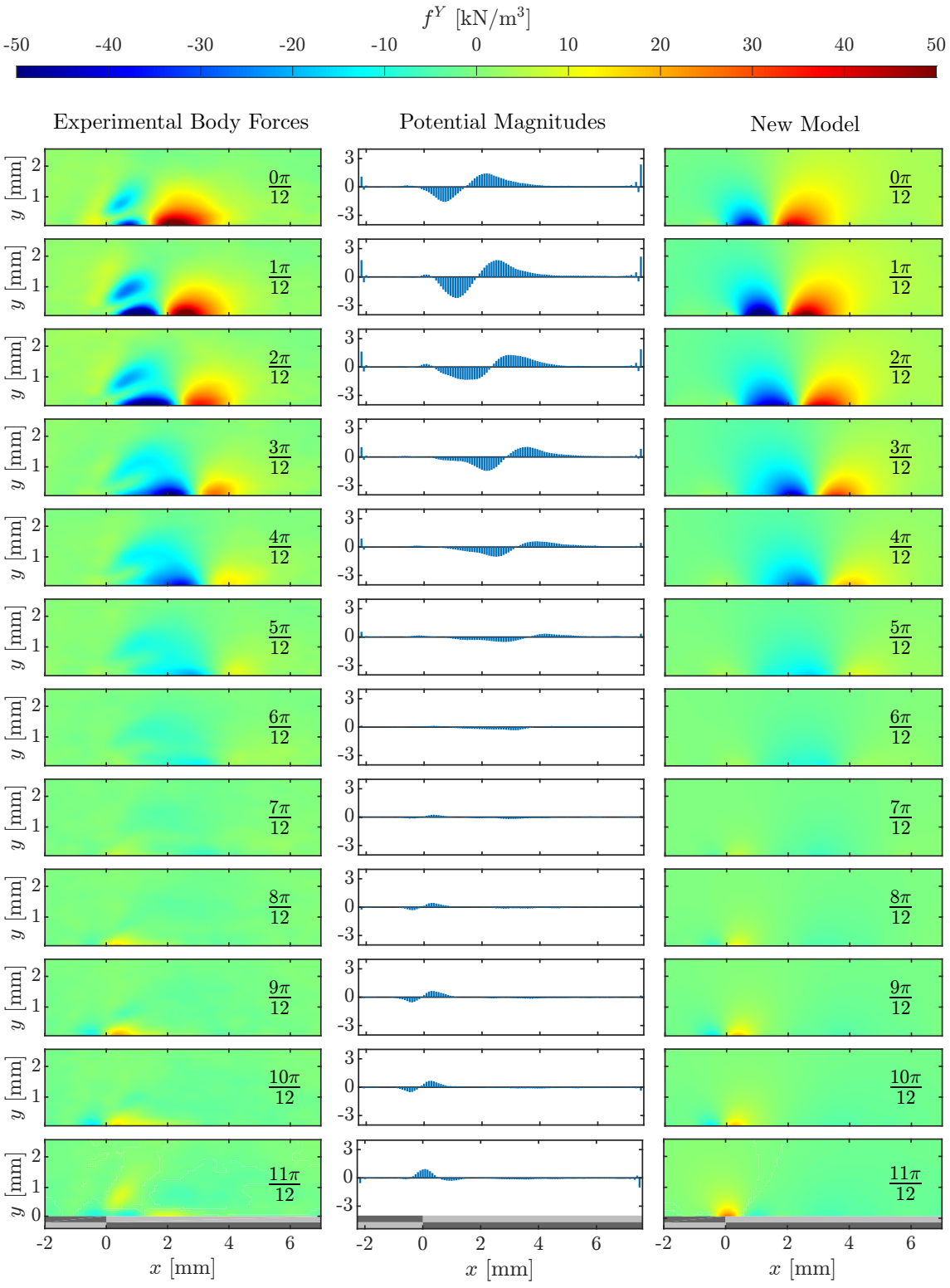

Figure B.11.: Modeling results in y-direction with common PMs for x and y, phases 0 to $11\pi/12$. Experimental body forces according to Hehner *et al.* [12, 13].

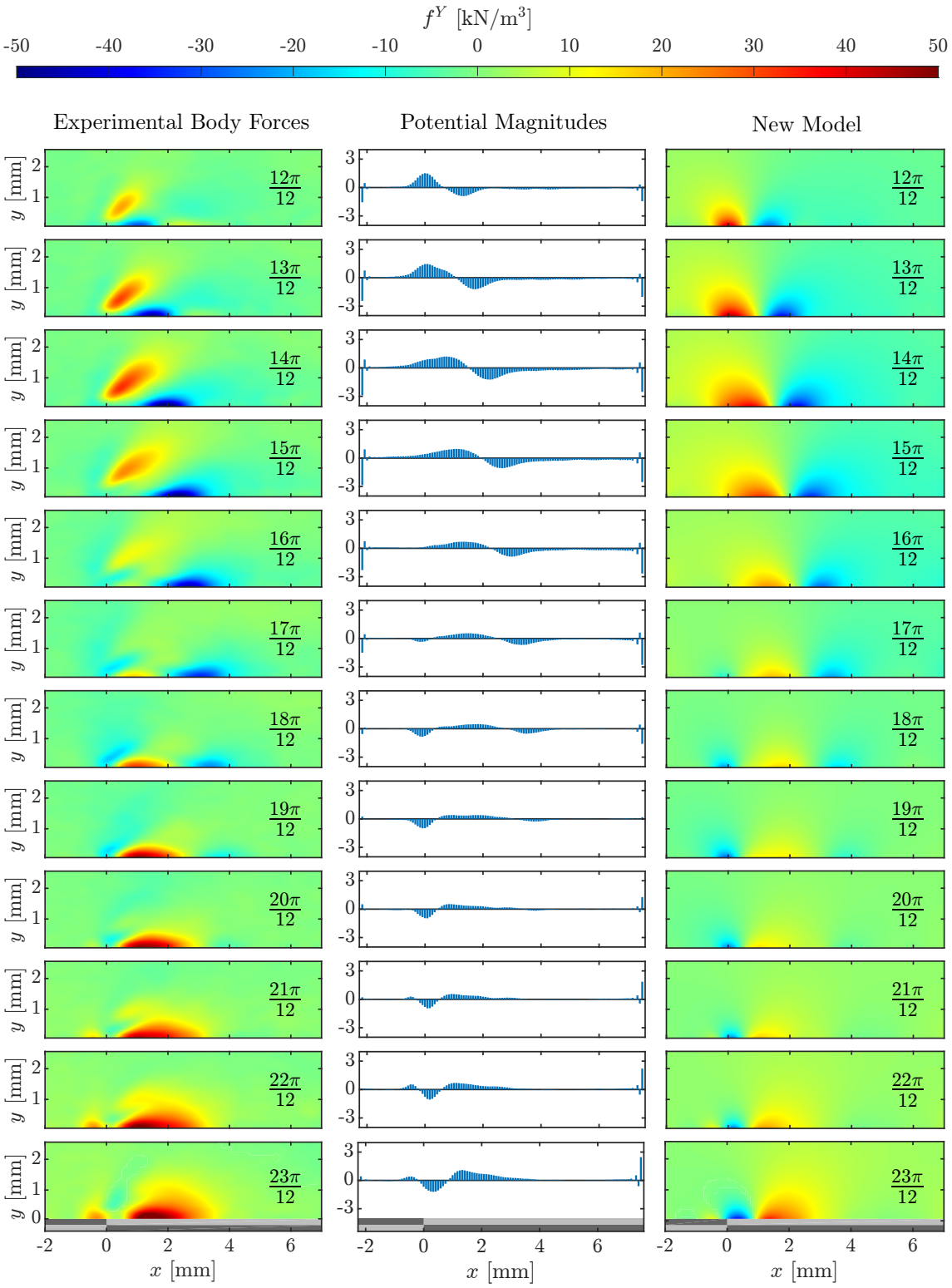

Figure B.12.: Modeling results in y-direction with common PMs for x and y, phases $12\pi/12$ to $23\pi/12$. Experimental body forces according to Hehner *et al.* [12, 13].

C. Complete figure list for a broken rational potential formulation

X-Direction: Phases 0 **to** $11\pi/12$

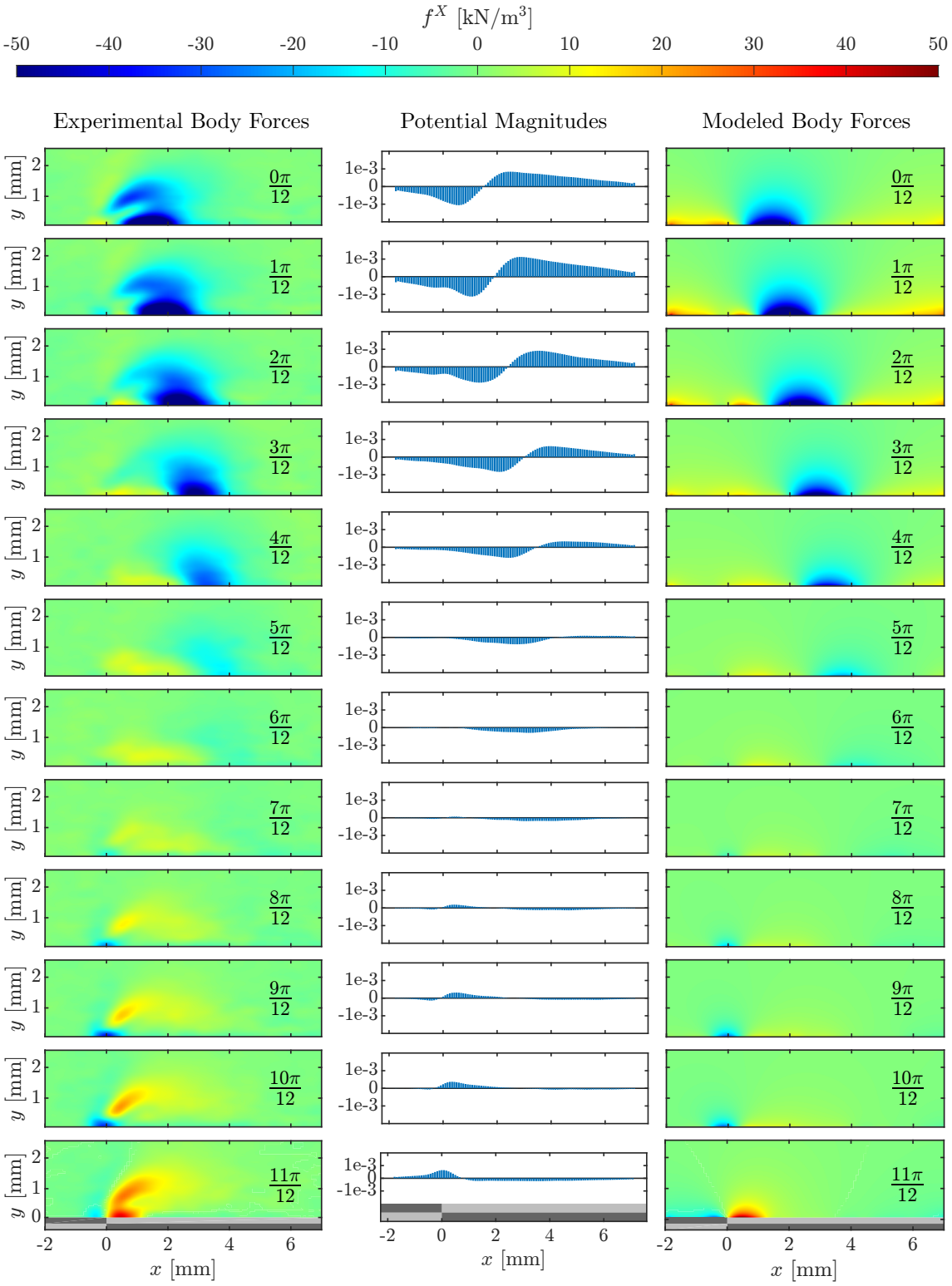

Figure C.13.: Broken rational potential formulation in x-direction, phases 0 to $11\pi/12$. Experimental body forces according to Hehner *et al.* [12, 13].

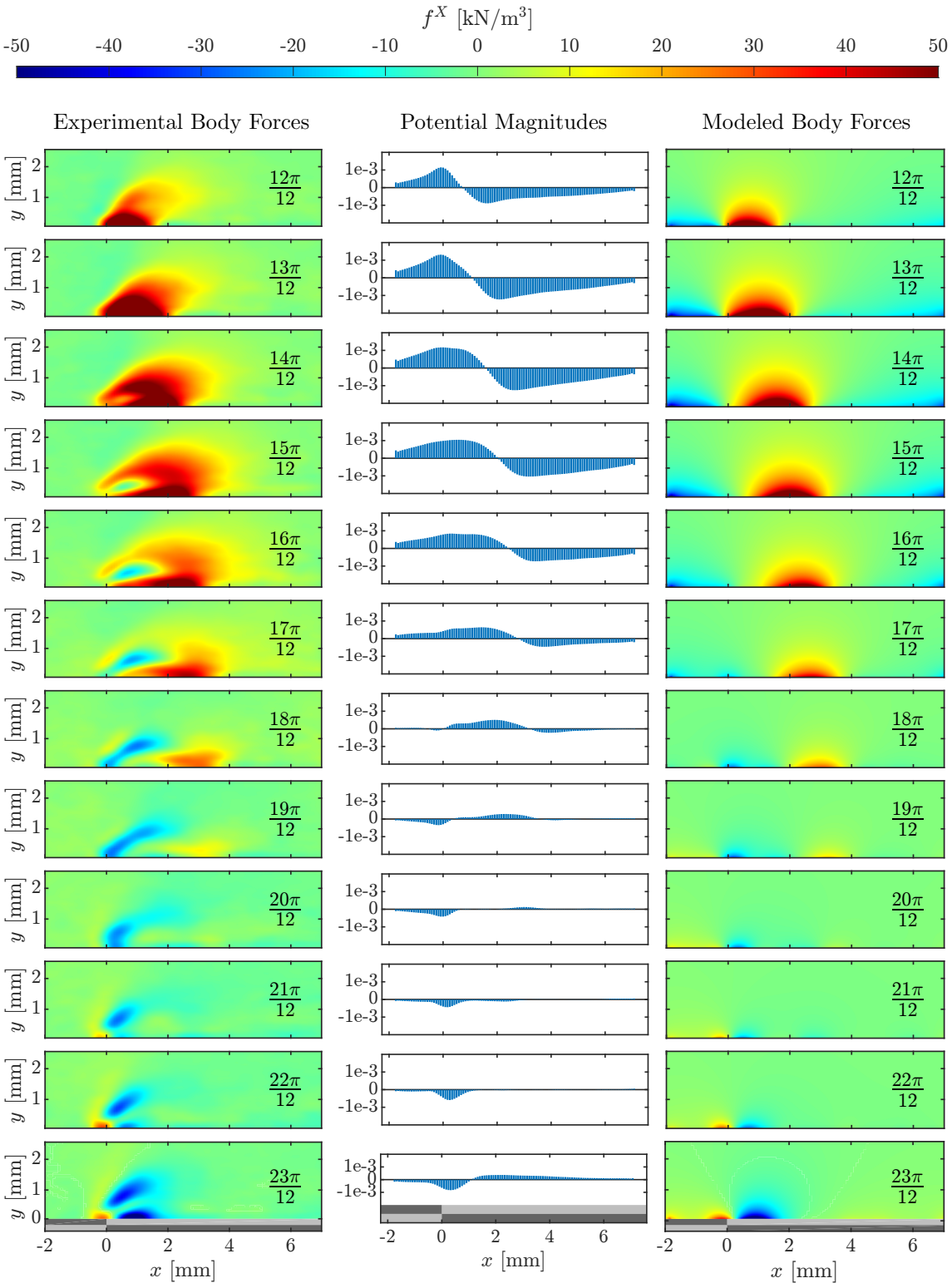

Figure C.14.: Broken rational potential formulation in x-direction, phases $12\pi/12$ to $23\pi/12$. Experimental body forces according to Hehner *et al.* [12, 13].

Y-Direction: Phases 0 **to** $11\pi/12$

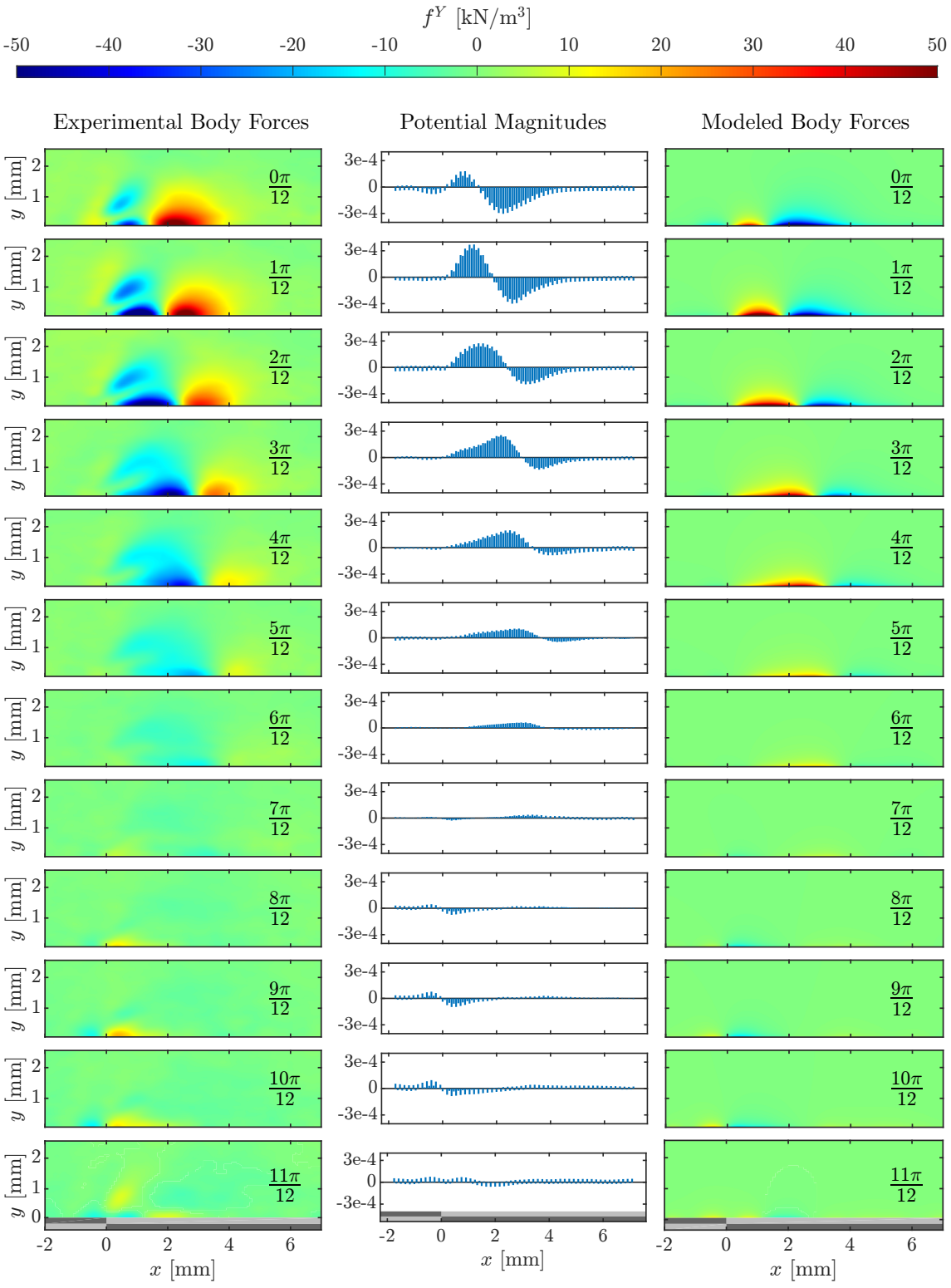

Figure C.15.: Broken rational potential formulation in y-direction, phases 0 to $11\pi/12$. Experimental body forces according to Hehner *et al.* [12, 13].

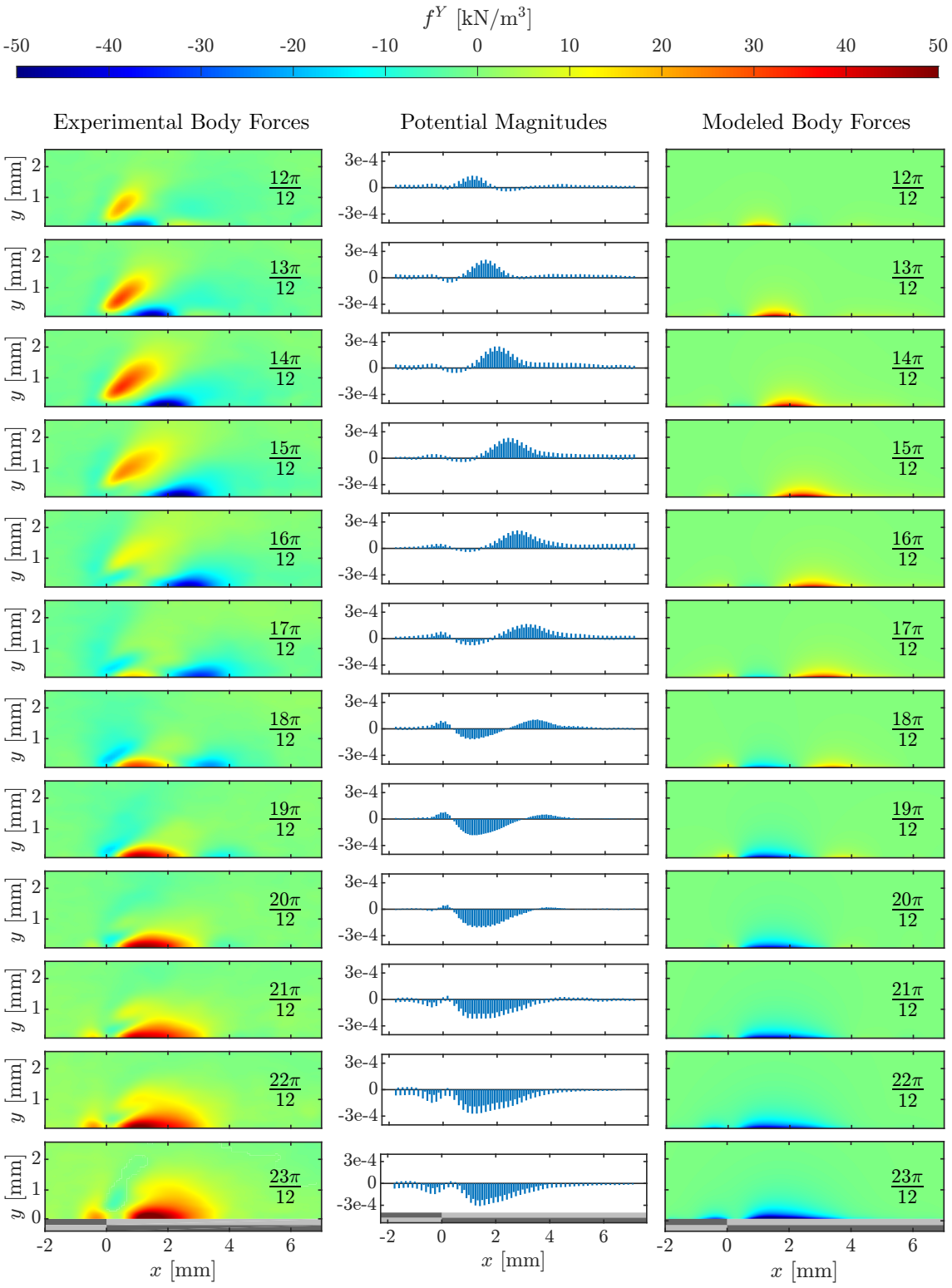

Figure C.16.: Broken rational potential formulation in y-direction, phases $12\pi/12$ to $23\pi/12$. Experimental body forces according to Hehner *et al.* [12, 13].

D. Complete figure list for an exponential potential description

X-Direction

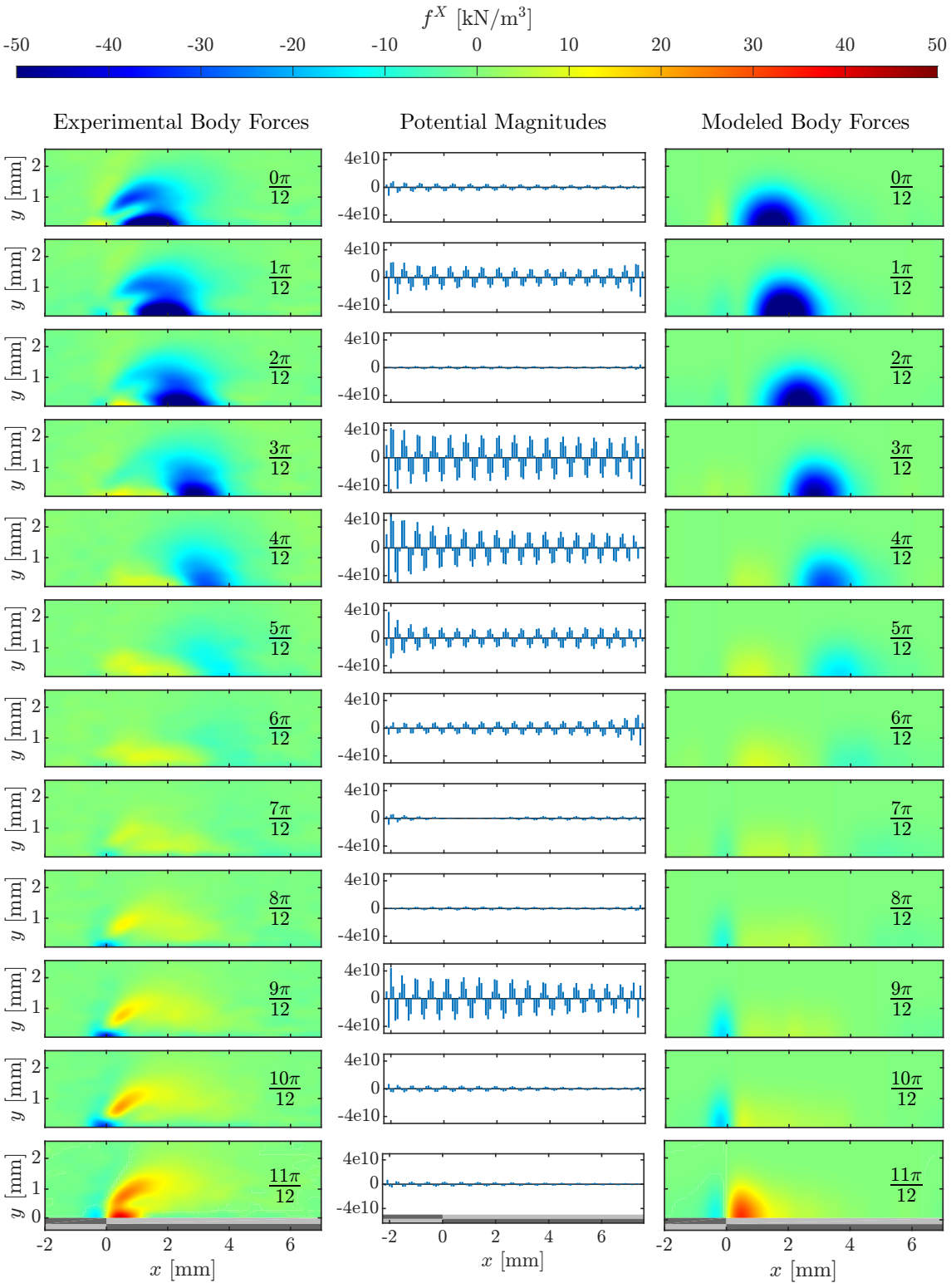

Figure D.17.: Exponential potential formulation, x-direction, phases 0 to $11\pi/12$. Experimental body forces according to Hehner *et al.* [12, 13].

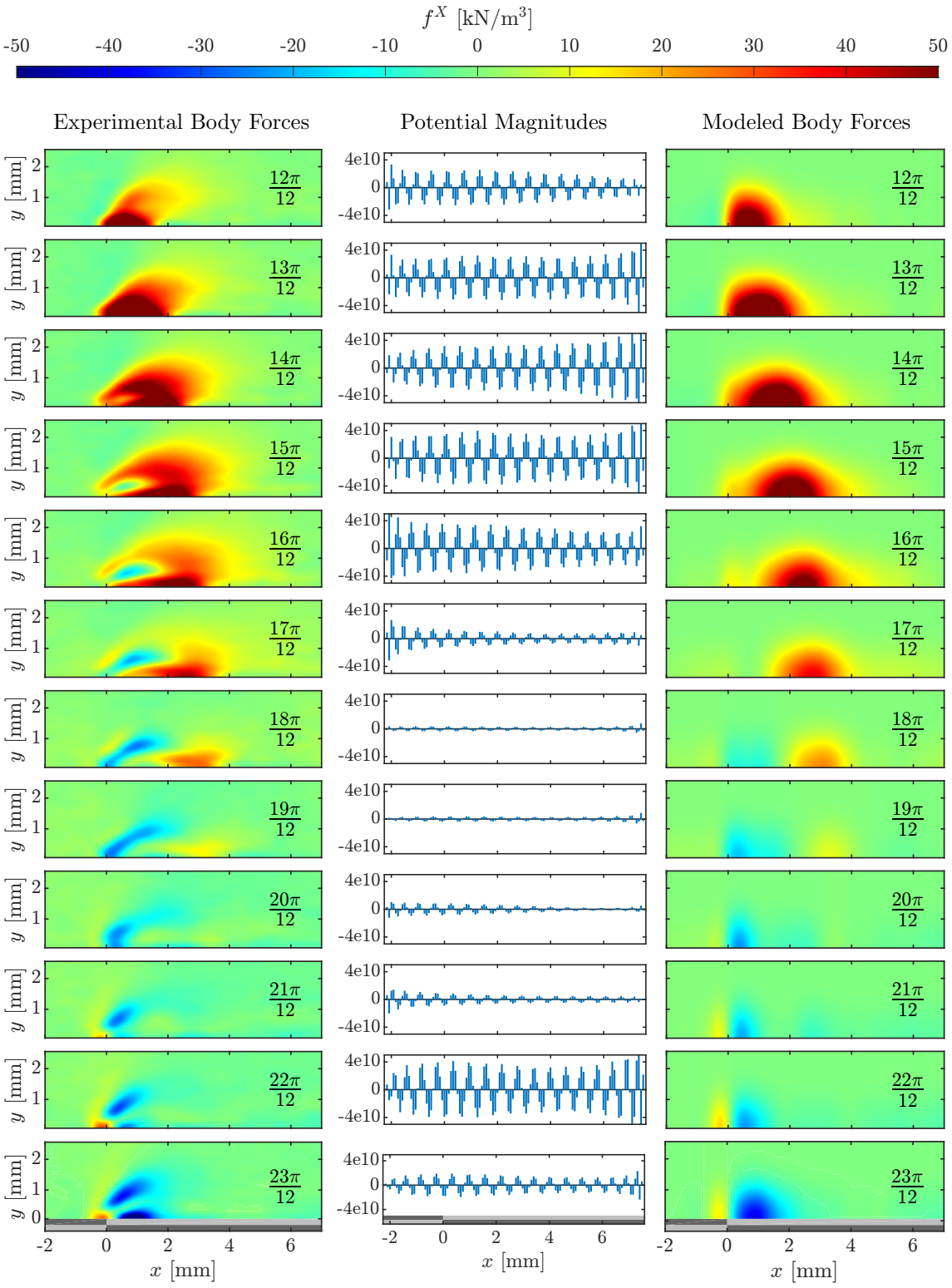

Figure D.18.: Exponential potential formulation, x-direction, phases $12\pi/12$ to $23\pi/12$. Experimental body forces according to Hehner *et al.* [12, 13].

Y-Direction

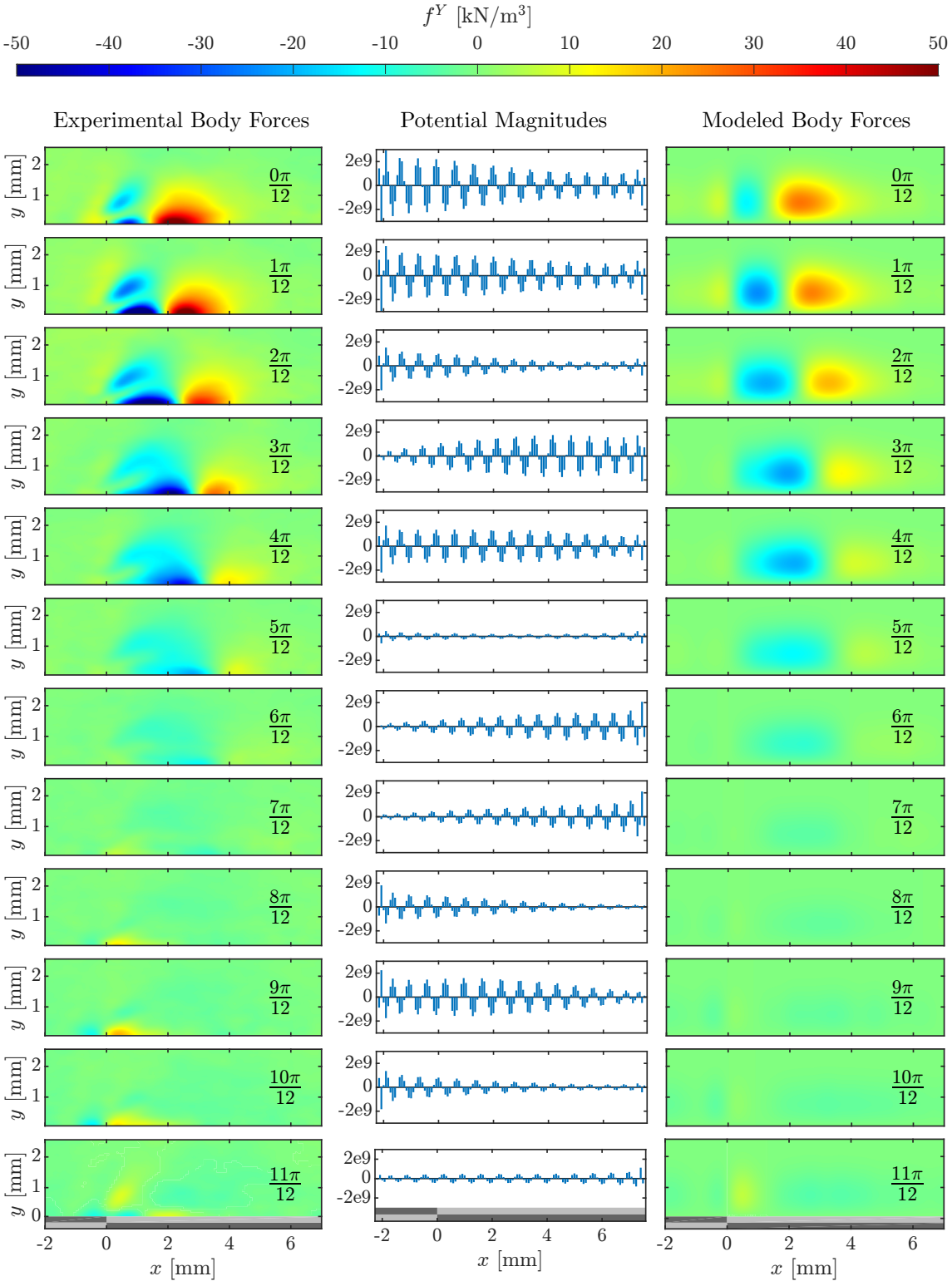

Figure D.19.: Exponential potential formulation, y-direction, phases 0 to $11\pi/12$. Experimental body forces according to Hehner *et al.* [12, 13].

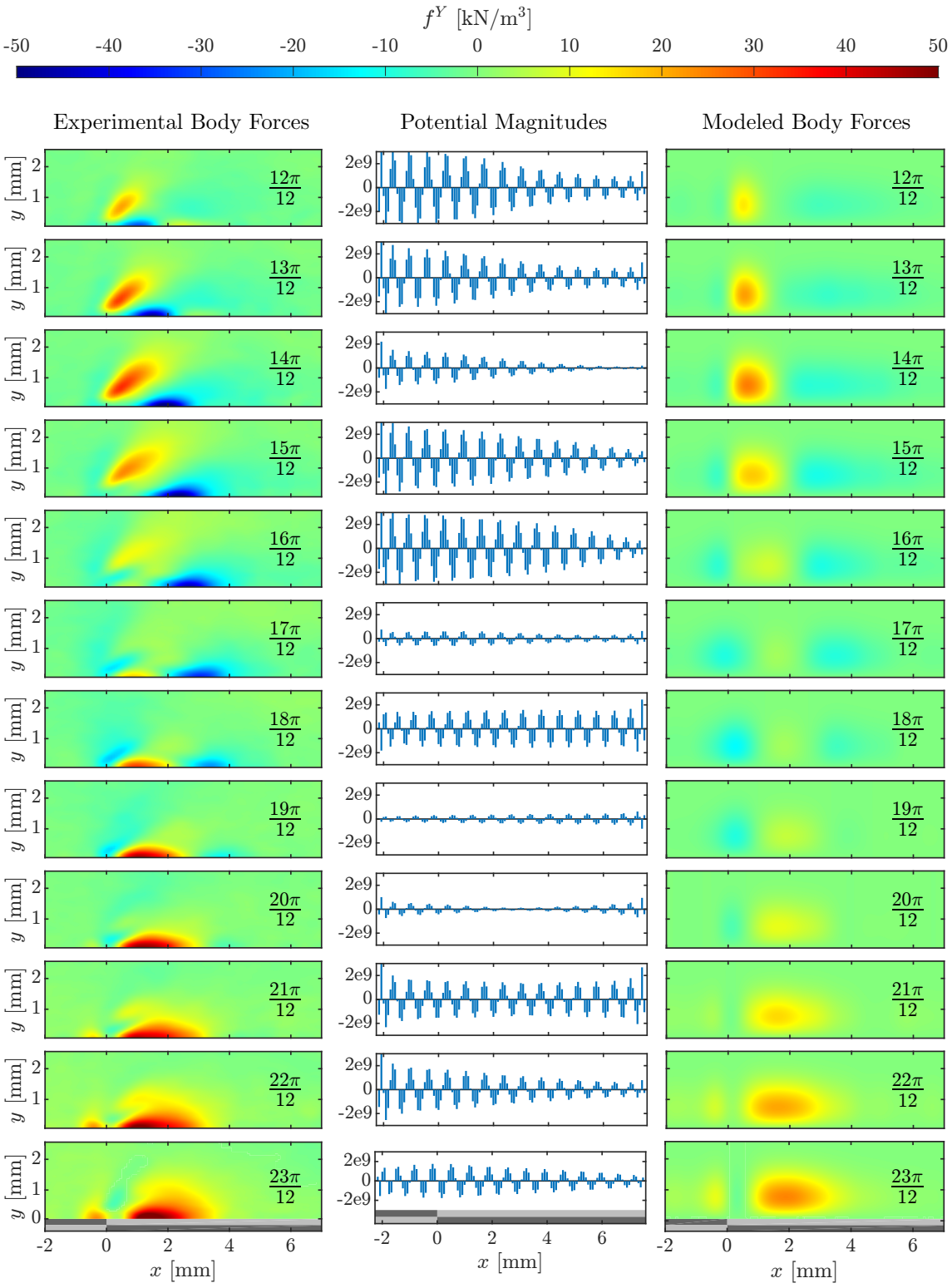

Figure D.20.: Exponential potential formulation, y-direction, phases $12\pi/12$ to $23\pi/12$. Experimental body forces according to Hehner *et al.* [12, 13].

E. Complete figure list for a numerical grid extended with 20 grid cells

X-Direction

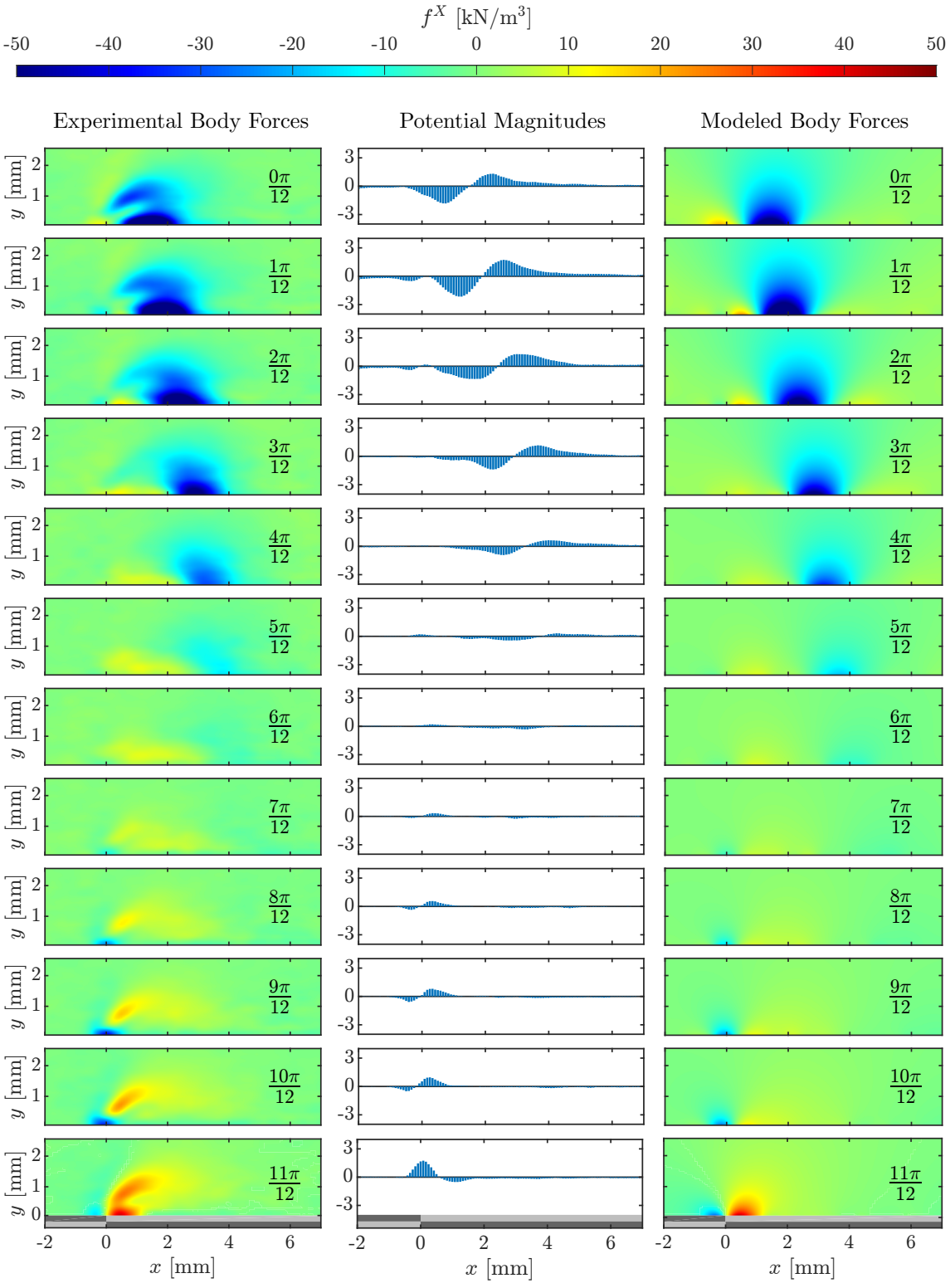

Figure E.21.: Numerical grid extended by 20 cells, MBFs shortened to original length, phases $0\pi/12$ to $11\pi/12$ in x-direction. Experimental body forces according to Hehner *et al.* [12, 13].

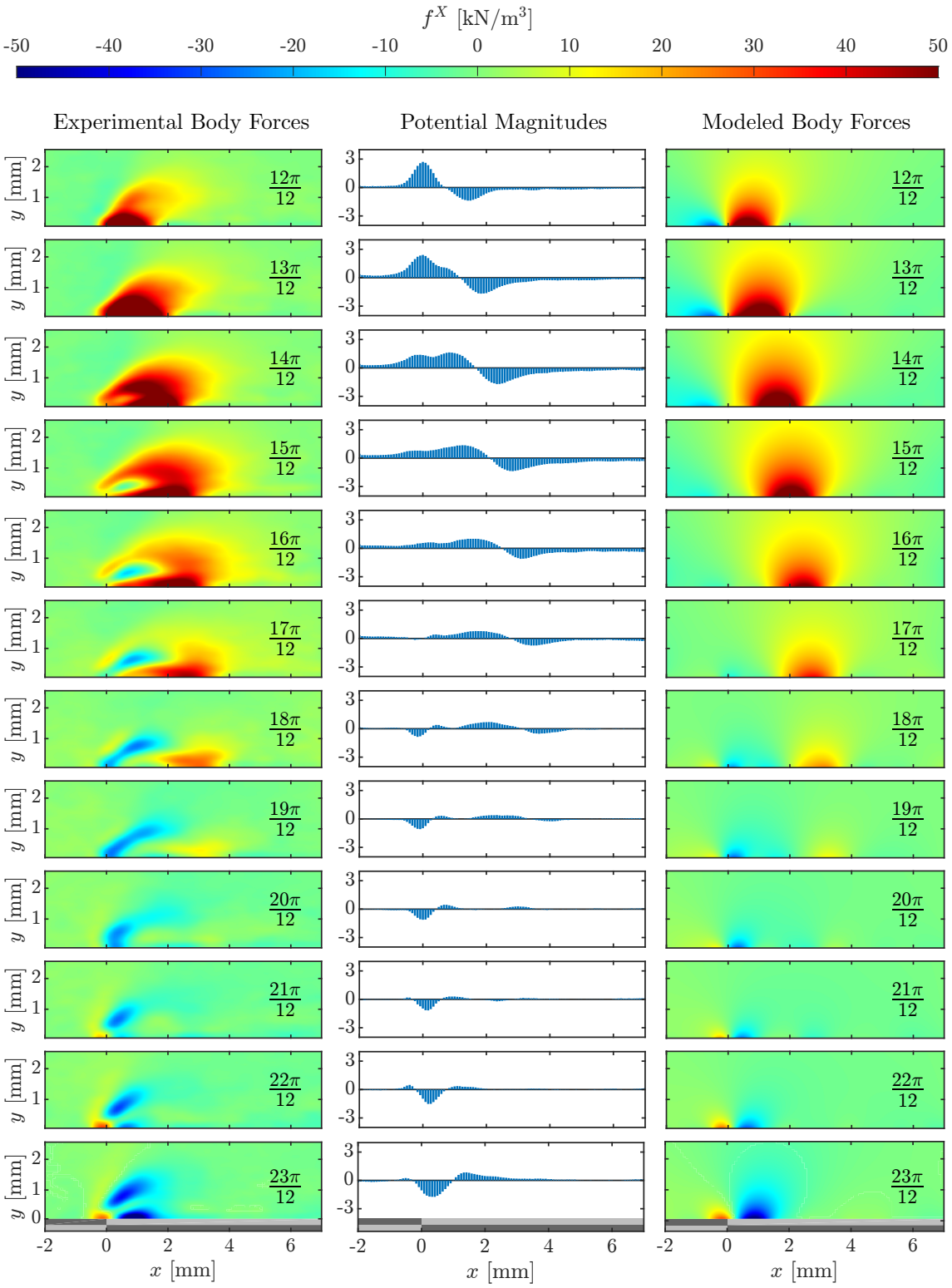

Figure E.22.: Numerical grid extended by 20 cells, MBFs shortened to original length, phases $12\pi/12$ to $23\pi/12$ in x-direction. Experimental body forces according to Hehner *et al.* [12, 13].

Y-Direction

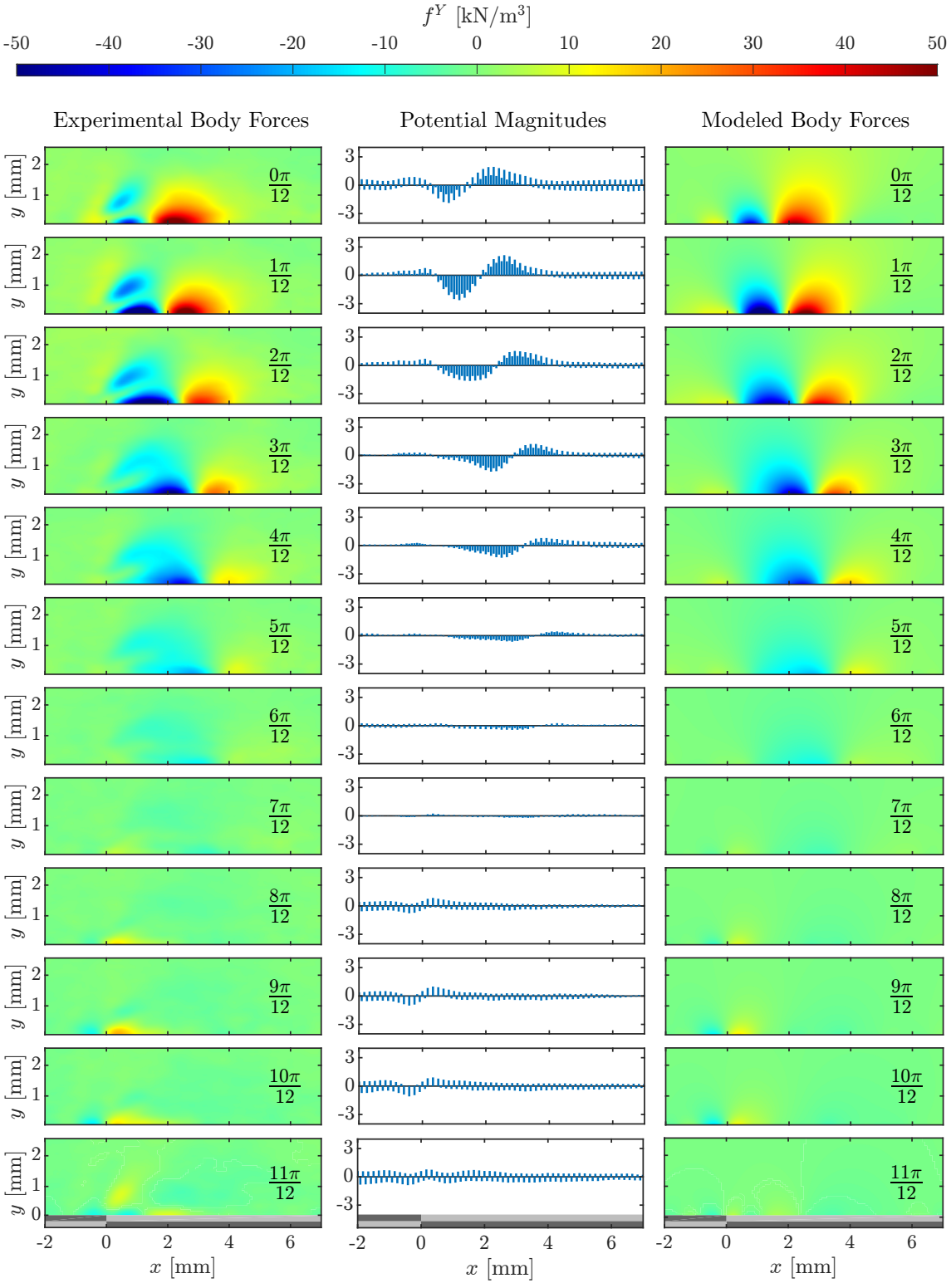

Figure E.23.: Numerical grid extended by 20 cells, MBFs shortened to original length, phases $0\pi/12$ to $11\pi/12$ in y-direction. Experimental body forces according to Hehner *et al.* [12, 13].

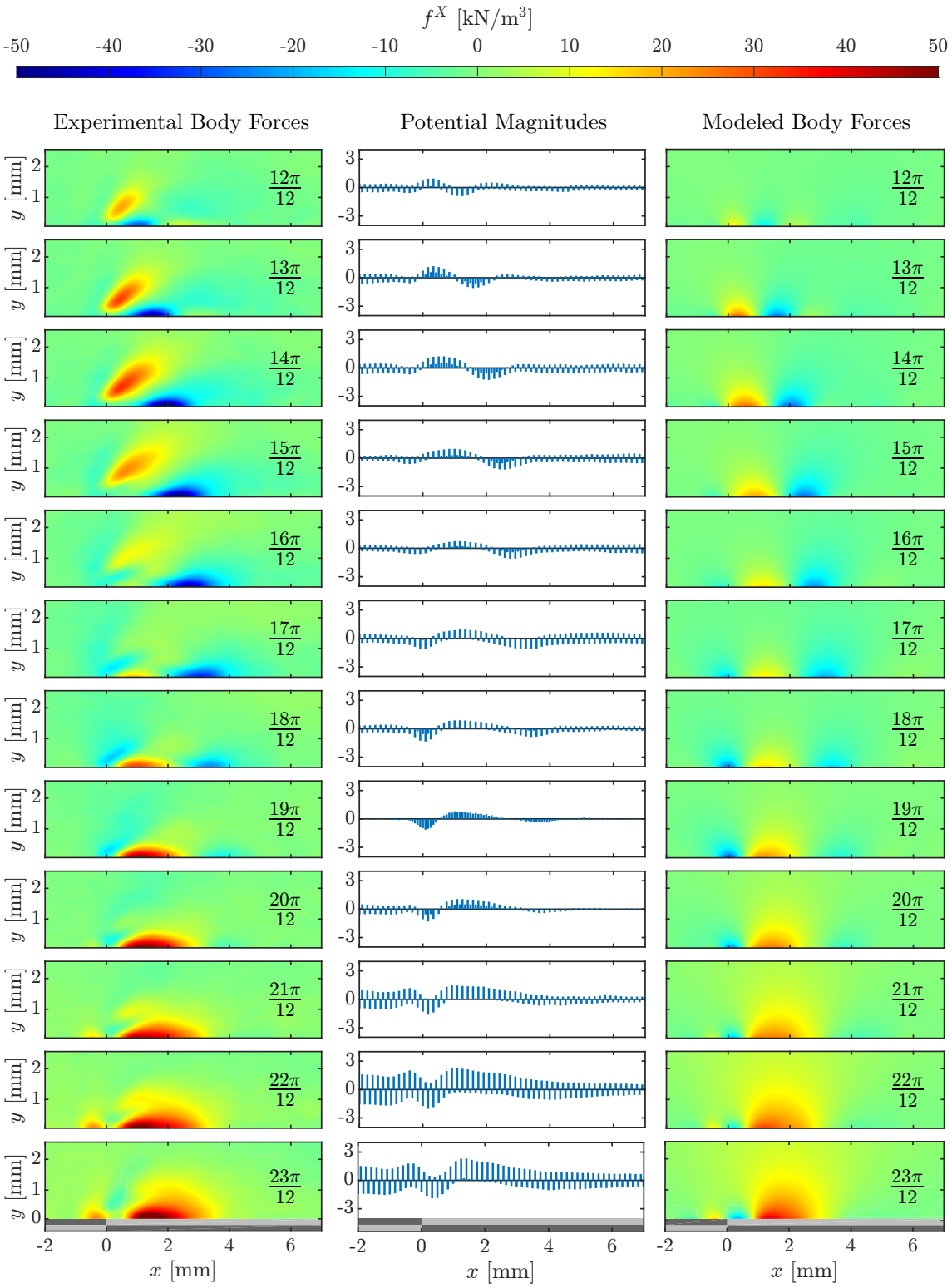

Figure E.24.: Numerical grid extended by 20 cells, MBFs shortened to original length, phases $12\pi/12$ to $23\pi/12$ in y-direction. Experimental body forces according to Hehner *et al.* [12, 13].

F. Complete figure list of body force fields with an extension of 40 grid cells and 20 additional potentials

X-Direction

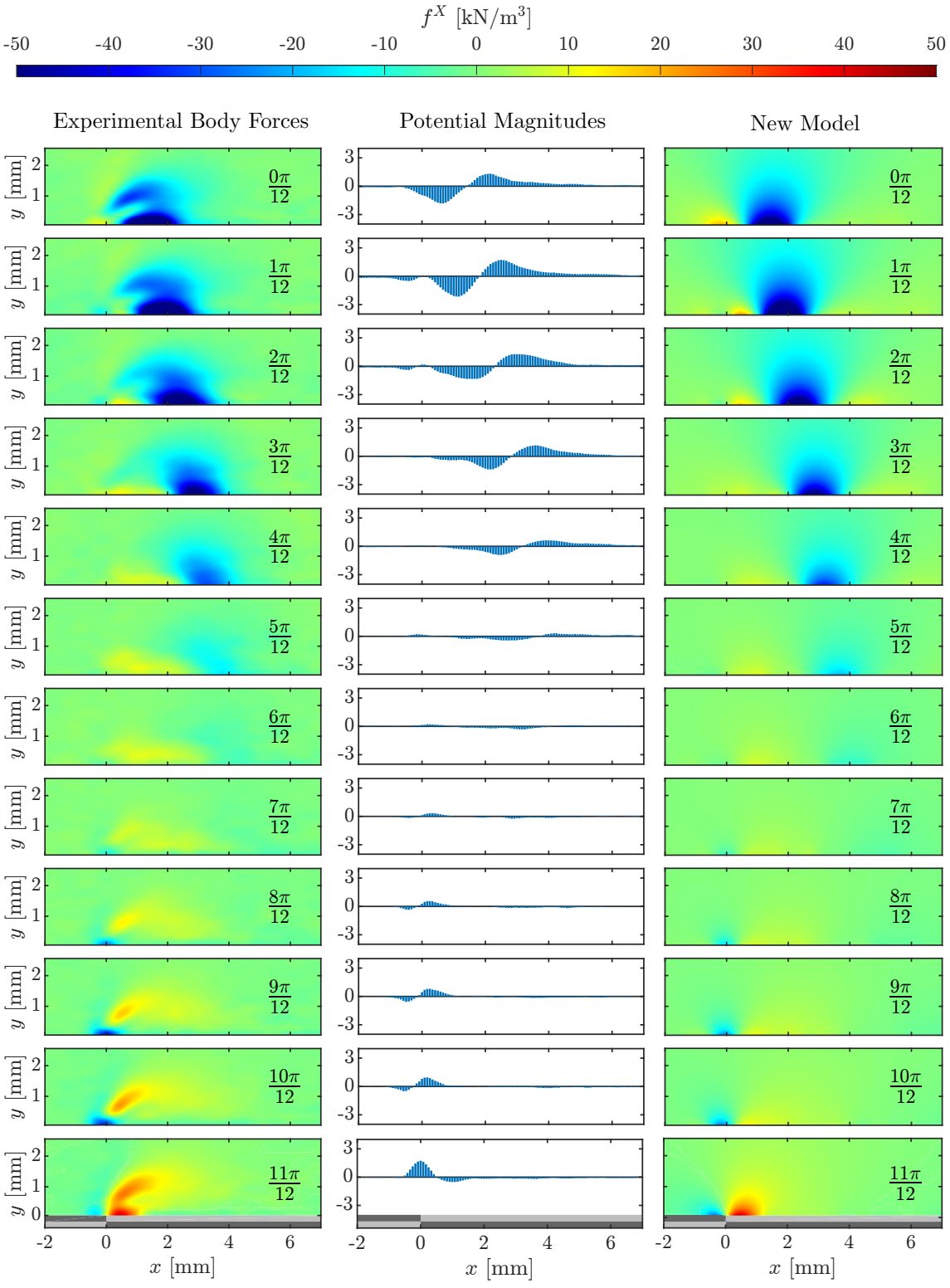

Figure F.25.: Numerical grid extended by 40 cells and with 20 additional potentials on each side, phases $0\pi/12$ to $11\pi/12$ in x-direction. Experimental body forces according to Hehner *et al.* [12, 13].

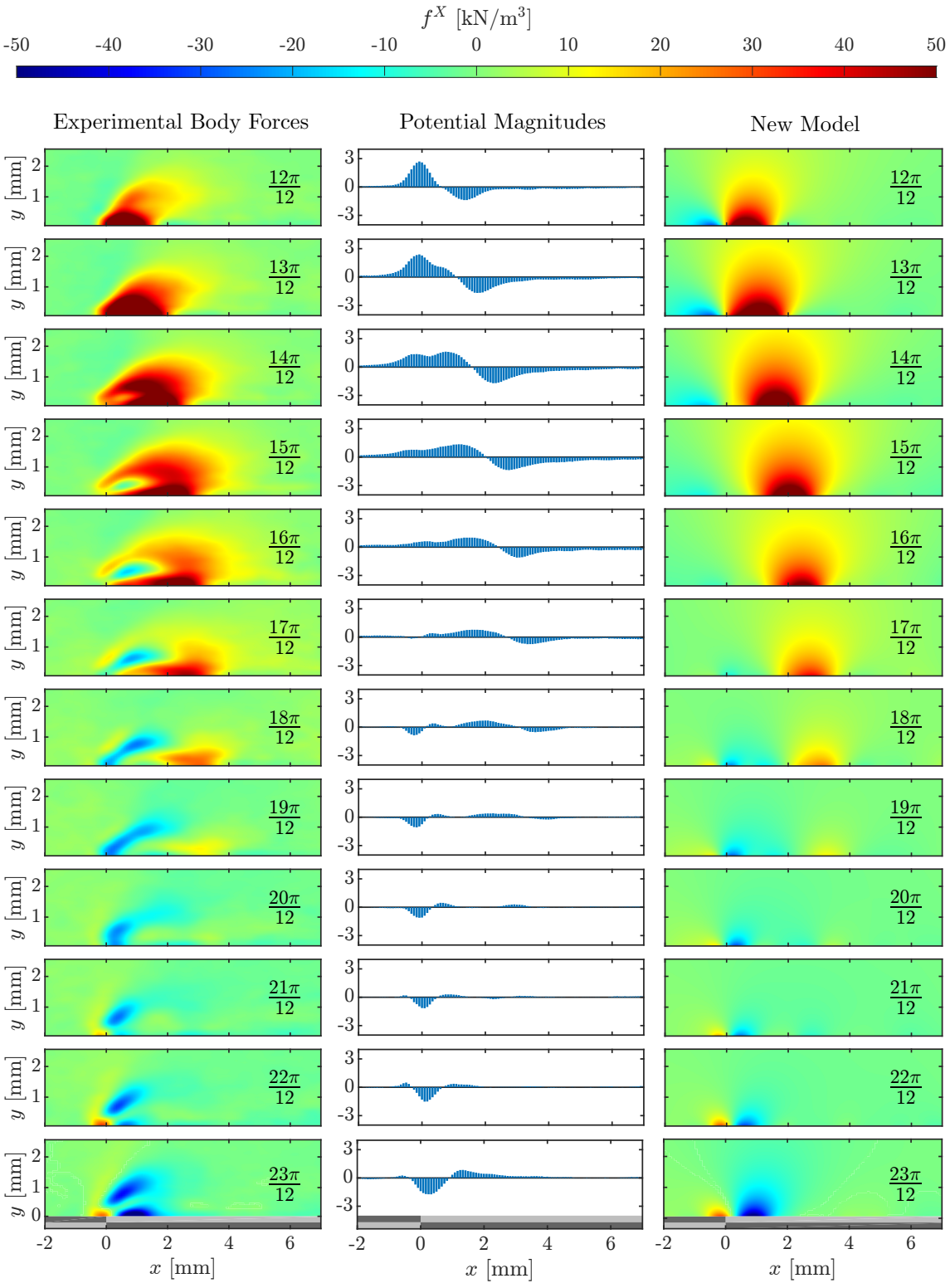

Figure F.26.: Numerical grid extended by 40 cells and with 20 additional potentials on each side, phases $12\pi/12$ to $23\pi/12$ in x-direction. Experimental body forces according to Hehner *et al.* [12, 13].

Y-Direction

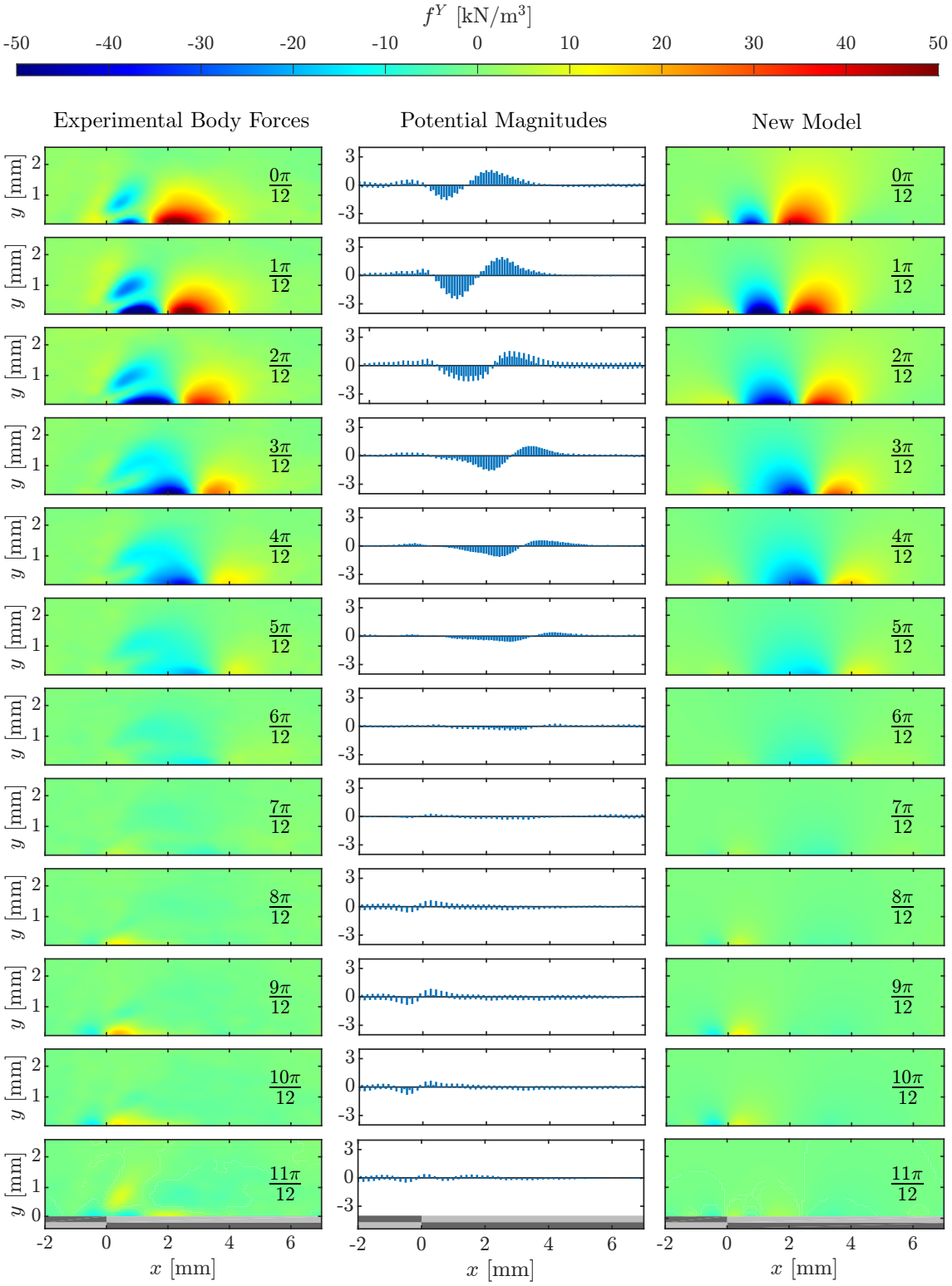

Figure F.27.: Numerical grid extended by 40 cells and with 20 additional potentials on each side, phases $0\pi/12$ to $11\pi/12$ in y-direction. Experimental body forces according to Hehner *et al.* [12, 13].

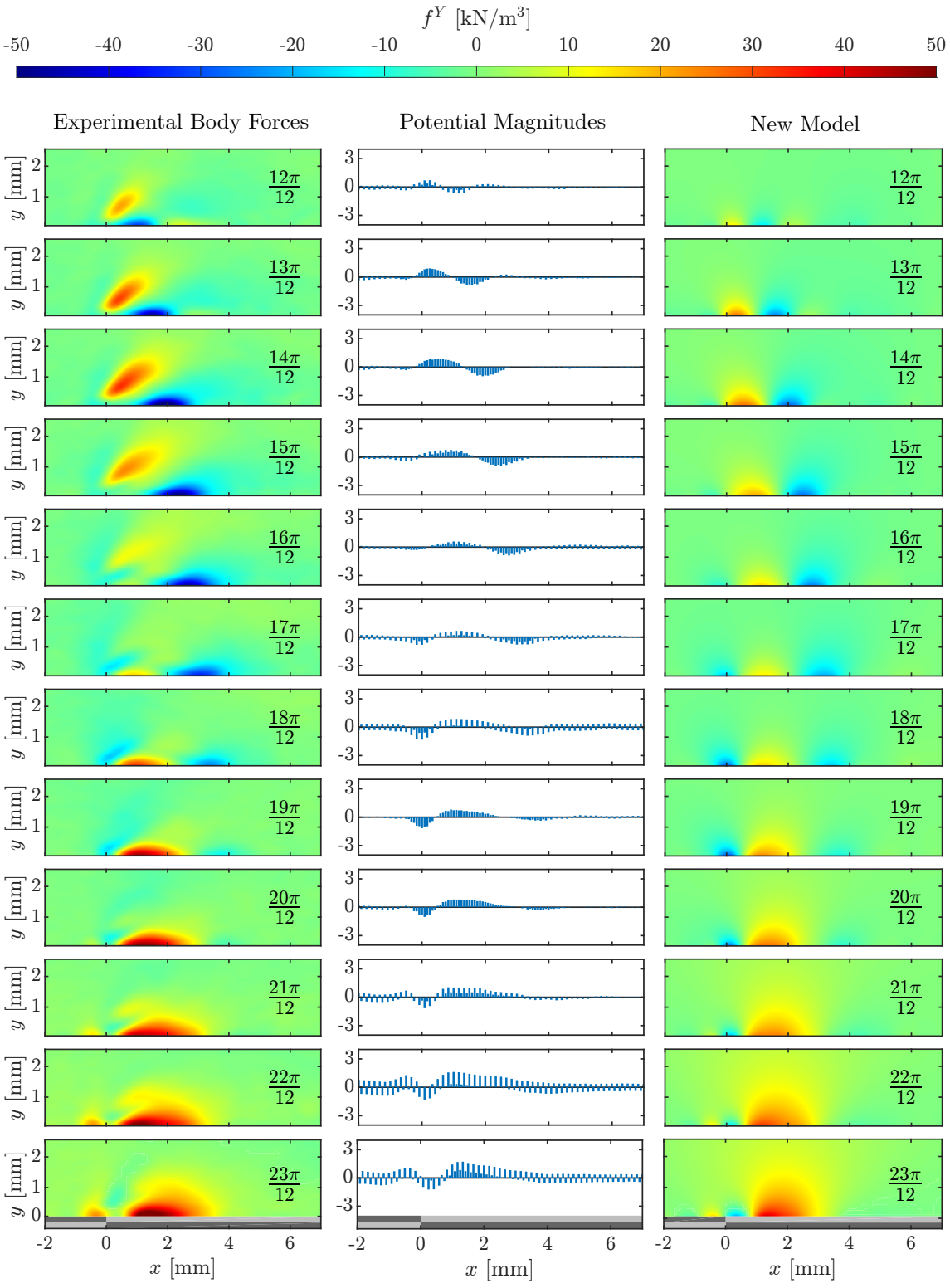

Figure F.28.: Numerical grid extended by 40 cells and with 20 additional potentials on each side, phases $12\pi/12$ to $23\pi/12$ in y-direction. Experimental body forces according to Hehner *et al.* [12, 13].

G. Complete figure list of body force fields for an decreased potential distance

X-Direction

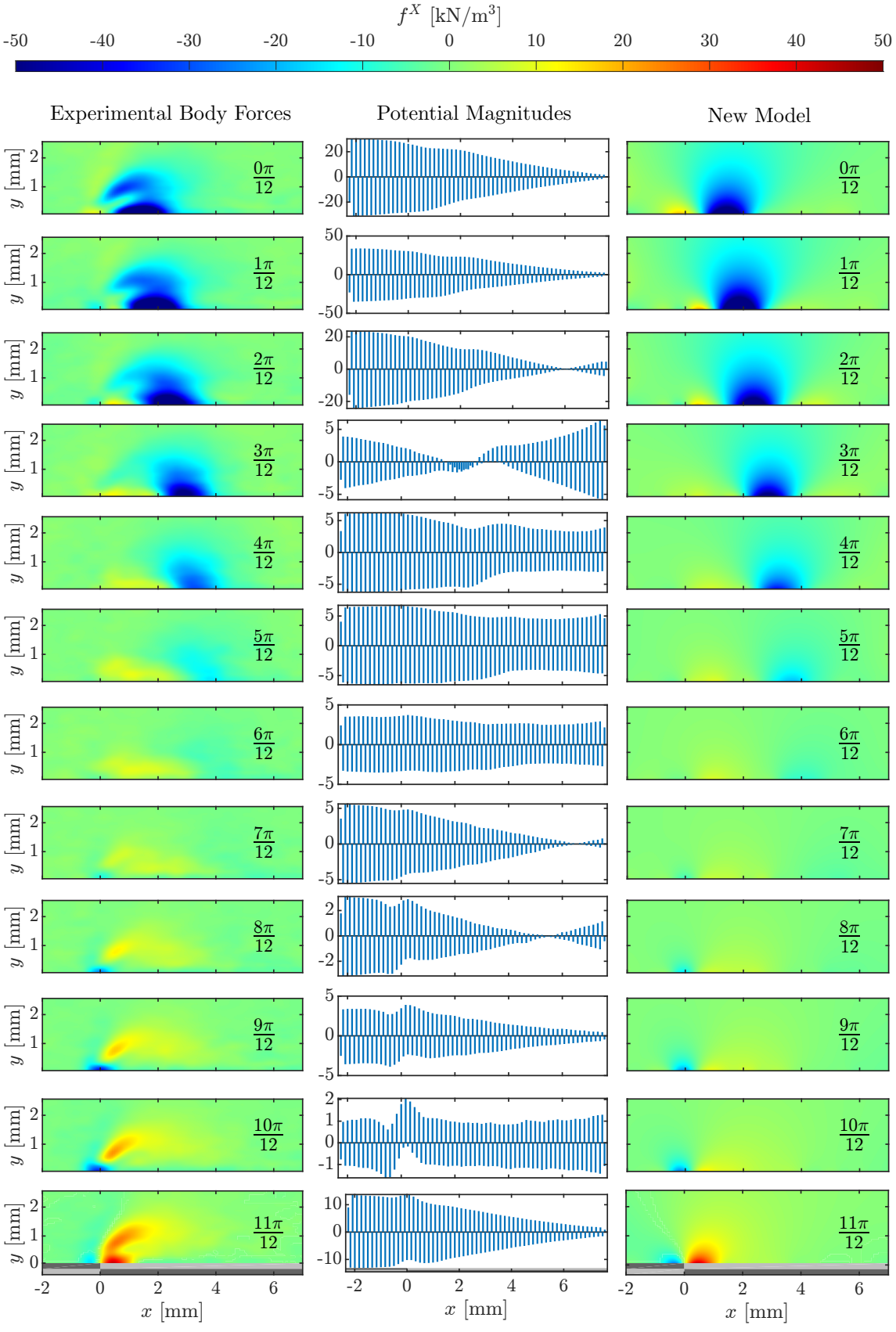

Figure G.29.: Distance between the potentials: $0.9999 \cdot \Delta x$, modeling results in x-direction, phases 0 to $11\pi/12$. Note that the ordinate limits of the PMs are not uniform. Experimental body forces according to Hehner *et al.* [12, 13].

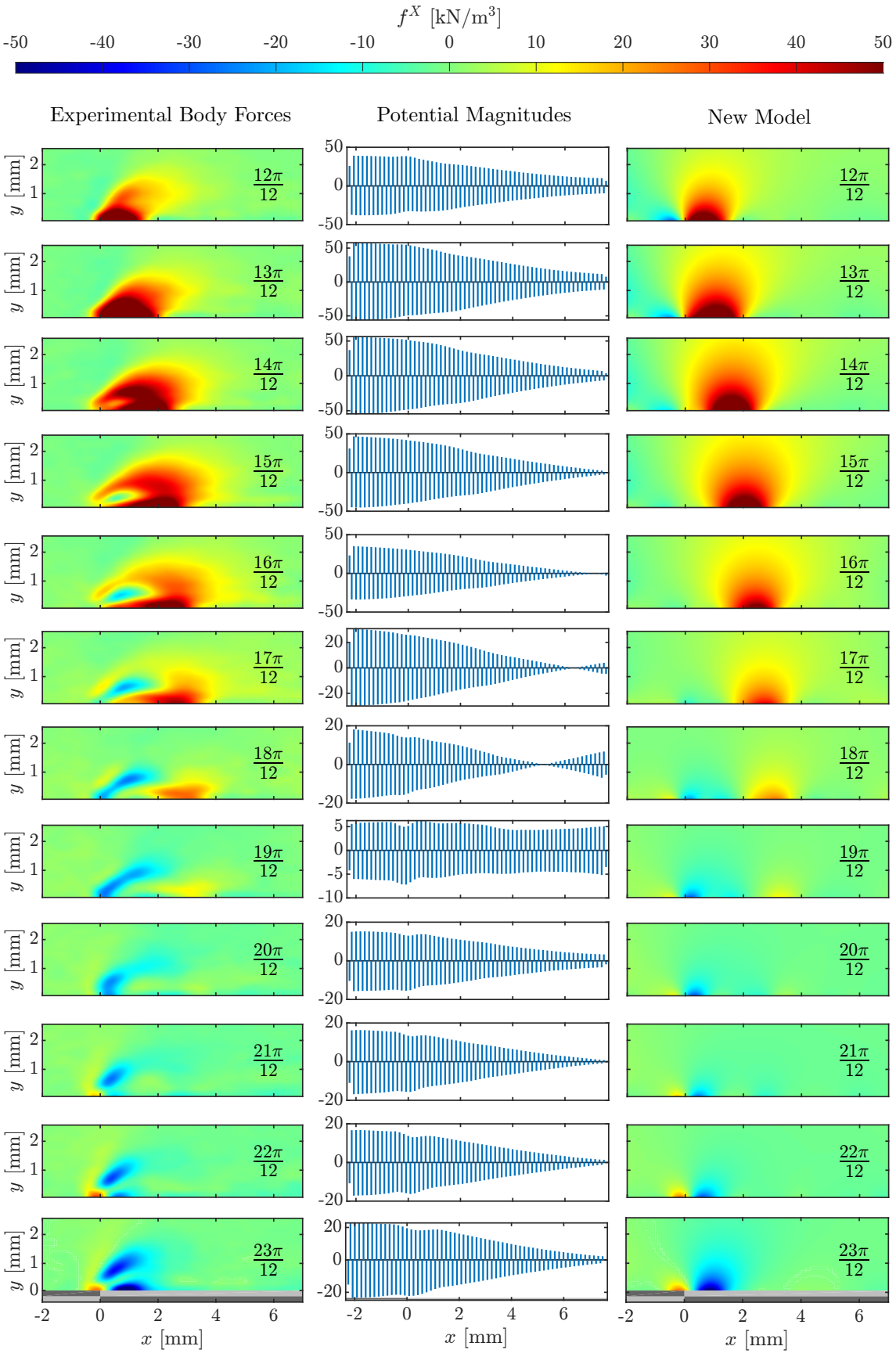

Figure G.30.: Distance between the potentials: $0.9999 \cdot \Delta x$, modeling results in x-direction, phases $12\pi/12$ to $23\pi/12$. Note that the ordinate limits of the PMs are not uniform. Experimental body forces according to Hehner *et al.* [12, 13].

Y-Direction

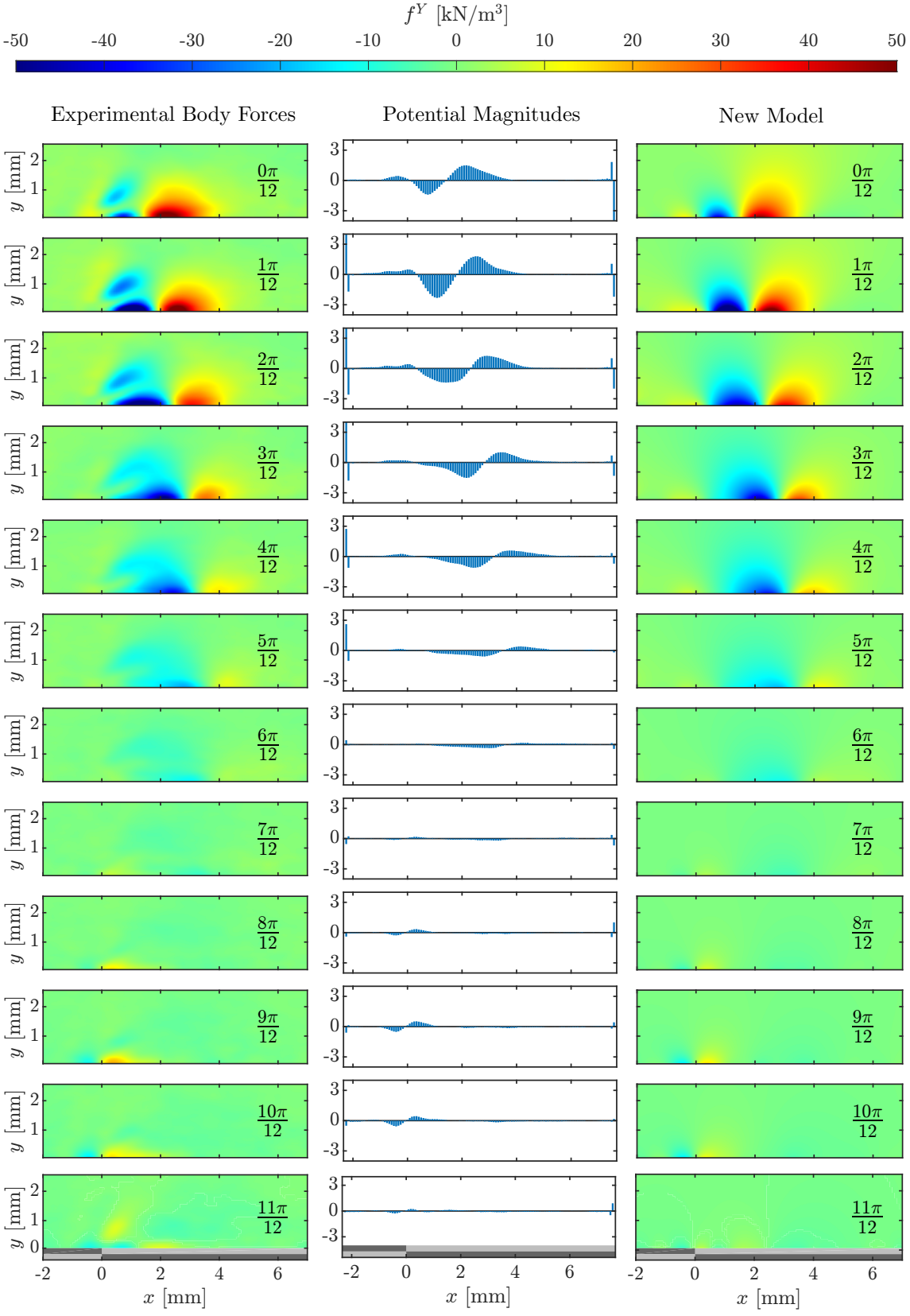

Figure G.31.: Distance between the potentials: $0.9999 \cdot \Delta x$, modeling results in y-direction, phases $0\pi/12$ to $11\pi/12$. Experimental body forces according to Hehner *et al.* [12, 13].

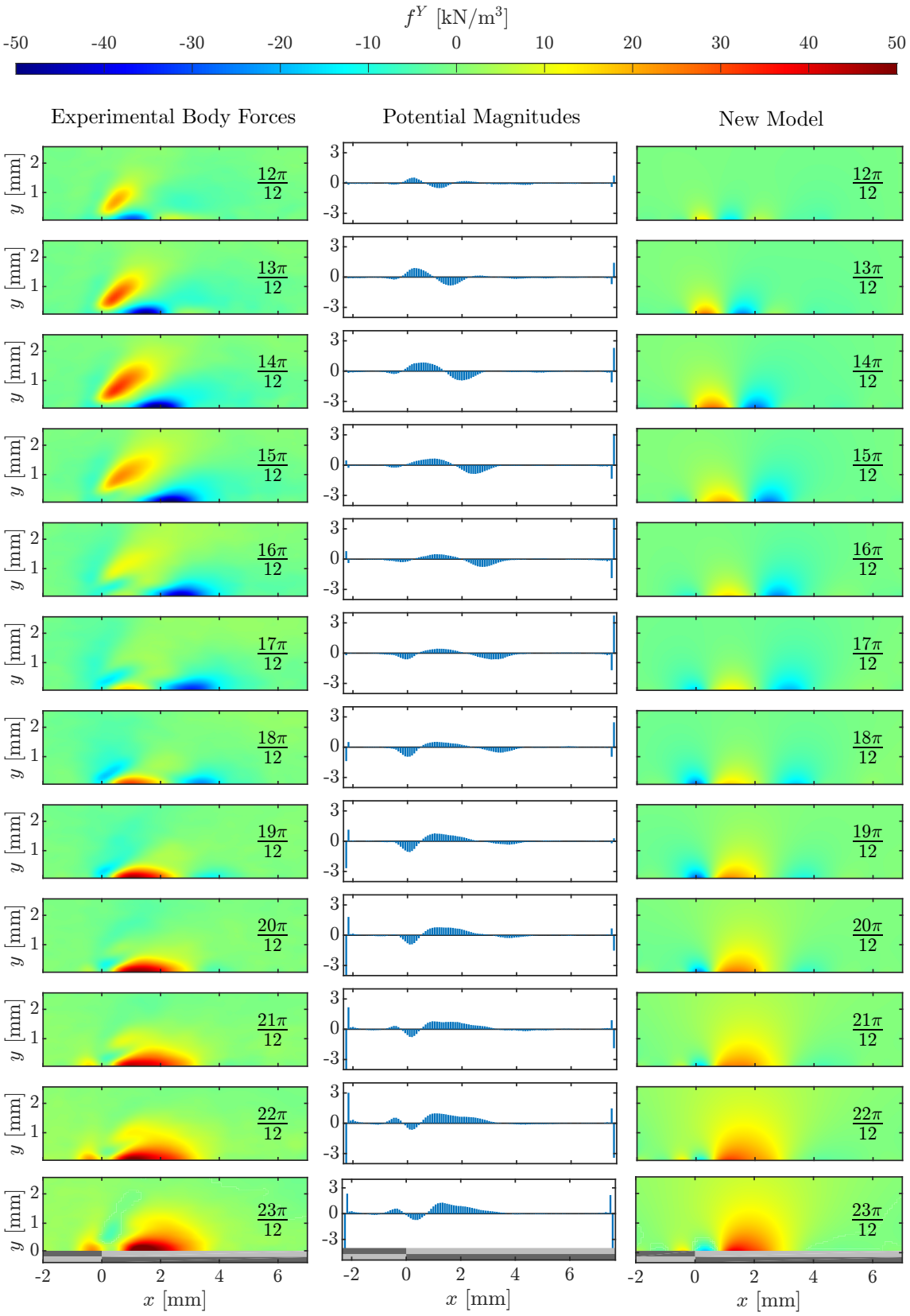

Figure G.32.: Distance between the potentials: $0.9999 \cdot \Delta x$, modeling results in y-direction, phases $12\pi/12$ to $23\pi/12$. Experimental body forces according to Hehner *et al.* [12, 13].

H. Complete figure list of body force fields for multiple potential rows

X-Direction

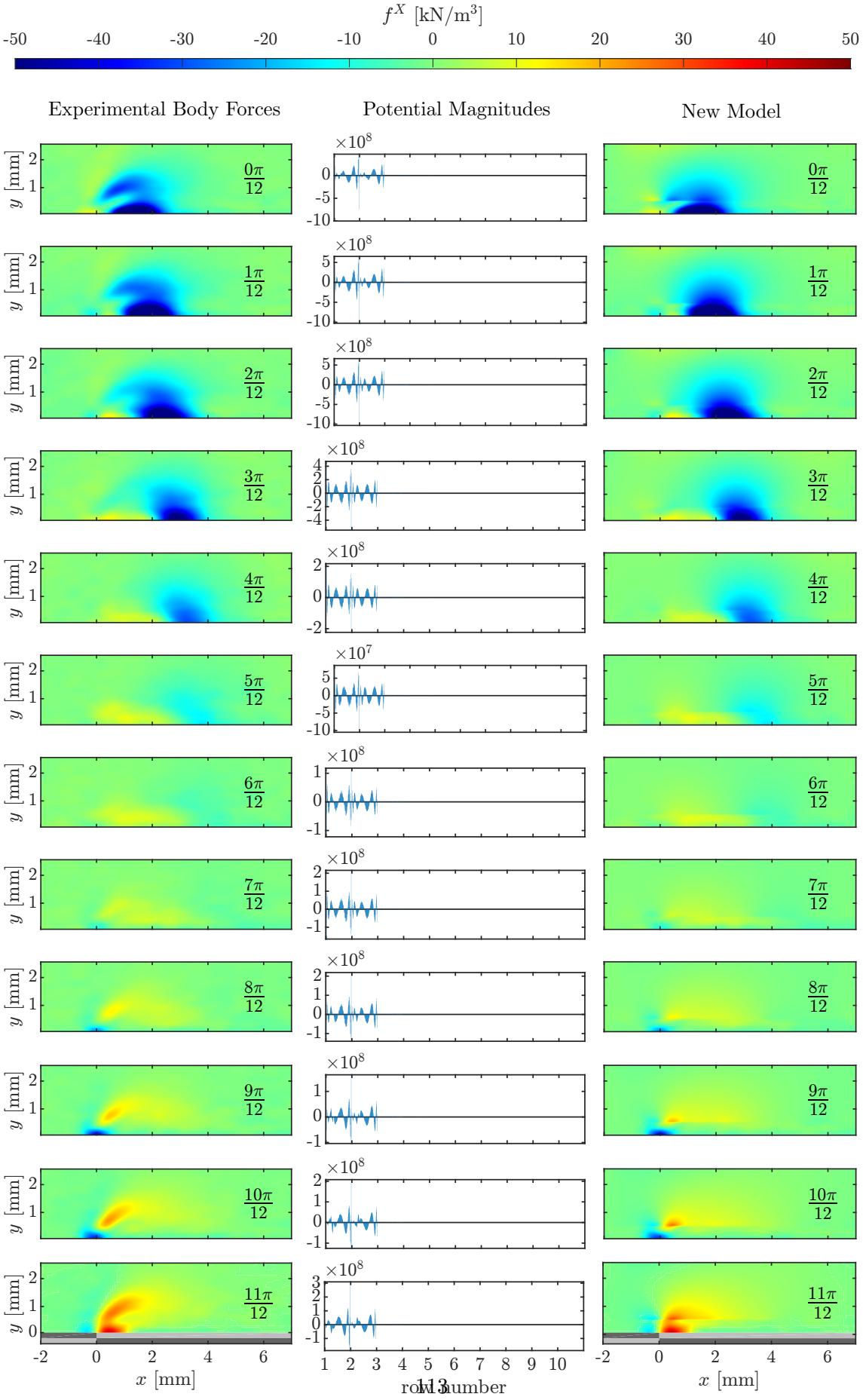

Figure H.33 : 10 potential rows above the actuator, phases $0\pi/12$ to $11\pi/12$ in x-direction.

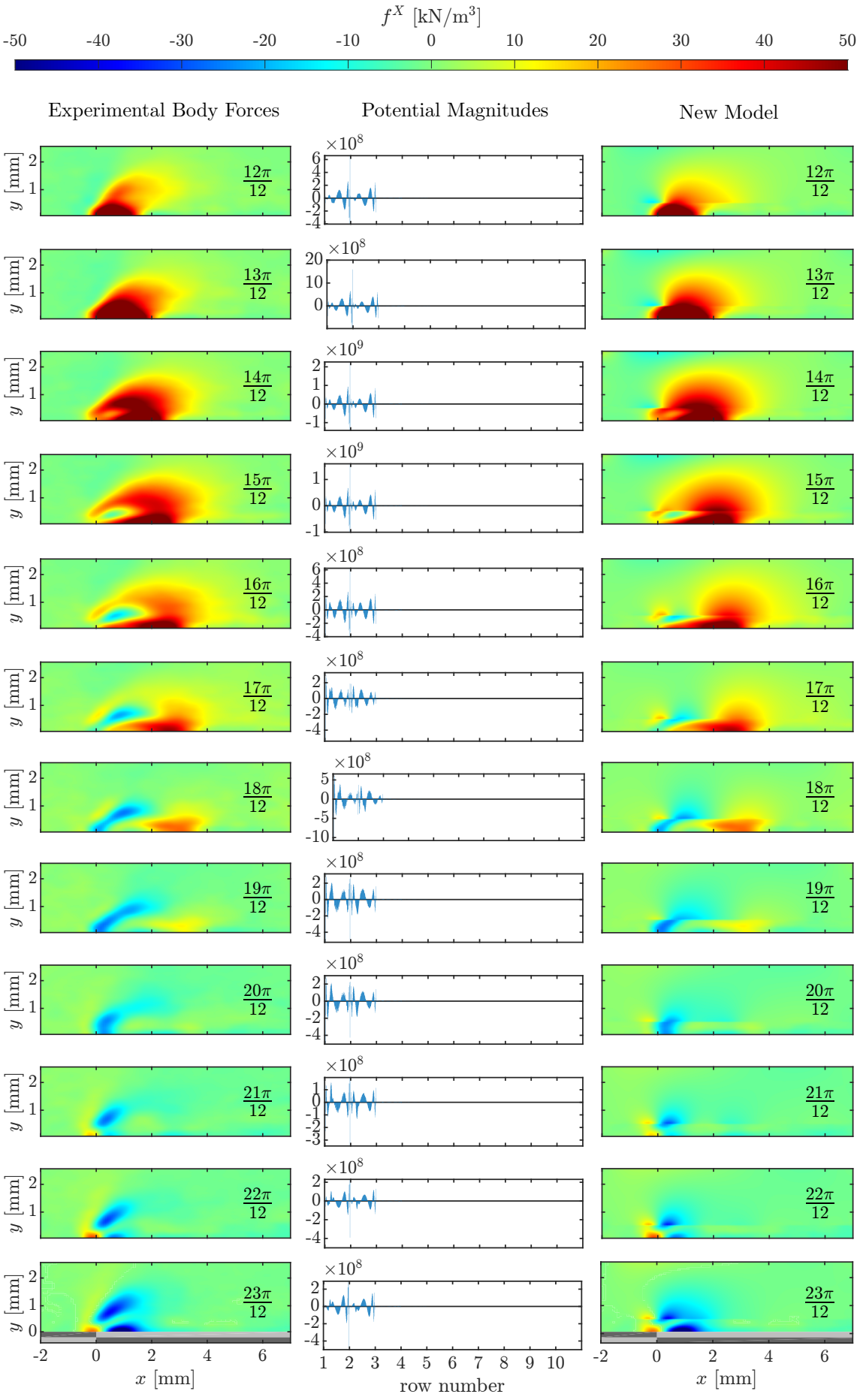

Figure H.34.: 10 potential rows above the actuator, phases $12\pi/12$ to $23\pi/12$ in x-direction. Note that the ordinate limits of the PMs are not uniform. Experimental body forces according to Hehner *et al.* [12, 13].

Y-Direction

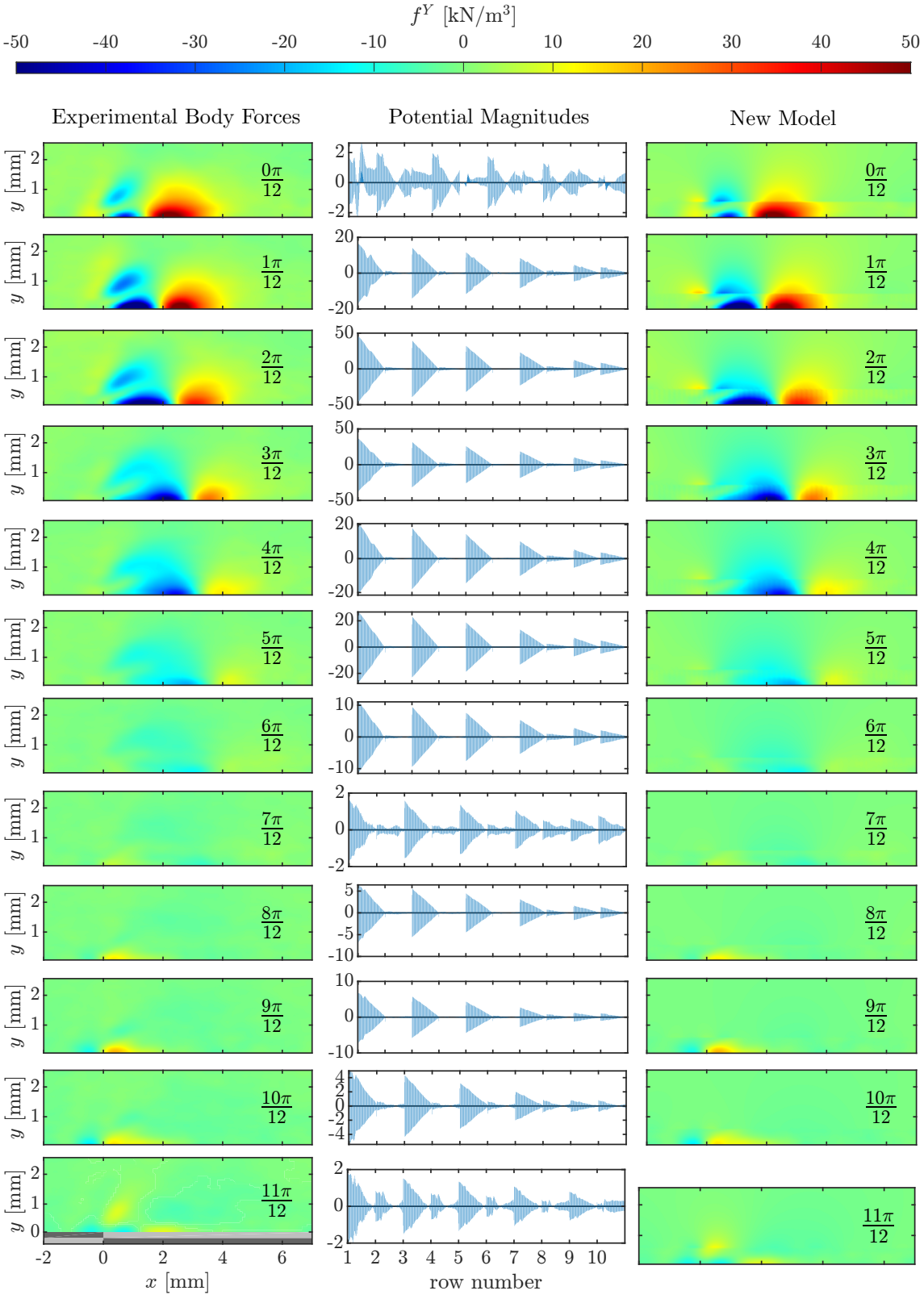

Figure H.35.: 10 potential rows above the actuator, phases $0\pi/12$ to $11\pi/12$ in y-direction. Note that the ordinate limits of the PMs are not uniform. Experimental body forces according to Hehner *et al.* [12, 13].

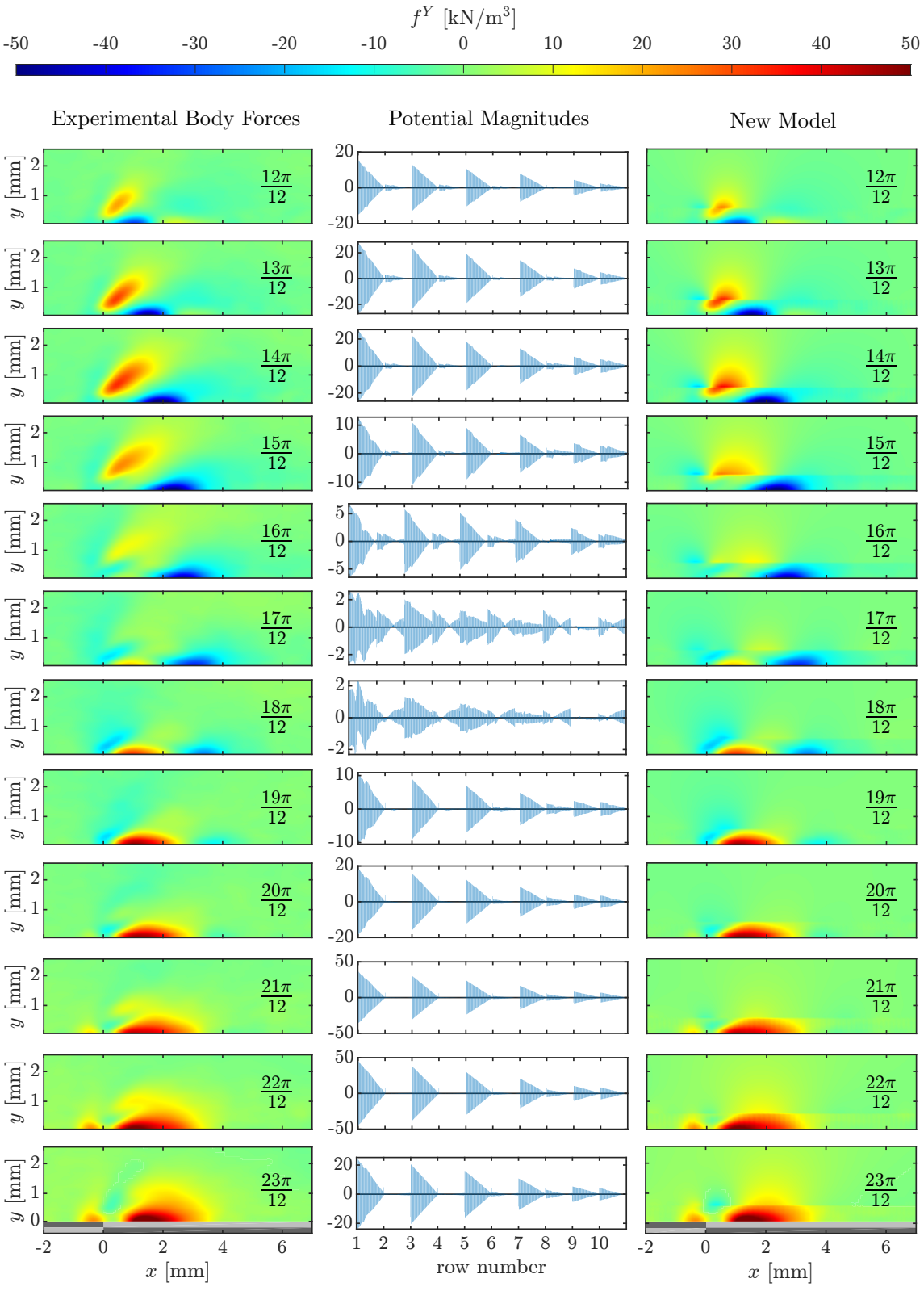

Figure H.36.: 10 potential rows above the actuator, phases $12\pi/12$ to $23\pi/12$ in y-direction. Note that the ordinate limits of the PMs are not uniform. Experimental body forces according to Hehner *et al.* [12, 13].

I. MATLAB Code

Main Script

```
%% Import experimental data: coordinate system, PIV-data, body forces derived via the NSE; for all 24 Phases

import_data('body_force_quiescent_air');

%% Variables for some of the model configurations

distance = 1;           % Distance between potentials, in relation to the grid cell length 1 -> 1 * 8.3e-2 mm
extension = 40;         % The numerical grid is extended up- and downstream by this amount of cells
addition = 20;          % Number of additional potentials which are positioned up- and downstream


%% Main for-loop: Each phase is calculated seperately. Solely the calculation matrix is reused for each iteration
for phase = 1:24

    % % Selection of body force data of the current phase
        F_x = fx_Wilke(:,:,phase);
        F_y = fy_Wilke(:,:,phase);


    % % Storage of the original body forces and coordinates
        F_x_org = F_x;
        F_y_org = F_y;

        x_org = x;
        y_org = y;


    % % Extension of the experimental body forces (if extension > 0)

        % Initialization of an empty matrix
        zeros_x = zeros(size(F_x,1), size(F_x,2) + 2*erweiterung);
        zeros_y = zeros(size(F_y,1), size(F_y,2) + 2*erweiterung);

        % Copying of experimental data into empty matrix
            for j = 1:size(F_x,1)
                for i = 1:size(F_x,2)
                    zeros_x(j,i+erweiterung) = F_x(j,i);
                    zeros_y(j,i+erweiterung) = F_y(j,i);
                end
            end

```

```
42          % Renaming body force matrix to the exptended one
43          F_x = zeros_x;
44          F_y = zeros_y;
45
46
47      % % The matrix is transformed into a line vector for the
            fitting process
48          F_line_x = F_x';
49          F_line_x = [F_line_x(:)];
50
51          F_line_y = F_y';
52          F_line_y = [F_line_y(:)];
53
54
55      % % Storage of the dimensions of the numerical grid
56      % % (41 x 117 for the original state
57          y_dim = size(F_x,1);
58          x_dim = size(F_x,2);
59
60          y_dim_org = size(F_x_org,1);
61          x_dim_org = size(F_x_org,2);
62
63
64      %% Creation of the matrices A_x and A_y for the fitting
            process
65      % % To save run time, the matrices are only computed for
            the first phase and re-used for the other phases
66
67          if phase == 1
68                  [A_x, A_y, x, y, amount_potentials] =
                        design_matrix(x, y, extension, addition,
                        distance, x_dim, y_dim);
69                  disp('New matrices')
70          end
71
72
73      %% Fitting of the respective equation system compilation
            with the LSMR function
74
75          % % PMs_x contains the potential magnitudes for the
                current phase
76          [PMs_x] = LSMR_fitting(teil, A_x, F_line_x);
77
78              % % Computation of the respective modeled body
                    forces within
79              % the bounds of the experimental CV
80              matrix_x =  (A_x * PMs_x);
81              matrix_x = reshape(matrix_x,[x_dim,y_dim]);
82              matrix_x = matrix_x';
83              matrix_x = matrix_x(:,extension+1:end-extension);
84
85          % % summary of the body forces of all phases
```

```
86          newmodel_x(:,:,phase) = matrix_x;
87
88          % % summary of PM vectors for all phases
89          all_solutions_x(phase,:) = PMs_x;
90
91
92          % % PMs_y contains the potential magnitudes for the
                current phase
93          [PMs_y] = LSMR_fitting(teil, A_y, F_line_y);
94
95              % % Computation of the respective modeled body
                    forces within
96              % % the bounds of the experimental CV
97              matrix_y =  (A_y * PMs_y);
98              matrix_y = reshape(matrix_y,[x_dim,y_dim]);
99              matrix_y = matrix_y';
100             matrix_y = matrix_y(:,extension+1:end-extension);
101
102         % % summary of the body forces of all phases
103         newmodel_y(:,:,phase) = matrix_y;
104
105         % % summary of PM vectors for all phases
106         all_solutions_y(phase,:) = PMs_y;
107
108
109
110 % %         %% Computation of a common PM vector for both
    directions
111 % %
112 % %
113 % %             % % PMs_both contains the common potential
    magnitudes for the current phase
114 % %                 [PMs_both] = LSMR_fitting_common_PMs(A_x,
    A_y, F_line_x, F_line_y);
115 % %
116 % %                 % % Computation of the respective modeled
    body forces within
117 % %                 % the bounds of the experimental CV
118 % %                     matrix_x =  (A_x * PMs_both);
119 % %                     matrix_x = reshape(matrix_x,[x_dim,
    y_dim]);
120 % %                     matrix_x = matrix_x';
121 % %                     matrix_x = matrix_x(:,extension+1:end-
    extension);
122 % %
123 % %                 % % summary of the body forces of all
    phases
124 % %                 newmodel_x(:,:,phase) = matrix_x;
125 % %
126
127 % %                 % % Computation of the respective modeled
    body forces within
```

```
% %                   % the bounds of the experimental CV
% %                       matrix_y =  (A_y * PMs_both);
% %                       matrix_y = reshape(matrix_y,[x_dim,
    y_dim]);
% %                       matrix_y = matrix_y';
% %                       matrix_y = matrix_y(:,extension+1:end-
    extension);
% %
% %
% %                   % % summary of the body forces of all
    phases
% %                   newmodel_y(:,:,phase) = matrix_y;
% %
% %
% %                   % % summary of PM vectors for all phases
% %                   all_solutions_both(phase,:) = PMs_both;

end
```

Creation of Matrices

```
function [A_x, A_y, x, y, amount_potentials] = design_matrix(x
    , y, extension, addition, distance, x_dim, y_dim)

%% Extension of coordinate vectors
delta_x = x(1,2) - x(1,1);

        % % Extension of x-vector
            for i = 1:extension
                new_line_x1 = (x(1,1) - delta_x) * ones(size(x
                    ,1),1);
                new_line_x2 = (x(1,size(x,2)) + delta_x) *
                    ones(size(x,1),1);
                x = [new_line_x1 x new_line_x2];
            end

        % % Extension of y-vector
            for i = 1:2*extension
                y = [y y(:,end)];
            end

%% Positioning of potentials according to chapter 5.2
    % % Distance between two potentials in [m]
    distance_real = distance * delta_x;

    % % Distance between original last potential and last
        added potential
    distance_end = addition * delta_x;

    % % Vector contains the positions of the potential
    lx_knot = (x(1,1) - distance_end - 0.5 * distance_real :
        distance_real : x(1,end) + distance_end + 0.5 *
```

```
       distance_real);

    % % Counter for set up of matrix
    amount_potentials = (1:length(lx_knot));


%% Set up of the matrix.
% % The variabel r defines the current line in the matrix
% % (each line refers to a single position in the grid)
r = 1;

    % % Counter for y-position in grid
    for j = 1:y_dim

        % % Counter for x-position in grid
        for k = 1:x_dim

            % % Counter for position of the potential
            for i = 1:length(amount_potentials)

                % % Distance between the current potential and
                    current position in grid
                radius = sqrt( (lx_knot(teil(i)) - lx(k))^2 +
                   (ly(j) - 0) );

                % % Set up of matrices according to eqn. (5.5)
                    and (5.6)
                A_x(r,i) = (lx(k) - lx_knot(teil(i))) / radius
                   ^2;
                A_y(r,i) = (ly(j) - 0) / radius^2;

            end
            r = r + 1;
        end
    end
```

Fitting Process for Each Spatial Direction

```
function [PMs] = LSMR_fitting(teil, A, F)

%% Initialization of variables for fitting

    lambda = 0;
    iter_max = 1600;
    atol = 0;
    btol = 0;
    conlim = 0;
    itnlim = iter_max;
    localSize = Inf;
    show = true;
    x0 = zeros(length(teil),1);

```

```
%%
[PMs] = lsmr(A, F, lambda, atol, btol, conlim, itnlim,
    localSize, show, x0);
%%
```

Fitting Process with a Common PM Vector for Both Spatial Directions

```
function [PMs_both] = LSMR_fitting_common_PMs(A_x, A_y,
    F_line_x, F_line_y)

% % This script is mostely equivalent to the basic fitting
    script, but
% % joins the computed matrices and the experimental data
    first
A = [A_x; -A_y];
F_all = [F_line_x; F_line_y];

%% Initialization of variables for fitting

    lambda = 0;
    iter_max = 1600;
    atol = 0;
    btol = 0;
    conlim = 0;
    itnlim = iter_max;
    localSize = Inf;
    show = true;
    x0 = zeros(length(teil),1);
%%
[PMs_both] = lsmr(A, F_all, lambda, atol, btol, conlim, itnlim
    , localSize, show,x0);
%%
```